Title
Geochemical and Petrological Investigations into Mantle Minerals from Experiments and Natural Samples

Author
Macris, Catherine Amy

Publication Date
2012

Peer reviewed|Thesis/dissertation

UNIVERSITY OF CALIFORNIA

Los Angeles

Geochemical and Petrological Investigations into Mantle Minerals from Experiments and Natural Samples

A dissertation submitted in partial satisfaction of the requirements for the degree of Doctor of Philosophy in Geochemistry

by

Catherine Amy Macris

2012

ABSTRACT OF THE DISSERTATION

Geochemical and Petrological Investigations into Mantle Minerals

from Experiments and Natural Samples

by

Catherine Amy Macris

Doctor of Philosophy in Geochemistry

University of California, Los Angeles, 2012

Professor Craig E. Manning, Chair

This dissertation consists of a series of studies investigating geochemical and petrological aspects of mantle minerals, namely, olivine, spinel, orthopyroxene, and clinopyroxene. The first study is an experimental look at the solubility of the clinopyroxene mineral diopside ($CaMgSi_2O_6$) in natural fluids. Results allow insight into the chemistry of high *P*-*T* fluids and the behavior of a major mantle mineral in equilibrium with such fluids. The second study focuses on iron isotopic compositions of mantle minerals as powerful tracers for geochemical processes in the mantle, such as partial melting, metasomatism, and oxidation. To address this, I studied inter-mineral iron isotopic fractionation of minerals from five distinct mantle-xenolith lithologies from San Carlos, Arizona. I compared the fractionations with opposing calculations predicting equilibrium iron fractionation at high temperatures, and applied the results to implications of petrogenesis of the xenoliths. The last study is an experimental determination of

equilibrium magnesium isotope fractionation between spinel, forsterite, and magnesite from 600°C to 800°C. In these experiments I implemented the three-isotope method with forsterite and magnesite, and with spinel and magnesite, at three different temperatures in high-pressure piston cylinder apparatus for varying lengths of time, using carbonate as the exchange medium. The result is the first rigorous high temperature experimental calibration of magnesium isotope fractionation of mantle minerals, and is generally consistent with expectations based on crystal chemical environment of Mg in these phases. The combination of experimental petrology with isotope geochemistry is a powerful approach for understanding mantle processes. Comparisons of these types studies with natural samples and theoretical predictions provide new insights into Earth's mantle.

The dissertation of Catherine Amy Macris is approved.

Edward Donald Young

Kevin D. McKeegan

Laurent G. Pilon

Craig E. Manning, Committee Chair

University of California, Los Angeles

2012

Acknowledgements

To those who have helped me along the way…

Grandma O'Shea – You encouraged me to read and be curious. You made me the person I am today and helped me every step of the way. Thank you for being you.

Matthew – You always supported me and showed sincere interest in what I was doing. I'm so lucky to have you as a brother.

Mindy – Thank you for being my best friend and a constant source of strength and happiness. You are diamond and you will shine!

James – Thank you for seeing me through tough times and always being there to make me smile (even when I didn't want to).

Anat – I'm so glad our time at UCLA overlapped. You made grad school bearable. I know we'll be friends and colleagues for the rest of our lives.

Jeremy W. – Thank you for all the discussions about science and music, and of course your endless help in the lab.

Jeremy B. – You are an inspiration in science and life. We can all learn from your attitude and perseverance in the face of adversity.

Craig and Ed – Thank you both for mentoring me and never giving up. We finally made it!

Table of Contents

List of Figures

Chapter One

Chapter Two

Chapter Three

List of Tables

Chapter One

Chapter Two

Chapter Three

VITA

EXPERIENCE

Summer 2011 to Present. Teaching Fellow
Evolution of the Cosmos, UCLA
Summer 2010 to Spring 2011. NSF GK-12 Fellow
Scientist in Residence, Emerson Middle School
Spring 2010. Teaching Assistant
Earth's Energy and The Environment, UCLA
Winter 2009—Present. Graduate Research Assistant
Department of Earth and Space Sciences, UCLA
Fall 2008. Teaching Assistant
Geochemistry, UCLA
Winter 2008—Summer 2008. Graduate Research Assistant
Department of Earth and Space Sciences, UCLA
Fall 2007. Teaching Assistant
Environmental Geology, UCLA
Winter 2007—Summer 2007. Graduate Research Assistant
Department of Earth and Space Sciences, UCLA
Fall 2006. Teaching Assistant
Mineralogy, UCLA
Winter 2006. Teaching Assistant
Oceanography, UCLA
Spring 2005—Fall 2006. Graduate Research Assistant
Department of Earth and Space Sciences, UCLA
Winter 2005. Teaching Assistant
Oceanography, UCLA
Winter 2004—Fall 2005. Graduate Research Assistant
Department of Earth and Space Sciences, UCLA
Fall 2004. Teaching Assistant
Earth Science, UCLA
Fall 2001. Intern
Government Affairs, American Geological Institute

HONORS & AWARDS

UCLA Teaching Fellow *2011-2012*
NSF GK-12 Fellowship *2010 - 2011*
AGU Outstanding Student Presentation Award, VGP *2008*
UCLA Science Education Fellowship, California Science Center *2008*
UCLA Science Education Fellowship, California Science Center *2007*
Excellence in Teaching Award, UCLA *2006*
Cross-Training Fellowship, UCLA *2005*
Excellence in Teaching Award, UCLA *2004*

PUBLICATIONS

Shahar, A., V. J. Hilgren, E. D. Youg, Y. Fei, **C. A.**

Macris, L. Deng (2011) High-temperature Si isotope fractionation between iron metal and silicate, *Geochimica et Cosmochimica Acta* **75**, 7688-7697.

Young, E. D., E. Tonui, C. E. Manning, E. Schauble, and **C. A. Macris** (2009) Spinel-olivine magnesium isotope thermometry in the mantle and implications for the Mg isotopic composition of Earth, *Earth and Planetary Science Letters* **288**, 524-533.

ABSTRACTS

Macris, C. A., E. D. Young, C. E. Manning, and E. A. Schauble (2011) Experimental determination of equilibrium magnesium isotope fractionation between spinel, forsterite, and magnesite by the three-isotope method at 700 °C and 1 GPa, *Eos. Trans. AGU,* Fall Meet. Suppl., Abstract MR12A-02. *ORAL*

Macris, C. A., E. D. Young, C. E. Manning, and E. A. Schauble (2011) New Insights into San Carlos Mantle Xenoliths Using Iron Isotopes, *Mineralogical Magazine,* Goldschmidt Conference Abstracts, 1382. *ORAL*

Macris, C. A., E. D. Young, C. E. Manning, and E. A. Schauble (2010) Inter-mineral Iron Isotope Fractionation in San Carlos Mantle Xenoliths, *Eos. Trans. AGU,* Fall Meet. Suppl., Abstract V51B-2199. *POSTER*

Macris, C. A., E. D. Young, C. E. Manning, E. A. Schauble, and E. Tonui (2008) Inter-mineral Iron Isotope Fractionation in San Carlos Xenoliths, *Eos. Trans. AGU,* Fall Meet. Suppl., Abstract V41D-2128. *POSTER.*

Macris, C. A. and C. E. Manning (2006) The Solubility of Diopside in H2O-NaCl Fluids at 800 C and 10 kbar, *Eos. Trans. AGU*, Fall Meet. Suppl., Abstract MR43C-1091. *POSTER.*

Macris, C. A. and C. E. Manning (2005) The Solubility of Diopside in Water at 10 to 15 kbar and 650 to 900 C, *Eos. Trans. AGU*, Fall Meet. Suppl., Abstract V31C-0622. *POSTER.*

INTRODUCTION

An understanding of the composition of Earth's mantle is essential for constraining the composition of the Bulk Silicate Earth (BSE), and understanding the geological processes that continuously shape the Earth, including differentiation, metamorphism, volcanism, and crustal recycling. Though largely inaccessible, the geochemistry of Earth's mantle can be examined through a wide variety of approaches. Information about its composition comes from theoretical calculations, experimental investigation, and from direct analyses of mantle-derived rocks that have been brought to the surface, known as xenoliths. The present work contributes to our knowledge of mantle petrology and geochemistry by studying equilibrium processes governing mantle minerals and fluids through the lenses of experimental petrology and stable isotope geochemistry.

In Chapter One, I use experimental petrology techniques to investigate the solubility of the mantle mineral diopside ($CaMgSi_2O_6$) in fluids at high pressures and temperatures. The interaction of fluids with rock forming minerals in the crust and upper mantle must be understood in order to determine mass transfer from a subducting plate to the overlying mantle, and to understand the role of the fluid phase as it percolates and metasomatizes vast regions of the upper mantle, and facilitates melt production in the crust and mantle. Solubility experiments involving natural fluids and important, rock-forming minerals allow insight into the chemistry of high *P*-*T* fluids, and contribute to our overall understanding of mantle geochemistry.

In Chapter Two, I turn to collecting stable isotope data from natural samples of the mantle that have been brought to the surface by volcanism. Here I measured iron isotope compositions of five mantle xenoliths and their constituent minerals (olivine, clinopyroxene,

orthopyroxene, and spinel) from San Carlos, Arizona. Iron stable isotope ratios have the potential to provide powerful tracers for geochemical processes in the mantle, such as partial melting, metasomatism, and oxidation. Careful determination of inter-mineral fractionation of iron isotopes in these rocks is the key to applying these tracers correctly. Although the information available for iron isotope compositions of mantle minerals is growing and substantial, the information taken as a whole vary considerably, making it difficult to understand the underlying systematics governing high temperature iron fractionation between minerals at equilibrium conditions. This work contributes to the understanding of how iron isotopes partition between mantle minerals at equilibrium with applications to partial melting and mantle metasomatism.

In Chapter Three, I combine experimental petrology with stable isotope geochemistry to determine the equilibrium magnesium isotope fractionation factors between forsterite and magnesite, and between spinel and magnesite as a function of temperature at 1 GPa using a piston-cylinder apparatus. The mantle is Earth's largest reservoir of magnesium, containing > 99% of Earth's inventory of this element. It is therefore important to understand the behavior of magnesium isotopes at mantle conditions. However, there is currently a lack of information concerning Mg isotope fractionation at high temperatures, which precludes the application of a potentially powerful tracer. While recent contributions have expanded the limited information on Mg fractionation in mantle minerals, it also highlights disagreements among and between individual data sets as well as disagreements between those data sets and theoretical studies. Experimental studies provide potentially useful ways to resolve these discrepancies. The new results presented here on magnesium isotope fractionation between mantle minerals represents the first rigorous high-T experimental calibration of magnesium isotope fractionation of mantle

minerals, and are generally consistent with expectations based on crystal chemical environment of magnesium in these phases.

CHAPTER ONE

The apparent solubility of diopside in H_2O and H_2O-NaCl solutions at upper mantle conditions

Abstract

The interaction of deep fluids and rock forming minerals in the crust and upper mantle must be understood in order to determine mass transfer from a subducting plate to the overlying mantle, and to understand the role of the fluid phase as it percolates and metasomatizes vast regions of the upper mantle, and facilitates melt production in the crust and mantle. Diopside ($CaMgSi_2O_6$) is an important rock-forming mineral occurring in many crustal and mantle rocks, and is therefore an obvious candidate for solubility experiments at high pressures and temperatures. The solubility of diopside in H_2O and H_2O-NaCl solutions has been measured at 650-900°C, 0.7 to 1.5 GPa in using hydrothermal methods. Diopside was found to dissolve incongruently to forsterite plus dissolved species at all conditions investigated. The data indicate that the solubility of diopside + forsterite in pure H_2O increases with increasing pressure, temperature, and salinity. Diopside + forsterite dissolution in H_2O-NaCl displays a dependence on fluid composition that is similar to forsterite and wollastonite.

1.1 Introduction

The characterization of fluid-rock interactions in the crust and upper mantle is of paramount importance to the understanding of mass transport in dynamic earth settings such as subduction zones, regional metamorphism, and oceanic hydrothermal systems. Fluid phases in these high *P-T* environments not only determine mass transfer from a subducting plate to the

overlying mantle, but also percolate and metasomatize vast regions of the upper mantle, and facilitate melt production in the crust and mantle. Understanding the geochemistry of these fluids will facilitate greater understanding of the redistribution of material in the crust and lithosphere, the transport of mass and energy into the Earth's interior, and the conditions leading to mantle melting (e.g., Vrolijk and Myers, 1990; Todd and Evans, 1993; Grove et al., 2002, 2006, 2009; Manning, 2004a,b, 2007).

One way to learn about these fluid phases is to study fluid inclusions in high-grade rocks. The last decade has seen significant contributions to this field (e.g. Andersen and Neumann, 2001; Scambelluri and Philippot, 2001), which have substantially improved our understanding of the role of fluids in crucial geologic settings. However, fluid inclusions in rock forming minerals are relatively rare, and data collected from these inclusions may be falsely interpreted due to back-reactions during retrograde metamorphism. In other words, almost any prograde metamorphic mineral formed by devolatilization that trapped the equilibrium fluid phase in an inclusion at high pressure and temperature, also underwent retrograde metamorphism involving a back-reaction of the fluid with its mineral host. The result is often a retrograde assemblage consisting of OH-minerals and/or carbonates, and a fluid that is potentially dramatically altered from its original composition and density (Heinrich and Gottschalk, 1995). Therefore it is necessary to have reliable experimental data to constrain the chemistry of high *P-T* fluids in equilibrium with relevant minerals and mineral assemblages by conducting systematic solubility experiments on rock-forming minerals.

There is an increasingly comprehensive data set becoming available on mineral solubility in aqueous fluids at high pressures and temperatures from experimental studies using weight loss methods and piston-cylinder apparatuses. Newton and Manning (2010) reviewed of these types

of experiments and their implications for deep-crustal and upper-mantle metasomatism, focusing on studies involving quartz (SiO_2) solubility in fluids of various compositions, and some of the other important rock-forming minerals including wollastonite ($CaSiO_3$) and corundum (Al_2O_3). Some other studies of note here contributed to the data set by measuring the solubilities of grossular ($Ca_3Al_2Si_3O_{12}$), andradite ($Ca_3Fe_2Si_3O_{12}$), and most recently, forsterite (Mg_2SiO_4) (Newton & Manning, 2007; Wykes et al., 2008; and Wykes et al., 2011).

Diopside ($CaMgSi_2O_6$) is also an important rock-forming mineral occurring in many crustal and mantle rocks. It is found in ultramafic (kimberlite and peridotite) igneous rocks, and is common in mafic rocks, such as olivine basalt and andesite. Diopside is also found in a variety of metamorphic rocks, such as in contact metamorphosed skarns developed from high silica dolomites. It is an important mineral in the Earth's mantle and is common in peridotite xenoliths erupted in kimberlite and alkali basalt.

Despite the widespread occurrence of diopside, it's solubility in natural fluids such as H_2O and H_2O-NaCl has not been constrained at all relevant pressures and temperatures. Shmulovich et al. (2001) measured diopside solubility at 650°C and 0.5 GPa in pure water and in a 50% NaCl solution. They reported apparent solubilities of 0.0023 and 0.0254 molal for diopside in pure water and in the 50% NaCl solution respectively. These measurements contribute to the understanding of diopside in equilibrium with natural fluids such as those present in subduction zones. However, additional experiments need to be done in order to quantify more systematically the solubility of this ubiquitous mineral in high *P*-*T* environments. For this study, I measured diopside solubility in pure water from 0.7 to 1.5 GPa and 650 to 900°C, and in H_2O-NaCl solutions at 800 °C and 10 kbar and NaCl concentrations approaching halite saturation. Results show that diopside dissolves incongruently at all conditions, leaving behind a residue of

forsterite while the wollastonite component dissolves into the fluid. The present work, in combination with solubility studies of wollastonite and forsterite, provide an opportunity to directly compare mobilities of Mg^{2+} and Ca^{2+} in metamorphic systems.

1.2 Experimental Methods

The starting material used in these experiments was from single a gem-quality natural diopside specimen obtained from the mineral collection of the Department of Earth and Space Sciences at the University of California, Los Angeles. The starting diopside contains <1 wt.% other constituents (Table 1.1). In these experiments, small chips of the gem-quality diopside (0.2-3.0 mg) were placed in an inner, 1.6 mm outer diameter, Pt capsule, which was then crimped shut on both ends and perforated to allow fluid penetration. The inner capsule was then placed inside of an outer, 3.5 mm outer diameter, Pt capsule with 0.18 mm wall thickness, along with varying amounts of H_2O and NaCl to reach desired salinities. The outer capsule was then sealed with an arc welder and heated in a 115 °C oven. After 3 hours, the capsule was weighed again to ensure there is no water loss.

Once the integrity of the seal was established, the capsule was placed horizontally into a 25.4 mm diameter NaCl-graphite furnace assembly and packed firmly with powdered NaCl. A thin piece of Pt was placed on top of the packed capsule to protect thermocouple puncture. Temperature was monitored with $Pt/Pt_{90}Rh_{10}$ thermocouples (±3°C estimated precision). A Heise gauge (±0.01 GPa estimated precision) monitored pressure of the assembly inside the end-loaded piston-cylinder apparatus. Run times varied from 4 to 96 hours, after which power to the press was cut, quenching the charge to temperatures <100°C in approximately 30 s. The outer capsule was then retrieved, cleaned, pierced with a needle, and dried for 15 minutes at 110°C,

and then 15 minutes at 350°C. The outer capsule was then carefully opened to extract the inner capsule, which was cleaned and weighed. The contents of the inner capsule were then removed, examined optically under a binocular microscope, and weighed. Selected run products were mounted and examined with a scanning electron microscope for composition and textural characteristics of residual crystals and quench material.

1.3 Experimental Results

Run products from all experiments consisted of the original diopside crystal with smaller forsterite crystals growing on its surface. The forsterite occurs as microscopic (~25-100 μm) sub- to euhedral residual crystals on diopside grain surfaces (Figure 1.1a) and in some runs also on the walls of inner capsules. From this textural evidence, I conclude that diopside dissolves incongruently to forsterite + dissolved species at all conditions investigated. Visually estimated forsterite mass is very small relative to bulk solubility (less than 5% of the crystal's weight loss). In addition, SEM analyses show acicular sprays of wollastonite (in pure H_2O runs) and wollastonite + enstatite (in H_2O-NaCl runs) occurring on grain surfaces (Figure 1.1b), along with minor silica material, which forms as both small spheres ("fish roe") and an amorphous coating on some crystal surfaces. These materials form a randomly distributed coating on the surface of diopside and forsterite crystals, and in some cases, coat the walls of the inner and outer capsules. The morphology, random distribution, and abundance of these materials lead us to interpret these fine crystals and amorphous materials as quench phases, which were in dissolved in solution at high *P*-*T* conditions. These quench materials are typical of high *P*-*T* solubility studies of silicate minerals (e.g., Newton and Manning, 2006, 2007). The formation of enstatite quench crystals in run products from H_2O-NaCl experiments, but not observed in pure H_2O runs in this study,

indicates a substantial increase in Mg^{2+} solubility in brines relative to pure H_2O.

Experiments in pure H_2O at 700 °C and varying times showed that diopside plus forsterite plus fluid reached constant solubility by 12 h; it is therefore assumed that run times ≥12 h have attained equilibrium. SEM analyses revealed that in several experiments small diopside crystals nucleated and grew in the outer capsule or on the walls of the inner capsule due to fluid convection within the charge. These experiments yielded erroneously high solubilities and were omitted from final plots and equation calculations, as justified by discussions of 'vapor-transport crystals' by Newton and Manning (2006) and Tropper and Manning (2007).

Because diopside dissolves incongruently at all conditions investigated thus far, the weight change of diopside crystals in our experiments did not measure the solubility of diopside sensu stricto, but rather the solubility of the new equilibrium mineral assemblage, diopside + forsterite. Thus all solubility measurements are reported here as apparent solubilities. Results from all experiments are given in Table 1.2 and are discussed below.

1.3.1 Diopside-H_2O Experiments

The solubility of diopside + forsterite in pure Millipore H_2O increases with increasing pressure and temperature. Experiments were conducted at 0.7 to 1.5 GPa and 650 to 900 °C. At 1.0 GPa, the apparent solubility increases from 0.004 molal at 650 °C to 0.012 molal at 900 °C (Figure 1.2). At 800° C and 0.7 to 1.5 GPa, apparent solubility increases from 0.002 to 0.015 molal (Figure 1.3). These preliminary data are described by the equation:

$$\log m_{\text{di app}} = -1.35669 + -1945.64/T + 1.00554P, \quad (1)$$

where $m_{\text{di app}}$ is the apparent solubility of diopside in molal, T is in K and P is in GPa. This equation illustrates the inverse behavior of solubility with temperature and direct relationship of solubility with pressure. Average absolute deviation between data and fit is 2.6% relative (maximum absolute deviation is 6.9% relative). This equation predicts an apparent solubility of ~0.0011 molal for diopside in pure water at 650°C, 0.5 GPa. Shmulovich et al. (2001) experimentally determined an apparent solubility of ~0.0023 molal at these conditions (Figure 1.4). The difference between these values may result from undetected vapor transport crystals in the Shmulovich group's experiment, which would give an erroneously high solubility measurement.

1.3.2 Diopside-H_2O-NaCl Experiments

The apparent solubility of diopside undergoes significant enhancement with NaCl concentration, rising rapidly from 0.0076 molal in pure H_2O and then leveling off to a maximum of ~0.13 molal approaching halite saturation. These data yield the equation:

$$m_{\text{di app}} = 0.0076 + 0.0186(X_{\text{NaCl}}) + 0.1597(X_{\text{NaCl}})^{1/2}, \quad (2)$$

where X_{NaCl} is mole fraction NaCl in solution. Figure 1.5 shows that the enhancement of diopside solubility in the presence of H_2O-NaCl fluids is much less than that of wollastonite at these conditions, which rises from ~0.0167 molal in pure water to >0.5 molal at halite saturation (Newton and Manning, 2006), and much greater than that of forsterite, which rises from ~0.0021 to ~0.03 molal in this range (Wykes et al., 2011).

The solubility enhancement factor of diopside in H_2O-NaCl relative to that in pure H_2O,

$X/X°$, passes through a maximum at $X_{NaCl} \approx 0.23$ and then declines towards halite saturation ($X_{NaCl} \approx 0.58$). The maxima for wollastonite and forsterite are approximately 0.38 and 0.26 respectively. Figure 1.6 shows that the general shape of the diopside solubility enhancement curve more closely resembles that of forsterite than wollastonite. Also the diopside maximum is much closer to forsterite than wollastonite. Therefore, diopside seems to behave more like forsterite than wollastonite in the presence of H_2O-NaCl fluids at high *P-T* conditions.

1.4 Discussion

1.4.1 Incongruent Dissolution

Based on the measurements and textural observations presented here, I conclude that, at the elevated pressures and temperatures of this study, diopside dissolves incongruently in pure H_2O and in H_2O-NaCl solutions. The result is diopside in equilibrium with forsterite and a fluid containing dissolved NaCl, SiO_2, $CaSiO_3$, and to a much lesser degree, Mg_2SiO_4 (from the small amount of dissolved residual forsterite). Preliminary work on forsterite solubility indicates that it dissolves very slightly incongruently in pure H_2O (yielding minor brucite + fluid), but congruently in H_2O-NaCl solutions at 800°C and 1.0 GPa (Wykes et al., 2011). However, due to the low solubility of forsterite, and the small amount of forsterite residue present in our experiments, we assume that the amount of Mg_2SiO_4 in solution does not materially influence the solubility of the wollastonite and quartz contributions to solution.

Incongruent dissolution is not surprising in the case of diopside, given the known solubilities of quartz, wollastonite, and forsterite. As shown in Figure 1.5, at all relevant conditions, quartz has the highest solubility, followed by wollastonite, which has a much higher solubility than does forsterite, with diopside plotting in between them (Newton and Manning,

2000; Newton and Manning, 2006; Wykes et al., 2011). Also, according to thermodynamic calculations of metasomatic phase relations in the system $CaO\text{-}MgO\text{-}SiO_2\text{-}H_2O\text{-}NaCl$, the assemblage diopside + forsterite exists in equilibrium with aqueous fluids containing a range of dissolved silica consistent with that of our experiments at high pressures and temperatures (Newton and Manning, 2000). Assuming negligible amounts of forsterite dissolve into solution, the dissolution equilibrium for diopside in the presence of forsterite can be written as

$$\underset{\text{diopside}}{2\ CaMgSi_2O_6} = \underset{\text{forsterite}}{Mg_2SiO_4} + 2\ CaSiO_{3,\,aq} + SiO_{2,aq} \qquad (3)$$

1.4.2 Solubility enhancement by NaCl

Comparisons of solubility data of rock-forming minerals in $H_2O\text{-}NaCl$ solutions versus pure H_2O reveal a general pattern of solubility enhancement at high *P* and *T*, with quartz being a notable exception (Figure 1.6). Newton and Manning (2010) discuss the significance of solubility enhancement by NaCl of some important rock-forming minerals including quartz, wollastonite, corundum, and grossular at length. The addition of diopside solubility data in pure water and saline solutions by the present work, allows for the comparison of the NaCl enhancement factor of diopside with those of its constituent parts: quartz, wollastonite, and forsterite.

1.5 Conclusions

These experimental results allow an initial evaluation of changes in apparent diopside solubility along specific fluid flow paths to be expected in high *P* environments. In subduction zones, fluid moving towards the earth's surface from the slab to the mantle wedge heats up as it

decompresses. Because temperature enhances solubility more than pressure in this system, we can predict that as a fluid moves from slab to wedge and therefore decompresses and heats up, solubility will increase despite decreasing pressure. The resulting fluid will be enriched in Ca and Si, but low in Mg, which is highly insoluble in H_2O. These results are consistent with theoretical predictions on the composition of fluids in equilibrium with eclogites (Manning, 1998), experimental investigations on fluid compositions in equilibrium with high-pressure mantle rocks (Schneider and Eggler, 1986; Ayers et al., 1997), and are also manifested in vein minerals in blueschists and eclogites which are Na-Ca-Al-Si rich (Gao and Klemd, 2001; Becker et al., 1999) and poor in Mg.

At all X_{NaCl} investigated, the solubility of wollastonite is greater than diopside, which in turn is greater than forsterite. As X_{NaCl} increases, these solubility differences are amplified. Brines in contact with ultramafic rocks at high pressures and temperatures will preferentially strip Ca relative to Mg, resulting in a Ca/Mg ratio of >1 in solution. These results provide a foundation for quantifying the nature of interaction between ultramafic rocks and complex brines in the deep crust and upper mantle.

Oxide	Wt.%	2σ
SiO_2	54.07	0.08
TiO_2	0.01	0.01
Al_2O_3	0.01	0.00
Cr_2O_3	0.02	0.01
FeO	0.40	0.02
MgO	18.18	0.02
CaO	26.21	0.04
MnO	0.35	0.01
Na_2O	0.02	0.00
Total	99.29	0.00

Table 1.1 Composition of diopside starting material (in wt.%). Average of 22 analyses. Errors are 2 standard error.

Run	P (GPa)	T (°C)	Time (h)	H_2O out (mg)	NaCl in (mg)	X_{NaCl}	Di in (mg)	Di out (mg)	$m_{di\ app}$ (mol/kgH_2O)
gdi1	1.0	750	21	35.73	0	0	1.01	0.96	6.02×10^{-3}
gdi2	1.0	700	8	35.82	0	0	1.11	1.08	4.59×10^{-3}
gdi3	1.0	700	4	35.96	0	0	2.09	2.06	4.37×10^{-3}
gdi5	1.0	650	12	36.13	0	0	0.89	0.85	4.02×10^{-3}
gdi7	1.0	800	12	35.72	0	0	1.02	0.96	7.65×10^{-3}
gdi8	1.0	850	16	36.70	0	0	0.49	0.41	9.95×10^{-3}
gdi9	1.0	900	12	26.95	0	0	1.14	1.08	1.18×10^{-2}
gdi10	1.0	850	12	35.84	0	0	0.68	0.61	8.99×10^{-3}
gdi12	1.5	800	15	33.75	0	0	0.83	0.72	1.54×10^{-2}
gdi13	1.2	800	12	34.21	0	0	0.41	0.33	1.17×10^{-2}
gdi15	0.7	800	20	21.68	0	0	0.43	0.42	2.02×10^{-3}
DB4	1.0	800	12	28.79	43.23	0.32	2.13	1.46	1.08×10^{-1}
DB5	1.0	800	12	20.33	64.83	0.50	2.10	1.55	1.23×10^{-1}
DB6	1.0	800	12	38.36	6.93	0.05	0.51	0.19	3.86×10^{-2}
DB9	1.0	800	48	36.80	12.34	0.09	1.41	0.92	6.07×10^{-2}
DB10	1.0	800	12	28.00	22.24	0.20	1.62	1.07	9.59×10^{-2}
DB8	1.0	800	5	36.60	12.84	0.10	1.30	0.87	5.46×10^{-2}
DB11	1.0	800	96	36.01	2.15	0.02	1.63	1.48	1.92×10^{-2}

Table 1.2 Experimental results. Propagation of weighing errors of 3 μg (H_2O and NaCl) and 0.25 μg (diopside) yields uncertainties in X_{NaCl}, $m_{di\ app}$, of $3 \times 10^{-5}$and 1×10^{-4}.

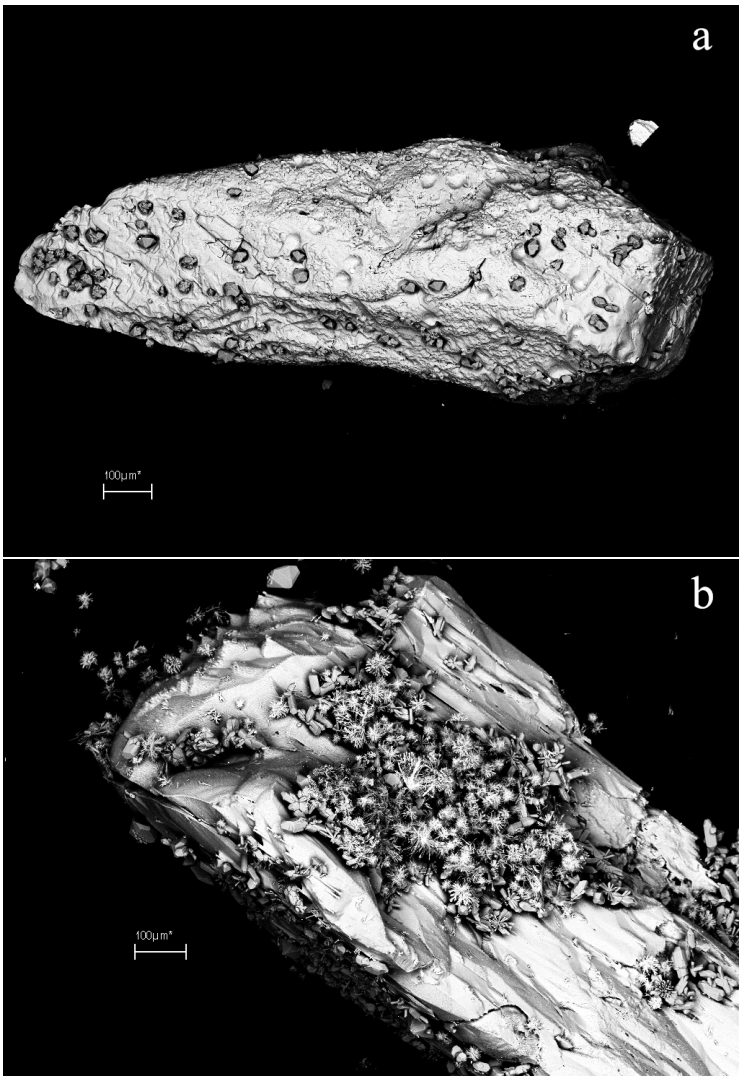

Figure 1.1 Backscattered electron (BSE) images of run products. (a) Image of diopside crystal from run gdi5 showing subhedral forsterite grains and etch pits. (b) Diopside crystal from run DB4 with subhedral forsterite crystals partially covered by acicular sprays of quench wollastonite and enstatite.

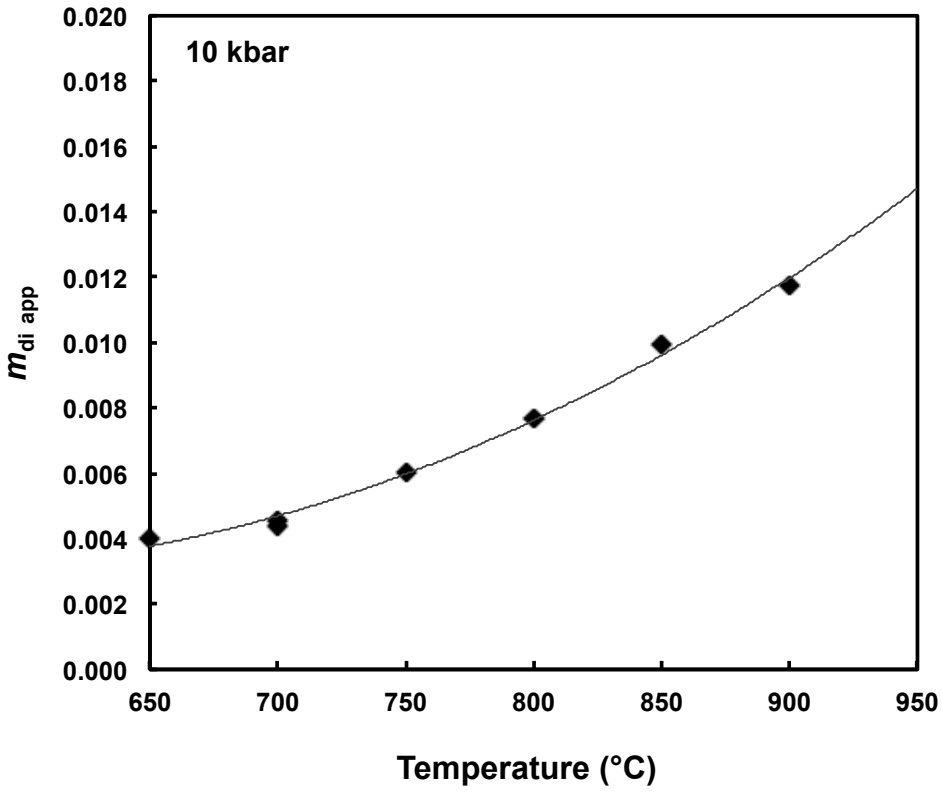

Figure 1.2 Apparent solubility of diopside in pure water at 1.0 GPa and temperatures ranging from 650 to 900°C. Errors are smaller than symbols.

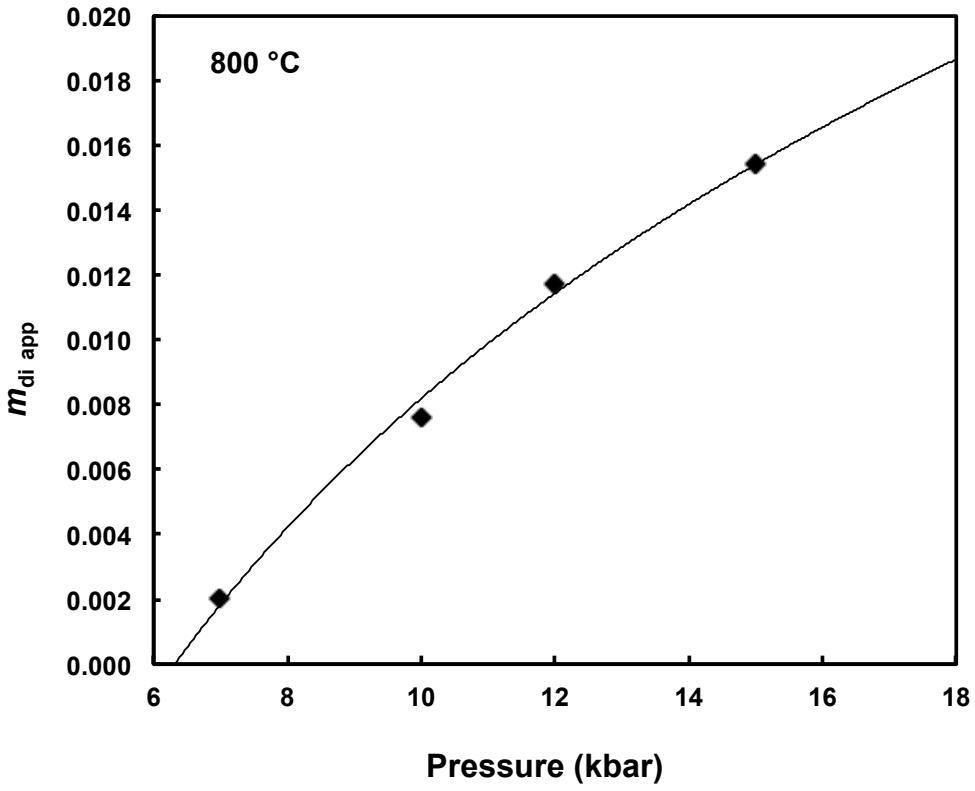

Figure 1.3 Apparent solubility of diopside in pure water at 800°C and pressures ranging from 7 to 15 kbar. Errors are smaller than symbols.

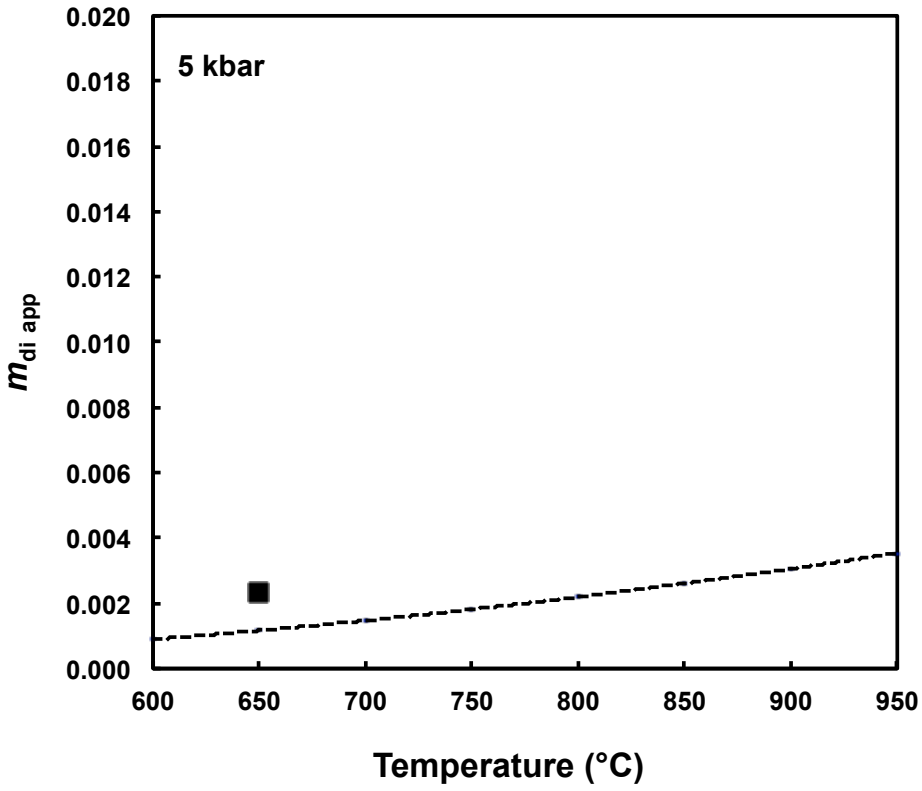

Figure 1.4 Comparison of data from Shmulovich et al. (2001) and diopside solubility predicted by equation (1) at 5 kbar in pure water. Error smaller than symbol.

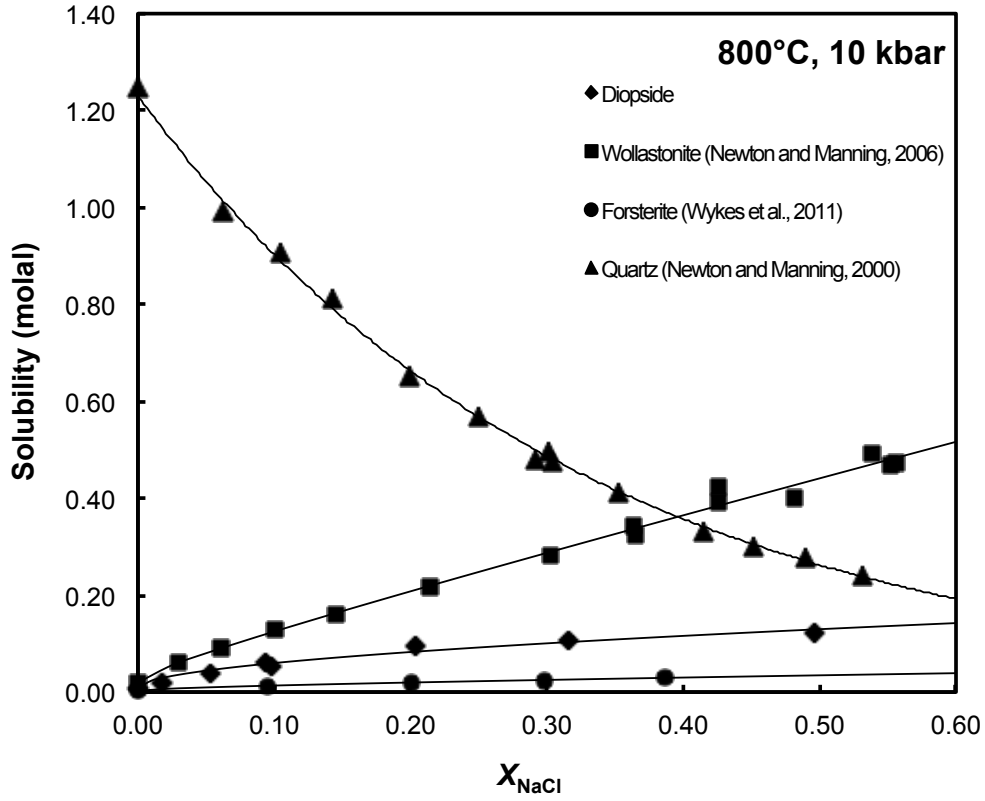

Figure 1.5 Solubilities of diopside, wollastonite (Newton and Manning, 2006), and forsterite (Wykes et al., 2011), and quartz (Newton and Manning, 2000) with varying X_{NaCl} at 800°C and 10 kbar. Errors are smaller than symbols.

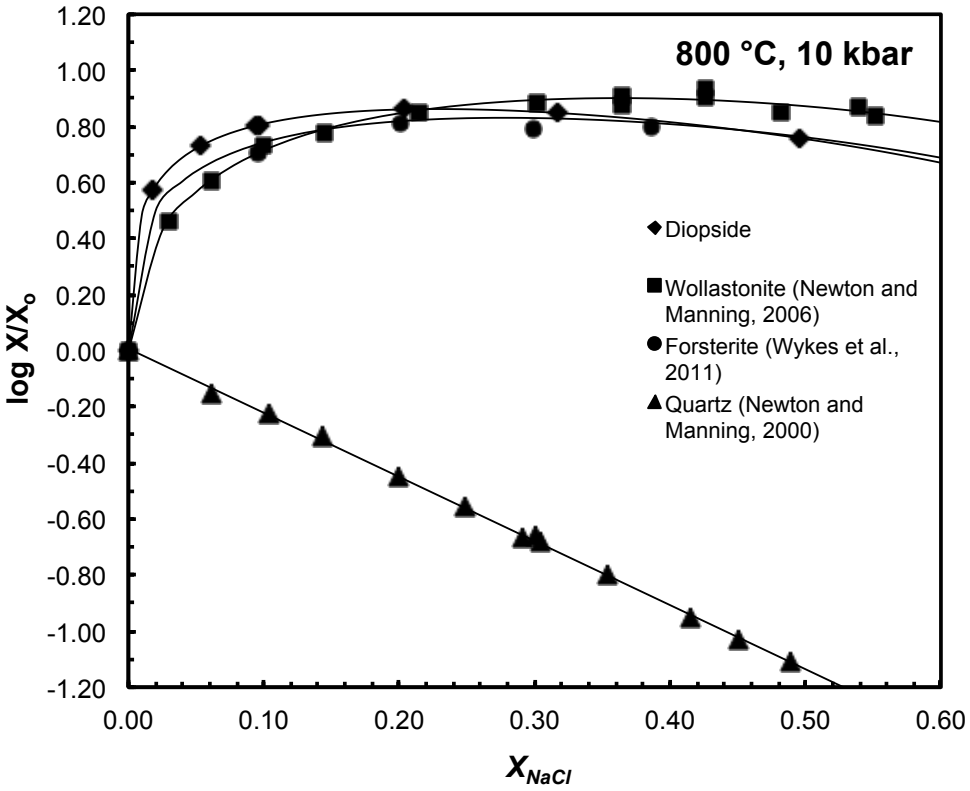

Figure 1.6 Solubility enhancement factors of diopside, wollastonite, and forsterite in NaCl-H2O solutions at 800°C and 10 kbar, expressed as the log of the ratio of mole fraction at a given NaCl concentration to that in pure H_2O (X/X_o). Mole fractions calculated assuming complete dissociation of NaCl to Na^+ and Cl^-, according to Newton and Manning (2006). Curves show empirical fits to solubility data for diopside (Eq. (2)), wollastonite (Newton and Manning, 2006), and forsterite (Wykes et al., 2011), and quartz (Newton and Manning, 2000). Errors are smaller than symbols.

References

Andersen, T. and Neumann, E. (2001) Fluid inclusions in mantle xenoliths. *Lithos* **55**, 301-320.

Ayers, J., Dittmer, S.K. and Layne, G.D. (1997) Partitioning of elements between peridotite and H_2O at 2.0-3.0 GPa and 900-1100^oC, and application to models of subduction zone processes. *Earth and Planetary Science Letters* **150**, 381-398.

Becker, H., Jockum, K.P., and Carlson, R.W. (1999) Constraints from high-pressure veins in eclogites on the composition of hydrous fluids in subduction zones. *Chemical Geology* **160**, 291-308.

Gao, J. and Klemd, R. (2001) Primary fluids entrapped at blueschist to eclogite transition: evidence from the Tianshan meta-subduction complex in northwestern China. *Contributions to Mineralogy and Petrology* **142**, 1-14.

Grove, T.L., Parman, S.W., Bowring, S.A., Price, R.C., Baker, M.B. (2002) The role of an H_2O-rich fluid component in the generation of primitive basaltic andesites and andesites from the Mt. Shasta region, N California. *Contributions to Mineralogy and Petrology* **142**, 375-396.

Grove, T.L., Chatterjee, N., Parman, S.W., Me´dard, E. (2006) The influence of H_2O on mantle wedge melting. *Earth and Planetary Science Lett*ers **249**, 74–89.

Grove, T.L., Till, C.B., Lev, E., Chatterjee, N., Me´dard, E. (2009) Kinematic variables and water transport control the formation and location of arc volcanoes. *Nature* **459**, 694.

Heinrich, W. and Gottschalk, M. (1995) Metamorphic reactions between fluid inclusions and mineral hosts. I. Progress of the reaction calcite + quartz = wollastonite + CO_2 in natural wollastonite-hosted fluid inclusions. *Contributions to Mineralogy and Petrology* **122**, 51-61.

Manning, C. E. (1998) Fluid composition at the blueschist–eclogite transition in the model system Na_2O–MgO–Al_2O_3–SiO_2–H_2O–HCl. *Swiss Bulletin of Mineralogy and Petrology* **78**, 225–242.

Manning, C.E. (2004a) Polymeric silicate complexing in aqueous fluids at high pressure and temperature, and its implications for water-rock interaction. in ‘‘Water-Rock Interaction, Proceedings of the Eleventh International Symposium on Water-Rock Interaction’’, R.B. Wanty and R.R. Seal II, eds., Taylor & Francis Group, London, 45-49.

Manning, C.E. (2004b) The chemistry of subduction-zone fluids. *Earth and Planetary Science Letters* **223**, 1–16.

Newton, R. C., and Manning, C. E. (2000) Metasomatic phase relations in the system CaO-MgO-SiO_2-H_2O-NaCl at high temperatures and pressures. *International Geology Review* **42**, 152-162.

Newton, R. C., and Manning, C. E. (2000) Quartz solubility in concentrated aqueous NaCl solutions at deep crust-upper mantle metamorphic conditions: 2-15 kbar and 500-900 °C. *Geochimica et Cosmochimica Acta*, **64**, 2993-3005.

Newton, R. C. and Manning, C. E. (2006) Solubilities of corundum, wollastonite and quartz in H2O--NaCl solutions at 800 °C and 10 kbar: Interaction of simple minerals with brines at high pressure and temperature. *Geochimica et Cosmochimica Acta* **70**, 5571-5582.

Newton, R. C., and Manning, C. E. (2007) Solubility of grossular, $Ca_3Al_2Si_3O_{12}$, in H_2O-NaCl solutions at 800°C and 10 kbar, and the stability of garnet in the system $CaSiO_3$-Al_2O_3-H_2O-NaCl. *Geochimica et Cosmochimica Acta* **71**, 5191-5202.

Newton, R. C., and Manning, C. E. (2010) Role of saline fluids in deep-crustal and upper-mantle

metasomatism: insights from experimental studies. *Geofluids* **10**, 58-72.

Scambelluri, M. and Philippot, P. (2001) Deep fluids in subduction zones. *Lithos* **55**, 213-227.

Schneider, M.E. and Eggler, D.H. (1986) Fluids in equilibrium with peridotite minerals: Implications for mantle metasomatism. *Geochimica et Cosmochimica Acta* **50**, 711-724.

Shmulovich, K., Graham, C. and Yardley, B. (2001) Quartz, albite and diopside solubilities in H2O-NaCl and H2O-CO2 fluids at 0.5-0.9 GPa. *Contributions to Mineralogy and Petrology* **141**, 95-108.

Todd, C.S. and Evans, B.W. (1993) Limited fluid-rock interaction at marble-gneiss contacts during Cretaceous granulate–facies metamorphism, Seward Peninsula, Alaska. *Contributions to Mineralogy and Petrology* **114**, 27-41.

Tropper, P., and Manning, C. E. (2007) The solubility of fluorite in H_2O and H_2O-NaCl at high pressure and temperature. *Chemical Geology* **242**, 299-306.

Vrolijk, P. and Myers, G. (1990) Fluid pressure history in Subduction zones: evidence from fluid inclusions in the Kodiak Accretionary Complex, Alaska. in ‘‘Studies in Geophysics: The Role of Fluids in Crustal Processes’’, Geophysical Study Committee, Commission on Geosciences, Environment, and Resources, National Research Council eds., National Academy Press, Washington, DC, 148–157.

Wykes, J. L., Newton, R. C., and Manning, C. E. (2008) Solubility of andradite, $Ca_3Fe_2Si_3O_{12}$, in a 10 mole % NaCl solution at 800°C and 10 Kbar: implications for the metasomatic origin of grandite garnet in calc-silicate granulites. *American Mineralogist* **93**, 886-892.

Wykes, J. L., Newton, R. C., and Manning, C. E. (2011) Forsterite solubility in NaCl-H2O fluids at upper mantle P-T conditions. *Eos, Transactions of the American Geophysical Union*

92, Abstract U53B-0059.

CHAPTER TWO

Inter-mineral iron isotope fractionation in San Carlos mantle xenoliths: a crystal chemical perspective

Abstract

Iron isotopic compositions of mantle minerals can provide powerful tracers for geochemical processes in the deep Earth, such as partial melting, metasomatism, and oxidation. Predictions of equilibrium fractionation from theory and Mössbauer data conflict, making interpretation high of high *P-T* Fe isotope data from mantle lithologies uncertain. To address this, I studied inter-mineral iron isotopic fractionation of minerals from five distinct mantle-xenolith lithologies from San Carlos, Arizona. The samples represent a broad range of mineral modes and include a clinopyroxenite, a websterite, a lherzolite, a harzburgite, and a dunite. All samples except for the websterite are Group I inclusions, which are typically rich in Mg and Cr, and consist of mainly olivine-rich rocks. Each xenolith exhibits Fe-isotopic variation between minerals in a single sample, and between samples. In all cases where spinel and olivine coexist in a sample, the $^{57}Fe/^{54}Fe$ of spinel is greater than that of the corresponding olivine, agreeing with expectations for equilibrium fractionation from theory. $^{57}Fe/^{54}Fe$ values of clinopyroxenes and orthopyroxenes from the xenoliths show no clear systematics. I interpret this to be a result of varying degrees of metasomatism, perhaps involving interaction with a melt. A strongly linear reverse correlation between olivine content and bulk rock $^{57}Fe/^{54}Fe$ was found for all samples except the websterite (the only type II xenolith measured). The strong linear relationship among Group I samples, and deviation from the trend in websterite, suggests Fe isotope systematics can be added to the list of differences used to distinguish between Group I and Group II xenoliths.

2.1 Introduction

Iron stable isotope ratios have the potential to provide powerful tracers for geochemical processes in the mantle, such as partial melting, metasomatism, and oxidation. Careful determination of inter-mineral fractionation of iron isotopes in these rocks is the key to applying these tracers correctly. Although the data available for iron isotope compositions of mantle minerals is growing and substantial, the data taken as a whole vary considerably and make it difficult to understand the underlying systematics governing high temperature iron fractionation between minerals at equilibrium conditions. Fe isotope data of mantle xenoliths reported in previous studies show variations between minerals within a single sample and between mantle xenoliths (Zhu et al., 2002; Beard and Johnson, 2004; Poitrasson et al., 2004; Williams et al., 2004, 2005, 2009; Schoenberg and von Blanckenburg, 2006; Weyer et al., 2005; Weyer and Ionov, 2007; Dauphas et al., 2009; Zhao et al., 2010; Huang et al., 2011; Zhao et al., 2012).

Williams et al. (2005) reported significant variations in $^{57}Fe/^{54}Fe$ of a large suite of mantle rocks relative to the IRMM-14 standard and their constituent minerals, resulting in some ambiguity concerning the fractionation of iron between the different phases. For example, the study determined that in some mantle rocks, spinel was higher in $^{57}Fe/^{54}Fe$ than olivine, while in other rocks olivine has the higher $^{57}Fe/^{54}Fe$ values. Iron isotope data from Zhu et al. (2002) also identified some variation in the $^{57}Fe/^{54}Fe$ of the mantle minerals olivine and clinopyroxene from three different xenoliths. They did not measure the iron isotope compositions of spinels in any samples and only show orthopyroxene values for two out three, which exhibit no variation. More recently, Zhao et al. (2010) measured small but distinguishable Fe isotopic variations in spinel lherzolites and clinopyroxenites from the North China Craton. Their inter-mineral Fe

isotope fractionation measurements showed no clear systematics within individual xenoliths. In other words, the current inter-mineral Fe isotope fractionation data set exhibit no trends regarding order of degree of enrichment of heavy iron isotopes among constituent minerals (Figure 2.1).

The variability in iron isotope compositions of mantle minerals from different areas may be due in part to the intrinsic petrologic variability inherent in different sample localities. For example the samples measured by Williams et al. (2005) come from very diverse petrological locales including sub-continental margin mantle, sub-continental mantle lithosphere, and sub-arc mantle. Some variations can be explained by assuming disequilibrium between phases as a result of metasomatism or interaction with a melt. Analytical artifacts must also be considered when evaluating discrepancies between data sets. For example, incomplete purification of Fe by column chemistry can lead to spurious Fe isotope measurements, which will affect each sample differently depending on the degree of incompleteness of purification, including the type and amount of polluting cations present.

Evaluation of the origins of the discrepancies is further hindered by disagreement among predictions for inter-mineral fractionation signs and magnitudes. Qualitative rules governing equilibrium stable isotope fractionation (e.g. Schauble, 2004; Young et al., 2009) suggest that spinel should concentrate the heavy isotopes of iron relative to olivine and pyroxenes. The opposite is found by modeling of Mössbauer and inelastic nuclear resonant x-ray scattering (INRXS) data (Polyakov, 1997; Polyakov and Mineev, 2000). These opposing predictions, combined with the variability seen so far in natural samples, raises important questions about Fe isotopes in the mantle. Are there systematic Fe isotope fractionation trends among mantle minerals that geochemists can use to aid in rigorously applying Fe isotopes as tracers of high

temperature geological processes in the mantle? For example, is spinel in the mantle enriched or depleted in heavy Fe isotopes relative to olivine and pyroxene?

In order to address these questions, I studied inter-mineral iron isotopic fractionation of minerals from the well-characterized mantle xenoliths of San Carlos, Arizona (Frey and Prinz, 1978), in order to better understand high temperature inter-mineral iron isotope fractionation and its controls. San Carlos xenoliths are among the most widely studied samples of mantle lithosphere because they are abundant and easily sampled, and they form a coherent, well-understood and representative petrologic record of mantle lithospheric processes (Galer and O'Nions, 1988). My goal is to establish the fractionation of iron isotopes between the minerals of a suite of well characterized xenoliths, especially fractionation between the minerals spinel, olivine, and pyroxene, with a focus on the crystal chemical principles that apply to these mineral structures and the way they govern the fractionation of iron isotopes.

2.2 Samples and background

The samples studied here include olivine (Ol), clinopyroxene (Cpx), orthopyroxene (Opx), and spinel (Spl) from three peridotite and two pyroxenite xenoliths from the San Carlos ultramafic inclusion locality in southeastern Arizona, USA. San Carlos ultramafic inclusions occur mostly as gravity settled masses exposed in lower parts of a Tertiary or Quaternary basalt flow related to a volcanic cone. The majority of the xenoliths can be classified into two groups, referred to as Groups I and II, which differ in a number of ways. Group I inclusions are mainly olivine-rich rocks, but orthopyroxene- and clinopyroxene-rich samples are also present. A major feature of San Carlos Group I xenoliths is the common occurrence pyroxene-rich rocks interlayered with lherzolites. Pyroxenes and spinels in Group I rocks are typically Cr-rich and

TiO_2 poor, and silicates generally have Mg# > 0.85. Group II xenoliths are highly variable in terms of mineral proportions and compositions, and include spinel clinopyroxenites, spinel olivine websterites, and many others. Pyroxenes in Group II xenoliths are usually Al_2O_3- and TiO_2-rich, but Cr-poor. Spinels are generally Al-rich and Cr-poor, and silicates range widely in Mg#, but are typically <0.85. These differences between Groups I and II inclusions result from distinct petrogenetic histories (Frey and Prinz, 1978).

All San Carlos xenoliths in the present study were borrowed from the Smithsonian Museum's collection, except for the spinel lherzolite, which came from our private collection. The five distinct mantle-xenolith lithologies were chosen to represent a broad range of mineral modes and include a clinopyroxenite, a websterite, a lherzolite, a harzburgite, and a dunite. Thin sections taken from each xenolith were analyzed by petrographic microscope and electron microprobe to determine average chemical composition and modes of constituent minerals (Table 2.1). Backscattered electron (BSE) images of each xenolith are presented in Figure 2.2.

2.2.1 Peridotite xenoliths

The three peridotite xenoliths chosen for this study represent a wide range of mineralogies including a spinel lherzolite (CEM1-3), a harzburgite (111-312-37), and a dunite (111-312-26). Sample CEM1-3 is a spinel lherzolite composed of 62% Ol, 24% Opx, 13% Cpx, and <1% chromian Spl as determined by electron microprobe. A 100×100 grid of spot analyses was programmed to give quantitative oxide percentages for 10,000 spots on the sample. The average mineral formula for spinel in this xenolith was also calculated from separate quantitative electron microprobe analyses (this is true for all mineral formulas presented here) to be $(Mg_{0.73}Fe^{2+}_{0.27})(Al_{1.19}Cr_{0.74}Fe^{3+}_{0.06})O_4$. Mineral formulas are determined by charge balance

assuming no vacancies after Johannsen (1931). Notable is the relatively high concentration of Cr as well as the relatively small amount of Fe^{3+} assigned to the octahedrally coordinated site. Therefore, the iron in the spinel of CEM1-3 is dominantly ferrous and tetrahedrally coordinated. BSE images of CEM1-3 reveal no petrographic signs of metasomatism or interaction with a melt (Figure 2.2a). Young et al. (2009) found that, in this same xenolith, heavy Mg isotopes tend to concentrate in spinel compared to the other minerals and Mg isotope thermometry records a spinel-olivine equilibration temperature of 815 ± 11 °C.

Sample 111-312-37 is a harzburgite, consisting of 69% Ol, 27% Opx, 4% Cpx, and <1% chromian Spl. The calculated average spinel formula is $(Mg_{0.72}Fe^{2+}_{0.28})(Al_{1.04}Cr_{0.90}Fe^{3+}_{0.05})O_4$, which again suggests high chromium content and relatively low trivalent iron in octahedral coordination versus divalent iron in tetrahedral coordination. BSE images of this harzburgite show partially altered regions at the edge basalt/xenolith contact, a clear sign of post-entrainment interaction with the host basalt (Figure 2.2b).

Sample 111-312-26 is a dunite with 69% Ol, 27% Opx, 4% Cpx, and <1% Spl. The average spinel formula for this dunite is $(Mg_{0.79}Fe^{2+}_{0.21})(Al_{1.54}Cr_{0.42}Fe^{3+}_{0.04})O_4$, which reveals that the Spl in this dunite is more than 50% poorer in chromium than Spl in the other two peridotite xenoliths. Most of the iron is divalent and in the tetrahedral site. BSE images of this xenolith also show late stage alteration by the host basaltic magma (Figure 2.2c), similar to that seen in the harzburgite.

2.2.2 Pyroxenite xenoliths

Two pyroxenite xenoliths were chosen for this study: a clinopyroxenite (SC-1-66), and an olivine websterite (SC-1-70). The clinopyroxenite contains 95% Cpx, 5% Opx, <1% spinel, and no olivine. The quantitative average mineral formula for spinel in this rock is

$(Mg_{0.71}Fe^{2+}_{0.29})(Al_{1.45}Cr_{0.50}Fe^{3+}_{0.03})O_4$. These spinels are similar in chromium content to those in the dunite. The websterite is composed of 58% Opx, 32% Ol, 10% Cpx, and <1% Spl, which have a calculated average mineral formula of $(Mg_{0.78}Fe^{2+}_{0.22})(Al_{1.91}Cr_{0.06}Fe^{3+}_{0.03})O_4$. Unlike all of the other xenoliths, the spinels in this websterite have very little chromium. As in every peridotite xenolith, most of the iron in the Spl structure from the clinopyroxenite and the websterite, exists as tetrahedrally coordinated Fe^{2+}. BSE images of both pyroxenite xenoliths show alteration along grain boundaries and textural indicators of metasomatism (Figure 2.2d,e).

2.3 Analytical Methods

2.3.1 Sample preparation and purification

Minerals were separated from the five xenoliths by handpicking with the aid of a binocular microscope. The identity of each grain was confirmed by energy dispersive x-ray analysis using a scanning electron microscope prior to dissolution. Mineral separates were weighed, then powdered in an agate mortar and pestle, then dissolved in two steps. In the case of the spinel lherzolite (CEM1-3), we obtained a large enough sample to get a robust whole-rock analysis. For this sample, a split of ~10 cm^3 of rock was ground in an agate mortar and pestle until grains were approximately 5 mm in diameter, then transferred to a shatterbox and powdered to submicron grain size for ease of dissolution.

Samples were dissolved in sealed Teflon vessels jacketed in steel acid digestion bombs (Parr Instrument Co.) in a 15:18 mixture of omni-grade HF and HNO_3 at temperatures of ~230 °C (for complete spinel digestion) for at least 72 hours. Dissolved samples were transferred to high-density Teflon (Savillex™) and evaporated to dryness at 120 °C on a hotplate. Dried samples were dissolved again in aqua regia at 120 °C for at least 24 hours followed by

evaporation to dryness. Samples were then redissolved in 7N HCl in preparation for our ion exchange column chemistry procedure.

The iron was purified by anion exchange chromatography in HEPA filtered laminar flow boxes within a class 100 clean laboratory using a one-column procedure. We used pre-filled Poly-Prep® columns measuring 4 cm x 0.8 cm with 10 ml reservoirs for the two purification steps. These columns contain 0.3 ml (wet) of Bio-Rad™ AG 1-X8 analytical grade resin in 200 to 400 mesh chloride form. Columns were washed initially 3 times with 10 ml of 7N HCl alternating with ~18 MΩ cm^2/cm water and conditioned with 0.5N HCl and 7N HCl. A typical load on the column consists of between 10 and 50 μg of Fe in 300 μl of 7N HCl. Matrix elements, including Ca, Mg, Al, and Cr, are eluted by passing 9 ml of 7N HCl through the column, leaving Fe adhered to the resin. Iron is then recovered by passing 1.5 ml of 0.5N HCl through the column. The pure iron eluent is subsequently evaporated on a 120 °C hotplate until just dry, then immediately picked up in 1 ml 2% HNO_3 for mass spectrometry. Columns are used only once, then discarded.

Elution curves were determined from synthetic dissolved rock solutions containing various concentrations of Al, Mg, Ca, Fe, Cr, Mn, Mg and Ti. These rock and mineral "analogues" were made by mixing varying amount of Spex Certi-Prep standard solutions to simulate the differing proportions of each element in typical Ol, Cpx, Opx, and Spl from San Carlos xenoliths as determined by electron microprobe analyses of the xenoliths from this study. The most reliable indicator of complete recovery of Fe in the presence of matrix elements on the columns was the absence of measurable shifts in $^{56}Fe/^{54}Fe$ and $^{57}Fe/^{54}Fe$ following Fe recovery. These "zero enrichments" were checked routinely during this study. In other words, every time a batch of column chemistry was done, one or more of the columns was loaded with one of these

rock or mineral analogues instead of an actual dissolved rock or mineral in order to test the column chemistry procedure for the particular composition(s) of the rock or mineral being run that day. These "column tests" allow for a high degree of confidence as to the robustness of our column chemistry procedure.

2.3.2 Mass spectrometry

Iron isotope ratio measurements were made using a ThermoFinnigan Neptune MC-ICPMS. The instrument has a fixed array of 9 Faraday collectors each with amplifier resistors of 10^{11} Ω. Sample purity was checked by monitoring $^{23}Na^{+}$, $^{24}Mg^{+}$, $^{27}Al^{+}$, $^{44}Ca^{+}$, $^{52}Cr^{+}$, $^{55}Mn^{+}$ and $^{58}Ni^{+}$. In all cases, with the exception of Cr in some spinel samples, the abundances of these potential impurities were < 1% (atomic) of the analyte Fe concentration. Such low impurity/Fe ratios are well below thresholds for discernible matrix effects on Fe isotope ratio measurements as determined by tests using various mixtures of these elements. Tests show that even extremely small amounts of Cr will cause interferences and matrix effects, resulting in erroneously low $\delta^{57}Fe$ and $\delta^{56}Fe$ values. This problem was solved by repeating the column chemistry procedure discussed in §2.3.1 with the Fe + Cr eluents. Tests show that repeating the Fe column chemistry procedure for a single sample results in complete recovery of Fe with no measurable shifts in $^{56}Fe/^{54}Fe$ and $^{57}Fe/^{54}Fe$ following Fe recovery. Therefore, we repeated the column separation for the samples in this study.

Samples and standard were analyzed as ~1 ppm Fe in 2% HNO_3 aspirated through a Cetac Aridus® desolvating nebulizer (samples were run in dry plasma) with the addition of N_2. Mass interferences from ArO^{+} (~ 2.5 mV), $ArOH^{+}$ (< 1 mV), and ArN^{+} (~ 1.8 V) were resolved from $^{56}Fe^{+}$, $^{57}Fe^{+}$ and $^{54}Fe^{+}$, respectively, by operating at a high mass resolving power of $m/\Delta m > 10{,}000$ (Weyer and Schweiters, 2003). Corrections for instrumental mass bias were

obtained by using sample-standard bracketing with peak height matching between sample and standard to better than 5%. Samples were analyzed 8 to 10 times with each analysis consisting of 20 cycles of ~ 4 second integrations.

All values for Fe isotope ratios presented in here were obtained by comparison with the international Fe standard, IRMM-014, (Beard and Johnson, 2004) and are reported in the conventional delta notation:

$$\delta^{i}\mathrm{Fe} = 10^{3}\left(\frac{\left({}^{i}\mathrm{Fe}/{}^{54}\mathrm{Fe}\right)_{\mathrm{Sample}}}{\left({}^{i}\mathrm{Fe}/{}^{54}\mathrm{Fe}\right)_{\mathrm{IRMM\text{-}14}}} - 1\right) \quad (1)$$

where *i* refers to 56 or 57. The aliquot of IRMM-14 for this work was stored as a 20 ppm concentration of Fe in a Teflon® bottle. Uncertainties in all δ^{i}Fe values are reported at the 2 standard error level, as calculated from the successive replicate analyses, except for measurements of CEM1-3, which the averages of three different aliquots of each mineral and whole rock. Good agreement between the three separate measurements, each coming from a separate dissolution and column chemistry procedure, supports the rigorousness of our procedures.

2.4 Results

Iron isotope compositions for individual minerals and whole rocks are presented in Table 2.2 and Figure 2.3. In discussing our results we use δ^{57}Fe rather than δ^{56}Fe as is the common practice, although both are reported to allow comparison to previous work that may report δ^{56}Fe values. The mantle xenoliths have overall variations in δ^{57}Fe of -0.27 to 0.66‰, -0.03 to 0.61‰, 0.09 to 0.23‰, and 0.18 to 0.57‰ for Cpx, Opx, Ol, and Spl, respectively. In every case where

a rock contains both Ol and Spl (every sample here except the clinopyroxenite), the Spl is enriched in the heavy isotopes of iron relative to the iron in Ol. Pyroxenes do not appear to exhibit any clear systematic behavior regarding $^{57}Fe/^{54}Fe$ relative to other phases. The order of $^{57}Fe/^{54}Fe$ of constituent minerals from the spinel lherzolite (CEM1-3) is $\delta^{57}Fe_{Spl} > \delta^{57}Fe_{Cpx} > \delta^{57}Fe_{Ol} > \delta^{57}Fe_{Opx}$. For harzburgite (111-312-37) the order differs mainly due to pyroxene and is $\delta^{57}Fe_{Opx} > \delta^{57}Fe_{Spl} > \delta^{57}Fe_{Ol} > \delta^{57}Fe_{Cpx}$. For dunite (111-312-26) we obtain $\delta^{57}Fe_{Spl} > \delta^{57}Fe_{Ol} > \delta^{57}Fe_{Opx} > \delta^{57}Fe_{Cpx}$. The websterite (SC-1-70) is similar to dunite and is $\delta^{57}Fe_{Spl} > \delta^{57}Fe_{Ol} > \delta^{57}Fe_{Opx} > \delta^{57}Fe_{Cpx.}$, Lastly, The clinopyroxenite (SC-1-66) stands out from the others with $\delta^{57}Fe_{Cpx} > \delta^{57}Fe_{Opx} > \delta^{57}Fe_{Spl}$ (Table 2.2 and Figure 2.3).

The Fe isotopic compositions of whole rocks (WR) were calculated by the measured iron isotope ratios of mineral assemblages of these xenoliths with mineral modal abundance (Table 2.1). In the case of the Spl lherzolite (CEM1-3), we were also able to measure the whole rock Fe isotopic composition (0.19 ± 0.10‰) directly and compare it to the calculated value (0.22 ± 0.03‰). The agreement within uncertainties lends confidence to both our mineral Fe isotope measurements and modal estimates. The $\delta^{57}Fe$ values estimated for whole rocks range from 0.03 to 0.66‰ (Table 2.2). A comparison of whole rock $\delta^{57}Fe$ values with increasing olivine content of the rocks (Figure 2.4) reveals a negative correlation that becomes strongly linear if the Group II websterite whole rock datum is omitted. Support for this omission of websterite will be discussed in §2.6.2.

2.5 Opposing Predictions for Equilibrium Fe Isotope Fractionation Factors

In order to set up a discussion of the results presented above, we must first review the opposing predictions for equilibrium Fe isotope fractionation between mantle minerals at high temperatures. The isotopic fractionation factor (α) between two phases is expressed in terms of

the ratio of the reduced isotopic partition function ratios (β-factors). This expression can be written in the logarithmic form as

$$\ln\alpha_{A-B} = \ln\beta_A - \ln\beta_B \quad (2)$$

where $\alpha_{A\text{-}B}$ is the equilibrium fractionation factor between two substances *A* and *B,* and β_A and β_B are the β-factors of substances *A* and *B*, respectively (Urey,1947; Bigeleisen and Mayer, 1947). There are currently two different estimates for $\alpha_{A\text{-}B}$ relevant to this study: 1) ionic model estimates based on qualitative and semi-quantitative insights governing equilibrium stable isotope fractionation, and 2) predictions from modeling Mössbauer and INRXS data.

2.5.1 Ionic model predictions

Differences in vibrational frequency drive equilibrium stable isotope fractionation:

$$v = \frac{1}{2\pi}\sqrt{\frac{K_f}{\mu}} \quad (3)$$

Vibrational frequency, *v*, depends on the force constant, K_f, which is a measure of bond stiffness, and reduced mass, μ. The fractionation of iron isotopes between two phases *a* and *b* ($\alpha_{a\text{-}b}$) depends on the difference between the force constants for each vibrational mode for both phases as well as their masses (e.g., Urey, 1947; Young et al., 2002, 2009):

$$\delta^{57}\mathrm{Fe}_a - \delta^{57}\mathrm{Fe}_b \cong 10^3\ln\alpha_{a-b}^{57/54}$$

$$= \frac{10^3}{24}\left(\frac{h}{k_bT}\right)^2\left(\frac{1}{m_{54}} - \frac{1}{m_{57}}\right)\left[\sum_{j=1}^{3N_a-3}\frac{K_{f,j,a}}{4\pi^2} - \sum_{j=1}^{3N_b-3}\frac{K_{f,j,b}}{4\pi^2}\right] \quad (4)$$

where $3N_i$-3 represents all independent modes of vibration, *N* is the number of atoms in the unit cell, m_{54} and m_{57} are the atomic masses of ^{54}Fe and ^{57}Fe respectively, k_b is Boltzmann's constant, and *h* is Plank's constant. In the ionic model for inter-mineral fractionation presented by Young

et al. (2009) for Mg isotope fractionation, insights into partitioning of heavy and light isotopes between minerals were gained by treating K_f in Eq. (4) as electrostatic in origin and summing over relevant and distinct bond pairs associated with the structures and compositions of the minerals in question. With this approach we can make some predictions for Fe isotope fractionation factors between phases that have broadly similar bond types, all the while acknowledging the significant limitations inherent in such calculations relative to more quantitative *ab initio* models. A definition of mean bond strength from Pauling (1929) is required to estimate K_f, which we will need in order to use Eq. (4). Bond stiffness depends on bond strength (s_i), which according to Pauling's electrostatic valence principle is directly proportional to valence (z_i) and inversely proportional to coordination number (n_i):

$$\bar{s} = \frac{z_i}{v_i} \tag{5}$$

The force constant for a bond between cation *i* (in our case Fe) and anion *j* (e.g., O) can be written as

$$K_{f,ij} = \frac{\overline{s_i s_j} e^2 (1 - n)}{4\pi\varepsilon_o r_{ij}^3} \tag{6}$$

where ε_o is the electric constant (vacuum permittivity for simplicity), e is the charge of an electron, and n is the exponent in the Born-Mayer formulation for ion repulsion (Born and Mayer, 1932).

Eqs. (4) – (6) lead to intuitive expectations for equilibrium inter-mineral fractionation of stable isotopes that can be used to predict iron isotope fractionation amongst minerals. Eq. (4) clearly shows that the heavy isotopes of an element tend to concentrate in substances where the element will form the stiffest (shortest, strongest) bonds. Eq. (5) indicates that as coordination number decreases and/or oxidation state (charge) increases, bond stiffness increases. Therefore,

Eqs. (3) – (6) predict that the heavy isotopes of iron will concentrate in minerals where the iron coordination number is lowest and/or oxidation state is highest.

Typical San Carlos spinels in this study contain Fe^{2+} in tetrahedral (four-fold, n_i = 4) coordination with a small amount of Fe^{3+} in octahedral coordination (n_i = 6). This is characteristic of normal spinels. Olivine, Cpx, and Opx can have Fe^{2+} and Fe^{3+} in octahedral coordination only. Based solely on the coordination environment and valence state of iron in these minerals, one predicts that spinel will concentrate the heavy iron isotopes relative to olivine, diopside, and enstatite. Moreover, olivine is predicted to possess the lowest equilibrium $\delta^{57}Fe$ of all of the phases because of the combination of higher coordination than in spinel and relatively low Fe^{3+}/Fe^{2+} compared with the other phases (Cpx and Opx) with the same Fe coordination. Table 2.1 shows average compositions of minerals from San Carlos xenoliths determined by electron microprobe, which are consistent with the above summary.

Taking these rules a step further, we can use these Eqs. (3) – (6) to make semi-quantitative estimates of inter-mineral stable isotope fractionation among the mantle xenolith phases if we have good data regarding the structures and compositions of the constituent minerals. The structural formula for an average olivine in CEM1-3, the Spl lherzolite, is $(Mg_{1.81}Fe^{2+}_{0.19})^{VI}Si^{IV}O^{IV}_4$ and the average spinel has the structural formula $(Mg_{0.73}Fe^{2+}_{0.27})^{IV}(Al_{1.19}Cr_{0.74}Fe^{3+}_{0.06})^{VI}$. An average spinel from these San Carlos xenoliths has 86% of its iron as $Fe^{2+[IV]}$, and 14% as $Fe^{3+[VI]}$. From these analyses we conclude that the San Carlos spinels are "normal". This result is consistent with inversion parameters (the fraction of Al^{3+} ions occupying the tetrahedral site) ranging from ~0.1 to 1.5 for spinels from similar rocks (Uchida et al., 2005). Oxygen is coordinated by four cations in both olivine and spinel. Application of Eqs. (3) – (6) to the $Fe^{2+[VI]}$-$O^{[IV]}$ bond in olivine with $r_{Fe^{2+[VI]}-O} = 2.17\times$

$10^{-10}m$ (e.g., Gibbs et al., 2008) and the $Fe^{2+[IV]}$-$O^{[IV]}$ and $Fe^{3+[VI]}$-$O^{[IV]}$ bonds in spinel with $r_{Fe^{2+[IV]}-O} = 2.00\times10^{-10}m$, and $r_{Fe^{3+[VI]}-O} = 2.13\times10^{-10}m$, respectively, and weighting the average K_f for the Fe - O bonds by the various bond types, suggests that $\delta^{57}Fe$ for spinel should be slightly larger than that for olivine at igneous temperatures (e.g., ~0.054‰ at 1000 K). (Table 2.1).

Caution should be used when calculating specific fractionation factors at given temperatures with this model. That said, these calculations do provide a method of rationalizing structures and site occupancies in silicates and oxides, and can be used to formulate expectations for the degree (±20%) and order of isotope fractionation between phases (Young et al., 2009). The dashed lines in Figure 2.5 show the temperature dependence of $^{57}Fe/^{54}Fe$ fractionation between various minerals and olivine according to Eqs. (3) – (6). The predicted order of fractionation for the minerals in San Carlos xenoliths according to the ionic model is $\delta^{57}Fe_{Spl} > \delta^{57}Fe_{Cpx} > \delta^{57}Fe_{Opx} > \delta^{57}Fe_{Ol}$. There is no perfect agreement between the predicted order and that recorded in the San Carlos xenoliths measured in this study. However, as previously mentioned, in every rock presented here, $\delta^{57}Fe_{Spl} > \delta^{57}Fe_{Ol}$, which is in agreement with this theory. Data from the pyroxenes in these xenoliths appear erratic, following no systematic trend.

2.5.2 Mössbauer / INXRS predictions

Iron isotope fractionation between minerals can also be predicted by modeling Mössbauer and INRXS data. Using this approach, Polyakov (1997), Polyakov and Mineev (2000), and Polyakov et al. (2007) predict that spinel will concentrate the light iron isotopes relative to olivine, a trend that is opposite to the predictions from Eqs. (3) - (6). Reduced partition function ratios (β-factors) for $^{57}Fe/^{54}Fe$ can be calculated for some iron-bearing

minerals by modeling Mössbauer spectroscopic data (Polyakov, 1997; Polyakov and Mineev, 2000; Polyakov et al., 2007). In order to determine the affinity of Fe isotopes for a given phase from Mössbauer data, one must relate the equilibrium isotopic fractionation factor to the thermal shift (second-order Doppler shift) of the recoil-free Mössbauer resonant frequency. Table 2.3 shows polynomial fits to the reduced partition function ratios for various Fe-bearing mineral phases as a function of temperature where

$$10^3 \ln\beta = \mathrm{B}_1 x - \mathrm{B}_2 x^2 + \mathrm{B}_3 x^3, \qquad x = 10^6/T^2 \tag{7}$$

Combining Eq. (7) and Eq. (2) one can predict the resulting fractionation factors between some minerals and olivine as a function of temperature. These predictions are shown as the solid lines in Figure 2.5. The predicted order of fractionation for mantle minerals is $\delta^{57}Fe_{Ol} > \delta^{57}Fe_{Opx} > \delta^{57}Fe_{Cpx} > \delta^{57}Fe_{Spl}$. It is important to note that predictions of equilibrium iron isotope fractionation based on modeling Mössbauer data are opposite in sign and order of enrichment from predictions based on the ionic model discussed in §2.5.1. Also, there does not appear to be any agreement between the predictions based on modeling Mössbauer data and inter-mineral Fe isotope fractionation in the xenoliths of this study.

2.6 Discussion

2.6.1 Inter-mineral fractionation and open system processes

Disagreement between Fe isotope fractionation models is stark, and should be addressed by comparison with data from natural samples and experiments. Here I will compare our data for the inter-mineral fractionation of five San Carlos xenoliths with both models in order to get a better understanding of the systematics of iron isotope fractionation between mantle minerals. The data presented here show variation in the Fe isotope compositions of minerals in a single

xenolith and variation between individual xenoliths (whole-rock values) from San Carlos, AZ (Table 2.2 and Figure 2.3). In order to have a discussion about what these variations mean, how they arise, and if we can use these measurements to further develop Fe isotope compositions as geochemical tracers, we must first establish whether Fe isotope equilibrium has been achieved among minerals within our samples. The question of inter-mineral equilibrium in the mantle xenoliths from this study must also be answered in order to make meaningful comparisons with the opposing fractionation predictions presented in §2.5.

"δ–δ" plots of isotope compositions between minerals pairs are good indicators of isotope exchange equilibration (Gregory and Criss, 1986). Mineral pairs plotting on a line with slope of ~ 1 on a "δ–δ" plot, are in exchange equilibrium with each other. This can be seen with reference to the definition of the fractionation factor $\alpha_{1,2} = (10^3 + \delta_1)/(10^3 + \delta_2)$ for phases 1 and 2, which can be rearranged to yield $\delta_1 = (\alpha_{1,2})(\delta_2) + 10^3(\alpha_{1,2} - 1)$. It is clear also that the intercept in such a plot is a function of temperature Gregory and Criss (1986). What is more, regardless of the number of phases hosting the element of interest, data falling below the line with a zero intercept, corresponding to infinite temperature, signify open-system isotope exchange (Gregory and Criss, 1986). Figures 2.6a-f are δ^{57}Fe–δ^{57}Fe plots of every possible mineral pair present in the xenoliths measured for this study. The solid line on each plot is Y = X, and represents equilibration of the minerals at infinite $T = \infty$. The dashed lines were calculated using the ionic model for T = 500°C, the approximate closure temperature for Fe isotope exchange via diffusion (Brady, 1995). Mineral pairs plotting between the solid and dashed lines on the δ^{57}Fe–δ^{57}Fe plots are regarded as being consistent with closed-system isotope partitioning. Mineral pairs plotting above and below the region between the solid and dashed lines are regarded as having undergone some open-system isotope exchange. The mineral pairs that have undergone open

system processes do not represent equilibrium among all phases, and therefore we should not expect these mineral pairs to follow any systematic or predictable behavior in regards to degree of enrichment of $^{57}Fe/^{54}Fe$.

Figures 2.6a-d and f are plots showing $\delta^{57}Fe$ values of clinopyroxene and orthopyroxene versus spinel, olivine, and each other. In all of these δ–δ involving one or more pyroxene, there seems to be some degree of disequilibrium due to open-system processes according to the principles outlined above. This is especially true for the plots containing clinopyroxene data. We must therefore exercise caution when applying these pyroxene Fe isotope data in any way that implies equilibrium. For instance, comparing inter-mineral Fe isotope fractionation involving clinopyroxenes from these xenoliths with the equilibrium models presented in §2.5, would be futile. This position is supported by a similar study on magnesium isotopes by Young et al. (2009). These authors found that pyroxenes in two San Carlos xenoliths (one of them being CEM1-3 from this study), were out of magnesium isotopic equilibrium, and did not agree with fractionation estimates based on density functional calculations (Schauble, 2011).

Figure 2.6e, on the other hand, shows $\delta^{57}Fe_{Spl}$ versus $\delta^{57}Fe_{Ol}$ for samples CEM1-3 (lherzolite), 111-312-37 (harzburgite), 111-312-26 (dunite), and SC-1-70 (websterite). Spinels and olivines from all of these xenoliths plot within the region of closed-system processes in δ–δ space (within error). Because there is no reason to invoke open-system exchange, we have no evidence that spinel and olivine are not in isotopic equilibrium. This is the only mineral pair for which this is true. Therefore, Spl-Ol fractionation measurements (Table 2.2, Figure 2.3) are the only data that can be used to compare with the two opposing models (Figure 2.5). In all cases where spinel and olivine coexist in a sample, $\delta^{57}Fe$ of spinel is greater than $\delta^{57}Fe$ of olivine. This observation is consistent with expectations based on coordination and valence state of iron as

described in the ionic model, but inconsistent with the predictions made by modeling Mössbauer and INRXS data.

This comparison supports the use of the ionic model for qualitative (in some cases semi-quantitative) predictions of equilibrium iron isotope fractionation between oxide and silicate minerals. As mentioned earlier, my spinel samples are calculated to have only negligible amounts of Fe^{3+} in their structures, yet still result in higher $^{57}Fe/^{54}Fe$ than the coexisting olivine. This is understood as purely a coordination effect rather than an oxidation state effect. Similar influence of coordination was seen for Mg isotope portioning between spinel and olivine (Young et al., 2009). This is an important observation as it is commonly suggested that oxidation state is the primary control on Fe isotope fractionation. For example, Williams et al. (2004, 2005) described the considerable iron isotope variation in mantle spinels as reflecting mantle redox processes. Plots of $\delta^{57}Fe$ and $Fe^{3+}/\Sigma Fe$ of San Carlos spinels show no clear correlation (Figure 2.7). It seems that in the case of mantle spinels and Fe isotopes, coordination environment is the major cause of inter-mineral fractionation, with oxidation state of iron playing at most a minor role. Fe isotope data from Zhao et al. (2010) also support this hypothesis, indicating that oxygen fugacity may not be the main control on iron isotope fractionation between xenolith minerals.

2.6.2 Fe isotopes and xenolith petrogenesis

Whole-rock $\delta^{57}Fe$ values of San Carlos xenoliths range from 0.03 to 0.66‰ (Table 2.2). A comparison of increasing whole rock $\delta^{57}Fe$ values with increasing olivine content of the rocks (Figure 2.4) reveals a weakly negative correlation at first glance because the websterite datum does not follow the same apparent trend as the other rocks. In the discussion here about the origins of the differing Fe isotope compositions of these xenoliths, this anomaly provides a clue

as to the petrogenesis of these samples. As discussed earlier, Frey and Prinz (1978) recognized that San Carlos xenoliths should be divided into two petrogenetically distinct types of inclusions: Group I xenoliths, residues typically rich in Mg and Cr; and Group II xenoliths, cumulates typically rich in Fe and Ti. Also, Group I spinels have higher Cr content than Group II spinels. Another way to tell these groups apart is by comparing Al_2O_3 and Cr_2O_3 content of clinopyroxenes. Figure 2.8 shows the clinopyroxenes from the San Carlos xenoliths of this study plotted with corresponding aluminum oxide and chromium oxide weight percents. The dashed line approximately separates regions of Groups I and II xenoliths based on a modified version of Figure 12 in Frey and Prinz (1978). The websterite datum, according to these criteria, may be a Group II xenolith while all of the other rocks are clearly in the Group I area. Therefore I will treat the websterite as a Group II xenolith, which means it has a different petrogenetic history from the rest of the rocks in this study.

Having established that the websterite is a Group II inclusion, we can now discuss the rest of the xenoliths in the context of Group I petrogenesis. Group I inclusions have been widely interpreted as partial melting residues with the lherzolites considered closest to primitive mantle material capable of generating a basaltic magma (Frey and Prinz, 1978; Galer and O'Nions, 1988). Frey and Prinz (1978) noted strong trends in bulk chemical composition (major elements), mineral composition, and modal proportion in San Carlos xenoliths. They determined that major element compositional trends are not caused by varying proportions of minerals with identical major element compositions. These trends are instead the result of systematic mineral compositional changes that accompany the modal changes. The combination of these two effects together causes the variations seen in bulk chemical compositions of San Carlos inclusions.

We see similar Fe isotope compositional trends accompanying modal changes in the Group I xenoliths from this study (Figure 2.4). The dunite has the lowest $\delta^{57}Fe$ values while the clinopyroxenite has the highest. Even more tellingly, the Group I whole-rock $\delta^{57}Fe$ values show a strongly linear negative correlation with olivine content. The more abundant olivine is in a sample, the lower the $\delta^{57}Fe$ of the bulk xenolith. To first order, this observation seems to support the theory presented by Frey and Prinz (1978) that olivine-rich Group I xenoliths are the residues of partial melting episodes. The order of consumption from residue upon increasing *T* and progressive melt extraction is Cpx, then Opx, then Spl, and finally Ol (e.g., Jaques and Green, 1980; Takahashi and Kushiro, 1983; Walter and Presnall, 1994). According to the ionic model presented in §2.5.1, the order of degree of enrichment of the heavy isotopes of iron at equilibrium is Ol, then Opx, then Cpx, then Spl (i.e., at equilibrium $\delta^{57}Fe_{Ol} < \delta^{57}Fe_{Opx} < \delta^{57}Fe_{Cpx} < \delta^{57}Fe_{Spl}$). If a fertile lherzolite representing upper mantle Fe isotope compositions is partially melted, the resulting residues will contain less Cpx and Opx (having migrated away in the melt), and will therefore be isotopically depleted due to the preferential loss of those phases that concentrate the heavy iron isotopes. However, this behavior alone cannot account for the range of whole rock Fe isotope compositions seen in our olivine-rich Group I samples (lherzolite, harzburgite, and dunite). The fractionation between olivine and pyroxenes is too small to produce the observed variation in whole rock $\delta^{57}Fe$ values.

Several recent studies have pointed to redox-controlled iron isotope fractionation during melting as the process responsible for observed whole rock $^{57}Fe/^{54}Fe$ variations (e.g. Williams et al., 2005; Dauphas et al., 2009). These studies explored the possibility that equilibrium fractionation between Fe^{2+} and Fe^{3+} during mantle melting could be the primary control on the iron isotopic variations among mantle xenoliths. Fe^{3+} is approximately ten times more

incompatible than Fe^{2+} during mantle melting (Canil et al., 1994; Woodland et al., 2006). The effective coordination of Fe^{2+} and Fe^{3+} is about 5 on average in basaltic melts (e.g., Jackson et al., 2005; Wilke et al., 2005), but 6 in Cpx, Opx, and Ol. Therefore, pursuing a redox-controlled fractionation mechanism makes sense. Dauphas et al. (2009) introduced a quantitative model relating the iron isotopic composition of magmas to the degree of partial melting, Fe^{2+} and Fe^{3+} concentration, and buffering capacity of the mantle. This model produces partial melting evolution curves for $\delta^{56}Fe$ by assuming equilibrium isotope fractionation between Fe^{2+} and Fe^{3+} with preferential extraction of Fe^{3+} during melting.

The solid and dashed lines on Figure 2.4 respectively represent evolution of a solid residue and extracted melt, calculated using equations for buffered fractional melting from Dauphas et al. (2009) Appendix B. I modified the model by using bulk Fe^{2+}/Fe^{3+} and $\delta^{57}Fe$ values of CEM1-3 (our Spl lherzolite) as the fertile source rock (initial composition of the residue). Also, in order to plot the curves on Figure 2.4, I had to convert the x-axis from degree of partial melting (%), to % olivine. This was achieved by interpolating data from melting experiments of Kinzler et al. (1997) relating mineral mode in a partial melting residue to the degree of partial melting. The resulting plot (Figure 2.4) suggests that the iron isotope values of the lherzolite, harzburgite, and dunite of this study could be caused by redox-controlled partial melting. Contributions from the differences between coordination environments of Fe in silicates (6) and melt (~5) are not represented in calculations here, but would serve to enhance the degree of fractionation to some extent.

The relatively high $\delta^{57}Fe$ value of the clinopyroxenite compared with the other Group I xenoliths is also explainable using the redox-controlled fractional melting model (Dauphas et al., 2009). It would require that the clinopyroxenite be a cumulate crystallized from a melt extracted

at ~65% partial melting (assuming the mantle source composition of CEM1-3). Frey and Prinz (1978) suggested that the common association of pyroxenite layers with lherzolites at San Carlos could be the result of cumulate processes involving physical separation of a solid from its coexisting equilibrium liquid, such as precipitation along the edges of a feeder dike. However, alternate explanations involving metasomatism of pyroxene should also be explored because partial melting does not explain the erratic nature of the inter-mineral Fe isotope fractionation values seen in San Carlos xenoliths, especially the seemingly anomalous clinopyroxene data.

2.6.3 Metasomatic alteration affecting Fe isotope compositions

The inter-mineral Fe isotope fractionation between pyroxenes and other mantle minerals in these xenoliths do not appear to reflect equilibrium processes, while the fractionation between spinel and olivine do seem to be in equilibrium (Figure 2.6). Therefore, the variation in individual mineral δ^{57}Fe values in these samples cannot be explained by partial melting alone. Late stage alteration mechanisms such as metasomatism and reaction with migrating melts are obvious alternative lithospheric mantle processes capable of producing the heterogeneity seen in our data. It is well established that localized metasomatic events and reactions with proximal magmatic dykes have altered major and minor oxides as well as isotopic compositions of San Carlos inclusions (Frey and Prinz, 1978; Galer and O'Nions, 1988). Frey and Prinz (1978) determined that San Carlos Group I inclusions formed as partial melting residues and were later penetrated by a migratory fluid phase in some localized regions.

The first non-traditional stable isotope evidence for late stage alteration of San Carlos pyroxenes by a fluid phase comes from Jeffcoate et al. (2007) who found Li isotopic disequilibrium in pyroxenes (especially Cpx) from San Carlos inclusions. They attributed these

observations to exchange with young interstitial melts. More recently, Young et al. (2009) clearly demonstrated that San Carlos pyroxenes have been shifted out of equilibrium according to magnesium isotopes. Young's group measured the Mg isotope compositions of minerals and whole-rocks for two San Carlos xenoliths, a spinel lherzolite (the same sample measured here for Fe isotopes) and a spinel harzburgite. In both rocks, the δ^{26}Mg values indicated that pyroxenes were out of equilibrium with spinel and olivine according to both density functional calculations (Schauble, 2011), and Mg isotope thermometry. Young et al. (2009) reasoned that this disequilibrium was caused by metasomatism or late stage exchange with a proximal melt.

Several lines of evidence indicate that pyroxenes are more easily altered than olivine and spinel at mantle conditions. Clinopyroxene and orthopyroxene are less refractory than olivine and spinel during mantle melting according to thermodynamic calculations and experiments (e.g. Takahashi and Kushiro, 1983; Walter and Presnall, 1998). Gudfinnsson and Presnall (2000) found that Fe-Mg exchange coefficients ($K_{\text{d Fe-Mg}}^{\text{xl-liq}}$) for olivine and spinel are almost independent of temperature and pressure, whereas the coefficients for the pyroxenes increase with temperature and pressure with clinopyroxene showing the most variation. Solubility experiments done at upper mantle *P-T* conditions also find pyroxenes are more soluble in high *P-T* solutions than olivine (e.g., Macris et al., 2006; Newton and Manning, 2006; Wykes et al., 2011). It makes sense, therefore, that clinopyroxene and orthopyroxene (to a lesser degree) are the minerals most modified in the lithospheric mantle in terms of major oxides and isotopic compositions, and that the mechanism of alteration is contact with a metasomatic fluid.

2.7 Conclusions

This study allows me to draw the following primary conclusions:

1. The data presented in this study are consistent with the Fe isotope data of mantle xenoliths reported in previous studies in that they all show Fe isotope variations between minerals within a single sample and between mantle xenoliths, suggesting a heterogeneous Fe isotope composition for the lithospheric mantle.
2. δ–δ plots of San Carlos inclusion minerals suggest that spinel and olivine are in equilibrium with each other, but pyroxenes are out of equilibrium with both olivine and spinel, and with each other.
3. Comparisons of Fe isotope fractionations between spinel and olivine in individual San Carlos xenoliths agrees generally with the sign and order of Fe equilibrium inter-mineral fractionation predicted by an ionic model, but disagree with the sign and order of fractionation predicted by modeling Mössbauer data.
4. Redox-controlled mineral-melt iron isotopic fractionation during partial melting of the mantle is likely the main cause of variations observed in whole rock δ^{57}Fe values of olivine-rich Group I xenoliths.
5. Disequilibrium involving pyroxenes can be attributed to late stage metasomatism or interaction with a migrating melt.
6. Coordination environment the major role in equilibrium inter-mineral iron isotope fractionation in the mantle. However, oxidation state is likely the controlling factor that determines mineral-melt equilibrium iron isotope fractionation.
7. Fe-isotope compositions of mantle minerals and bulk xenoliths are powerful tracers of high temperature geological processes if care is taken when selecting samples and interpreting data.

8. Experiments must be done in order to confirm or refute existing models of temperature dependence of Fe equilibrium fractionation in mantle minerals.

Table 2.1 Major oxides (wt.%), mode (% mineral), and chromium number of minerals in peridotite and pyroxenite xenoliths from San Carlos, AZ.

Sample	CEM1-3				111.312.37				111-312-26				SC-1-70				SC-1-66			
Rock	Spinel lherzolite				Harzburgite				Dunite				Websterite				Clinopyroxenite			
Mineral	Ol	Opx	Cpx	Spl	Ol	Opx	Cpx	Spl	Ol	Opx	Cpx	Spl	Ol	Opx	Cpx	Spl	Ol	Opx	Cpx	Spl
Points	66	12	14	10	11	6	11	8	9	9	11	11	11	11	11	2	0	11	11	11
SiO_2	40.25	55.07	52.07	0.02	41.01	56.12	53.14	0.03	40.98	54.76	48.57	0.04	40.16	53.81	51.00	0.05		54.99	51.73	0.04
TiO_2	0.01	0.05	0.13	0.12	0.01	0.03	0.08	0.18	0.02	0.08	2.09	0.14	0.00	0.09	0.45	0.10		0.16	0.51	0.36
Al_2O_3	0.01	2.91	4.26	35.28	0.01	2.47	2.89	30.54	0.03	4.67	5.82	48.23	0.04	6.05	7.71	65.28		3.99	5.26	44.50
Cr_2O_3	0.02	0.58	1.30	32.64	0.02	0.62	1.11	39.46	0.02	0.65	0.43	19.26	0.03	0.15	0.28	2.91		0.55	1.19	22.96
Fe_2O_3	0.38	0.21	1.74	3.02	0.53	0.84	0.39	2.38	0.28	0.52	2.22	2.00	1.07	0.82	1.15	1.38		0.51	0.19	1.50
FeO	8.71	5.53	1.12	11.37	8.14	4.60	2.07	11.51	8.56	5.01	3.97	9.33	11.54	6.96	3.83	10.43		6.46	2.93	12.49
MnO	0.13	0.14	0.08	0.24	0.13	0.12	0.10	0.24	0.13	0.11	0.14	0.16	0.17	0.16	0.12	0.12		0.15	0.10	0.19
MgO	48.94	32.86	16.04	17.01	50.49	34.25	17.66	16.77	49.99	32.88	14.04	19.55	47.53	31.15	15.47	21.18		32.47	16.25	17.37
CaO	0.07	0.80	19.89		0.07	0.93	21.38		0.10	1.05	21.75		0.10	1.01	19.60			0.91	20.62	
Na_2O		0.11	1.53			0.03	0.56			0.10	0.64			0.10	1.23			0.05	0.82	
Total	98.5	98.3	98.2	99.7	100.4	100.0	99.4	101.1	100.1	99.8	99.7	98.7	100.6	100.3	99.8	101.5		100.2	99.6	99.4
Modal %	64	24	12	<1	69	27	4	<1	93	2	5	<1	32	58	10	<1	0	5	95	<1
Cr#		11.85	16.99	38.30		14.33	20.42	46.43		8.56	4.57	21.13		1.60	2.39	2.90		8.48	13.13	25.71

Abbreviations: Ol, olivine; Opx, orthopyroxene; Cpx, clinopyroxene; Spl, spinel.

$Cr\# = 100 \times Cr^{3+}/(Cr^{3+}+Al^{3+})$.

Table 2.2
Iron isotopic compositions of silicate minerals and spinels from peridotite and pyroxenite xenoliths from San Carlos, AZ.

Sample	Rock Type	Mineral	$\delta^{57}Fe$	2 SE	$\delta^{56}Fe$	2 SE
CEM1-3	Spl Lherzolite	Cpx	0.24	0.03	0.15	0.02
		Opx	0.20	0.03	0.12	0.02
		Olivine	0.23	0.04	0.15	0.04
		Spinel	0.44	0.04	0.29	0.02
		Whole-Rock*	0.22	0.03	0.05	0.02
		Whole-Rock**	0.19	0.10	0.11	0.08
111-312-37	Harzburgite	Cpx	0.10	0.03	0.04	0.02
		Opx	0.24	0.04	0.17	0.01
		Olivine	0.14	0.04	0.10	0.02
		Spinel	0.18	0.03	0.01	0.02
		Whole-Rock*	0.16	0.03	0.05	0.01
111-312-26	Dunite	Cpx	-0.10	0.03	-0.14	0.01
		Opx	0.03	0.03	-0.01	0.02
		Olivine	0.09	0.03	0.04	0.01
		Spinel	0.22	0.04	0.11	0.03
		Whole-Rock*	0.07	0.03	-0.01	0.02
SC-1-70	Websterite	Cpx	-0.27	0.04	-0.27	0.03
		Opx	0.04	0.03	0.00	0.02
		Olivine	0.06	0.03	0.26	0.03
		Spinel	0.21	0.05	0.11	0.04
		Whole-Rock*	0.03	0.02	-0.01	0.02
SC-1-66	Clinopyroxenite	Cpx	0.66	0.04	0.46	0.03
		Opx	0.61	0.05	0.41	0.02
		Spinel	0.57	0.03	0.36	0.03
		Whole-Rock*	0.66	0.04	0.46	0.03

*Whole-rock Fe isotopic compositions calculated based on mineral data.
**Whole-rock Fe isotopic compositions measured directly.

Table 2.3 Coefficients for calculating $^{57}Fe/^{54}Fe$ fractionation between phase *i* and olivine, $10^3 \ln\beta = B_1 x - B_2 x^2 + B_3 x^3$, $\mathbf{x} = 10^6/T^2$

^{57}Fe-^{54}Fe	B1	B2	B3
Spl ($Mg_{0.9}Fe_{0.1}Al_2O_4$)	0.456316	0.000628	1.34434E-06
Chr ($FeCr_2O_4$)	0.429868	0.000557	1.12388E-06
Opx1 ($Mg_{1.95}Fe_{0.05}Al_{0.05}Si_{1.96}O_6$)			
A Site	0.497467	0.000746	1.74183E-06
B Site	0.497467	0.000746	1.74183E-06
Opx2 ($Mg_{1.65}Fe_{0.27}Al_{0.03}Si_{2.02}O_6$)			
A Site	0.429868	0.000557	1.12388E-06
B Site	0.663553	0.001328	4.13369E-06
Cpx ($Ca_{1.03}Mg_{0.64}Fe_{0.31}Si_{1.94}O_6$)			
A Site	1.17247	0.004146	2.28041E-05
B Site	0.483553	0.000705	1.59972E-06
Mgt (Fe_3O_4)	0.95706	0.004730	4.07030E-06
Ol $(Mg,Fe)_2SiO_4$	0.57000	0.000986	2.62021E-06

Coefficients for Magnetite are from Polyakov et al. (2007). All other coefficients are from Polyakov and Mineev (2000). *Spl* spinel; *Chr* chromite; *Opx* orthopyroxene; *Cpx* clinopyroxene; *Mgt* magnetite; *Ol* olivine.

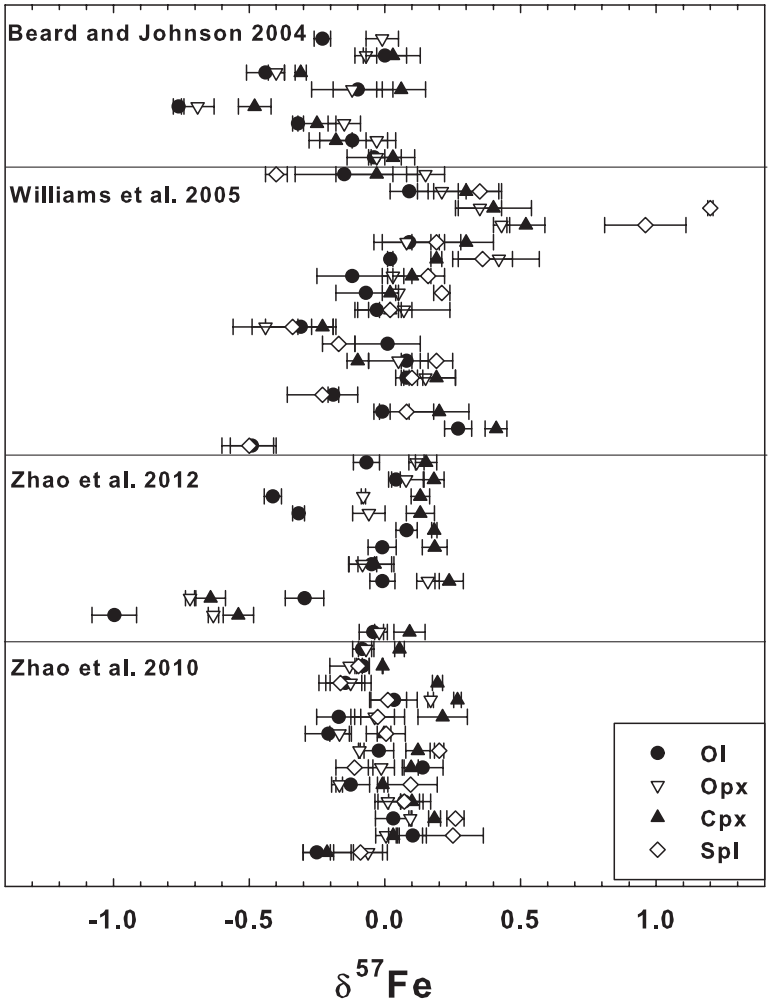

Figure 2.1 Fe isotope compositions of mantle minerals. Constituent minerals from a single xenolith are show collinearly so that inter-mineral fractionation can be discerned. Data from Beard and Johnson (2004); Williams et al. (2005); and Zhao et al. (2010, 2012). *Ol* olivine; *Opx* orthopyroxene; *Cpx* clinopyroxene; *Spl* spinel. Error bars represent 2 standard deviations.

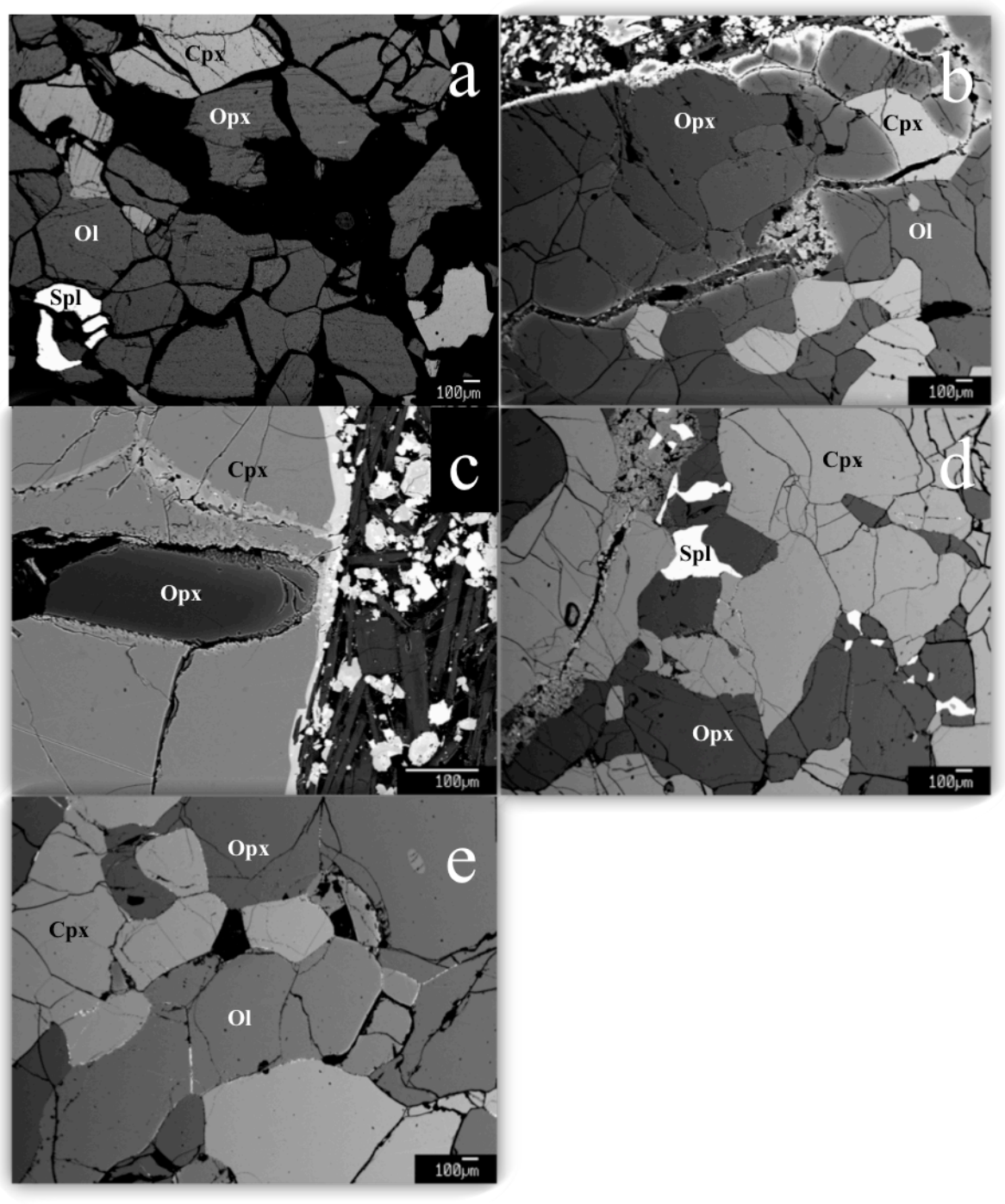

Figure 2.2 Backscattered electron images of San Carlos xenoliths from this study. (a) Spl lherzolite (CEM1-3), (b) harzburgite (111-312-26), (c) dunite (111-312-37), (d) clinopyroxenite (SC-1-66), and (e) websterite (SC-1-70).

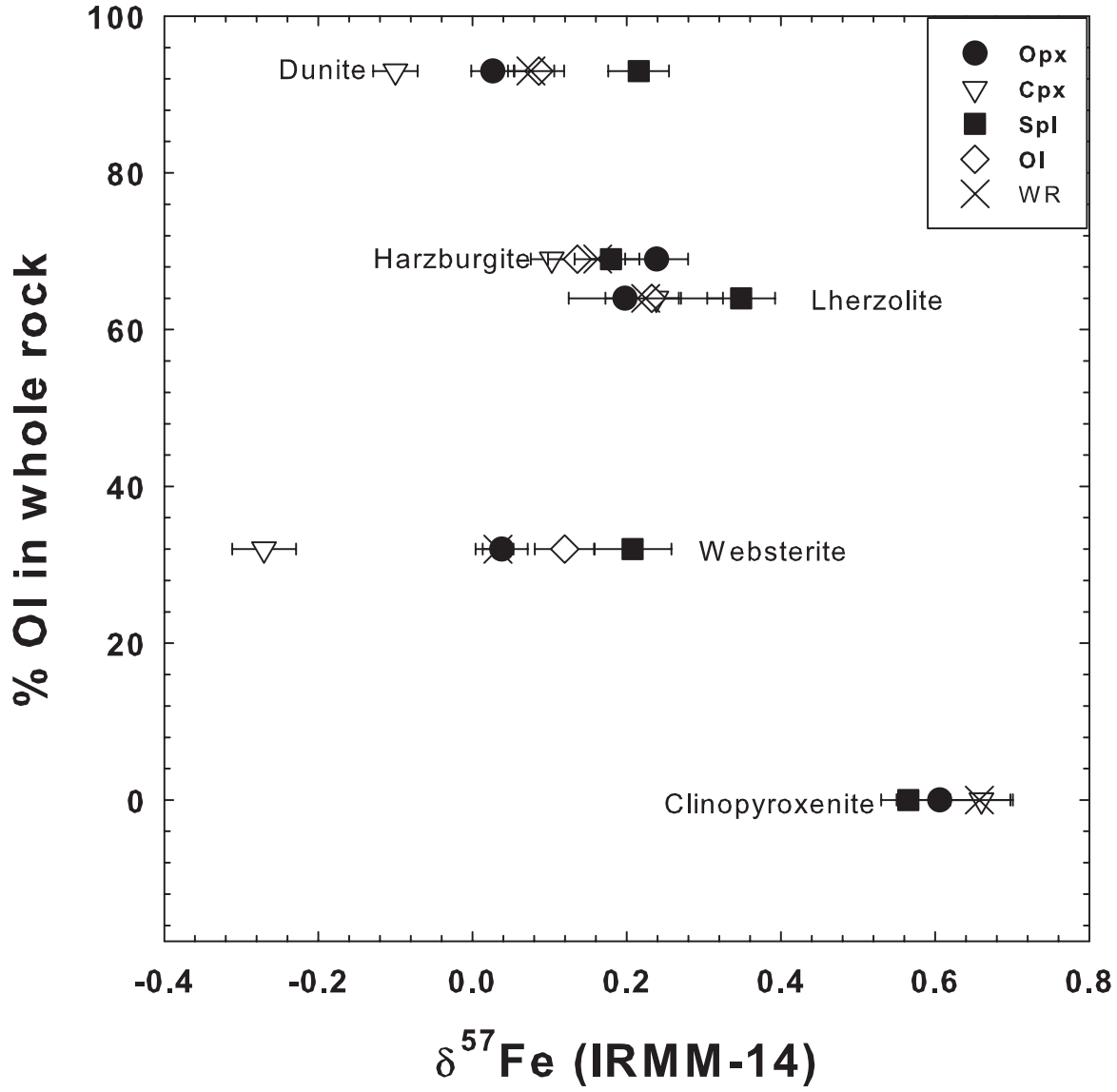

Figure 2.3 δ^{57}Fe values of olivine (Ol), orthopyroxene (Opx), clinopyroxene (Cpx), spinel (Spl), and whole rock (WR) versus percent olivine in the corresponding xenoliths; data from Tables 2.1 and 2.2.

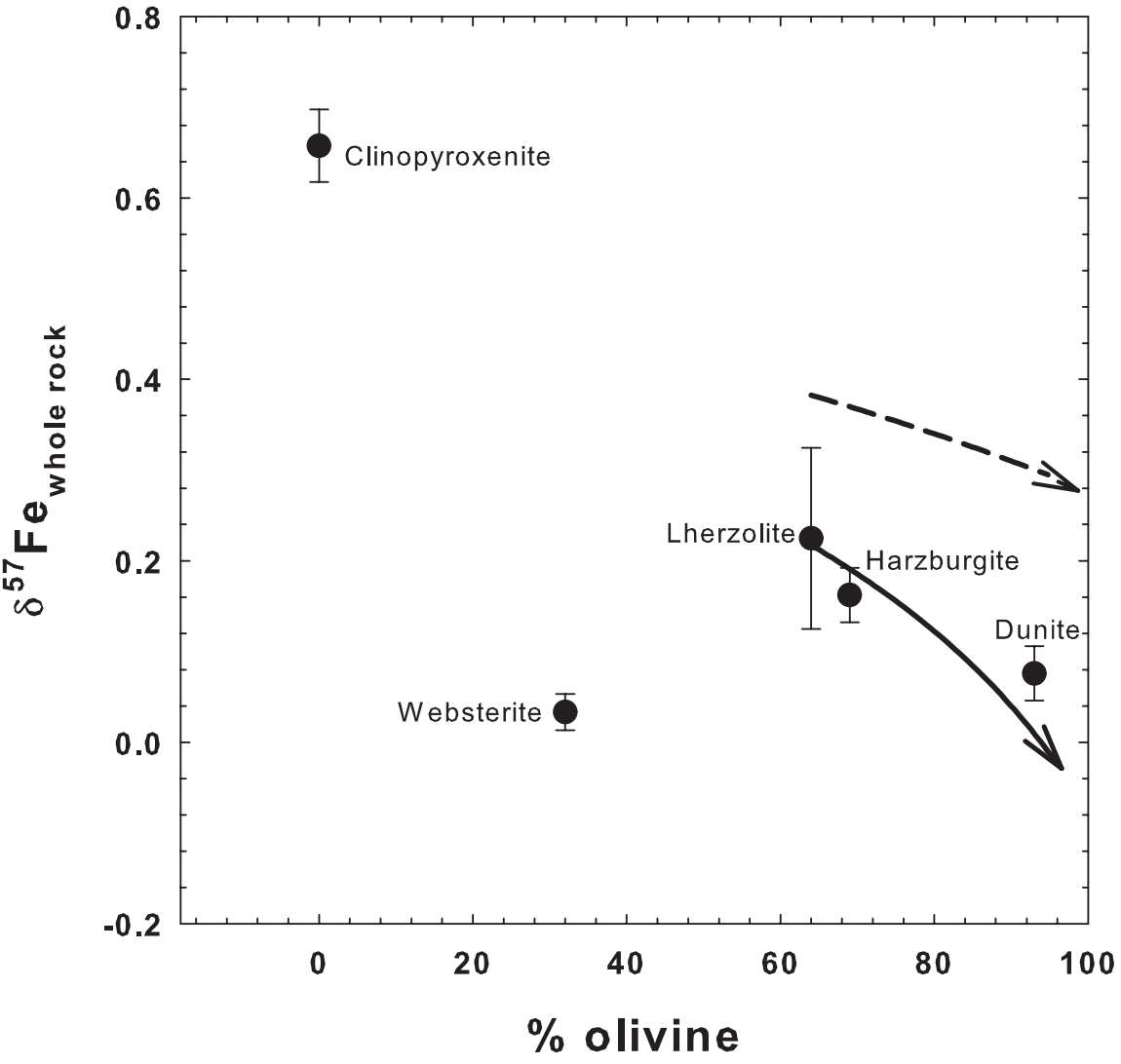

Figure 2.4 Whole-rock δ^{57}Fe values versus percent olivine in the corresponding xenoliths; data from Tables 2.1 and 2.2. The solid line (solid residue) and dashed line (melt) are partial melting curves modified from Dauphas et al. (2009). See main text for details. Error bars on all data points (except for the lherzolite) depict 2 standard error and are calculated by regressing the errors of constituent mineral δ^{57}Fe values. Error bars on the lherzolite represent 2 standard error as determined by direct measurement of the powdered rock by MC-ICPMS.

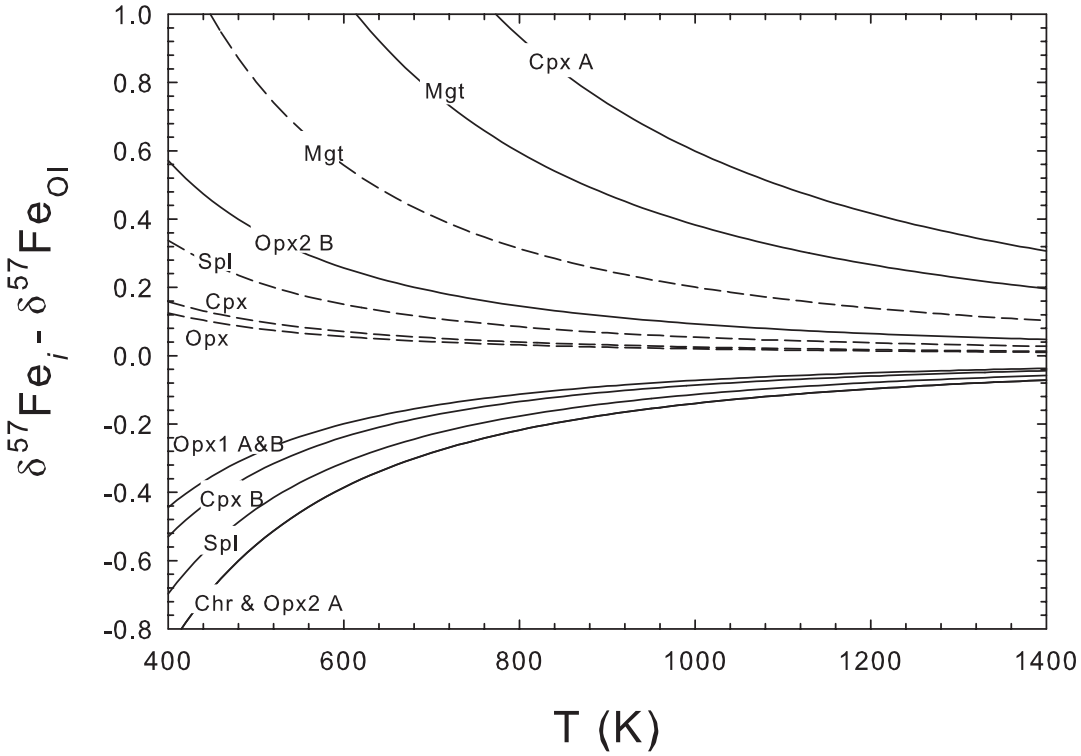

Figure 2.5 Plot showing the calculated temperature dependence of δ^{57}Fe of magnetite (Mgt), enstatite (Opx on figure), diopside (Cpx on figure), spinel (Spl), and chromite (Chr) relative to forsterite (Ol on figure). Dashed curves are predictions based on the ionic model (§2.5.1). Solid curves are predictions based on modeling Mössbauer data (§2.5.2), and were calculated from the coefficients in Table 2.3 (Polyakov and Mineev, 2000; Polyakov et al., 2007).

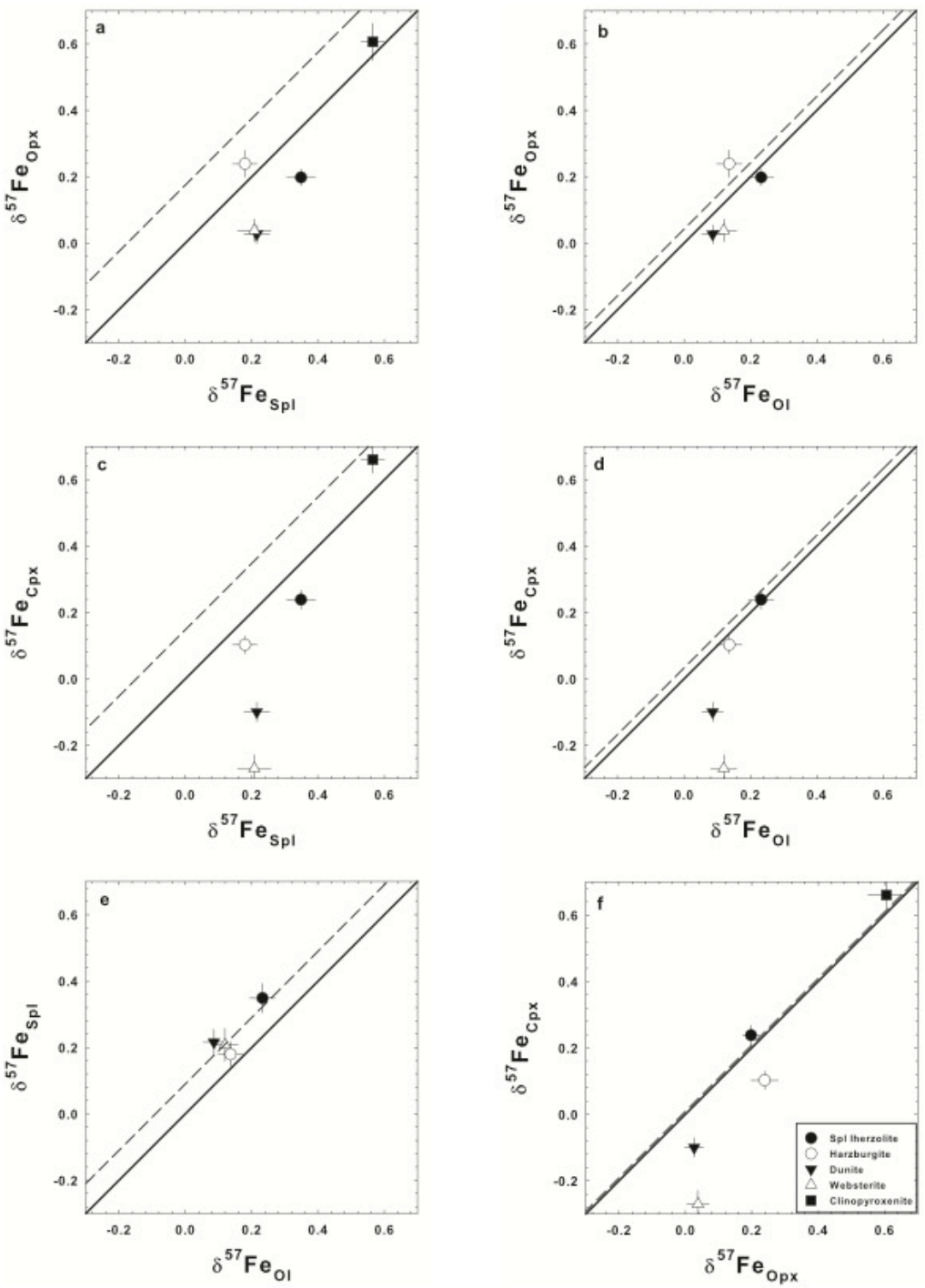

Figure 2.6 Fe isotope fractionation between minerals in San Carlos mantle xenoliths. The solid lines represent $T = \infty$. The dashed lines represent $T = 773.15$ K, and were determined using the ionic model discussed in §2.5.1. See text for further explanation. Error bars on individual data points depict 2 standard error for each measurement.

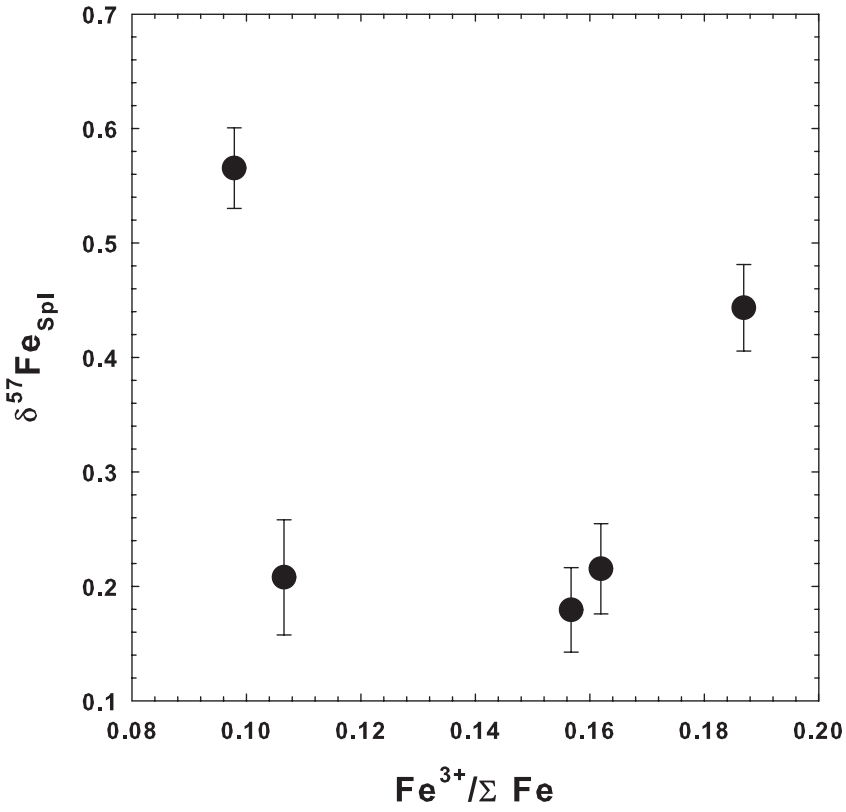

Figure 2.7 Spinel δ^{57}Fe values versus oxidation state of iron in San Carlos xenoliths. Data from Tables 2.1 and 2.2. Error bars are 2 standard error.

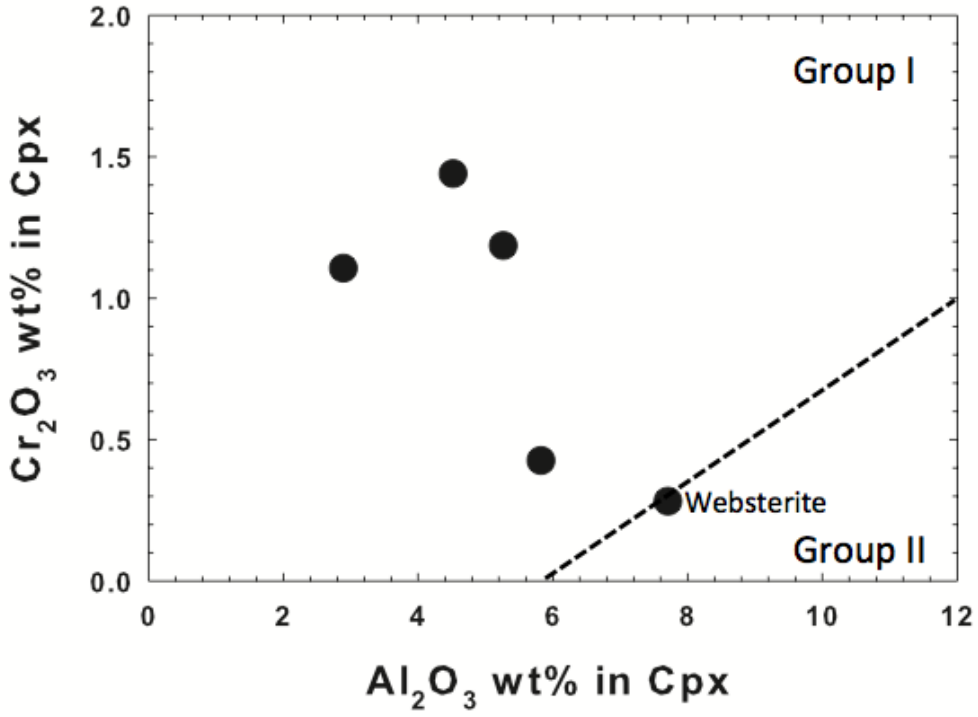

Figure 2.8 Chromium oxide versus aluminum oxide content of clinopyroxenes from San Carlos xenoliths. The dashed line indicates separation between Groups I and II xenoliths (modified from Frey and Prinz, 1978). Data are from Table 2.1.

References

Beard B. L. and Johnson C.M. (2004) Inter-mineral Fe isotope variations in mantle-derived rocks and implications for the Fe geochemical cycle. *Geochimica et Cosmochimica Acta* **68**, 4727-4743.

Bigeleisen J. and Mayer M. G. (1947) Calculation of equilibrium constants for isotopic exchange reactions. *Journal of Chemical Physics* **15**, 261–267.

Born M. and Mayer J. E. (1932) Zur Gittertheorie der Ionenkristalle. *Zeitschrift für Physik A Hadrons and Nuclei* **75**, 1-18.

Canil D., O'Neill H., St C., Pearson D. G., Rudnick R. L., McDonough W. F., and Carswell D. A. (1994) Ferric iron in peridotites and mantle oxidation states. *Earth and Planetary Science Letters* **123**, 205-220.

Dauphas N., Craddock P. R., Asimow P. D., Bennett V. C., Nutman A. P., and Ohnenstetter D. (2009) Iron isotopes may reveal the redox conditions of mantle melting from Archean to Present. *Earth and Planetary Science Letters* **288**, 255-267.

Frey F. A. and Prinz M. (1978) Ultramafic inclusions from San Carlos, Arizona: Petrologic and geochemical data bearing on their petrogenesis. *Earth and Planetary Science Letters* **38**,129-176.

Galer S. J. G. and O'Nions R. K. (1988) Chemical and isotopic studies of ultramafic inclusions from the San Carlos Volcanic Field, Arizona: A bearing on their petrogenesis. *Journal of Petrology* **30**, 1033-1064.

Gregory and Criss (1986) Isotopic Exchange in Open and Closed Systems. *Reviews in Mineralogy and Geochemistry* **16**, 91 – 128.

Gudfinnsson G. H. and Presnall D. C. (2000) Melting Behaviour of Model Lherzolite in the System CaO–MgO–Al_2O_3–SiO_2–FeO at 0.7–2.8 GPa. *Journal of Petrology* **41**, 1241-1269.

Huang F., Zhang Z., Lundstrom C. C., and Zhi X. (2011) Iron and magnesium isotopic compositions of peridotite xenoliths from Eastern China. *Geochimica et Cosmochimica Acta* **75**, 3318-3334.

Jaques A. L. and Green D. H. (1980) Anhydrous melting of peridotite at 0–15 kb pressure and the genesis of tholeiitic basalts. *Contributions to Mineralogy and Petrology*, **73**, 287-310.

Jeffcoate A. B., Elliott T., Kasemann S. A., Ionov D., Cooper K., and Brooker R. (2007) Li isotope fractionation in peridotites and mafic melts. *Geochimica et Cosmochimica Acta* **71**, 202-218.

Johannsen A. (1931) A Descriptive Petrography of the Igneous Rocks. Vol. 1. Chicago University Press, Chicago. 267 pp.

Kinzler R. J. (1997). Melting of mantle peridotite at pressures approaching the spinel to garnet transition: Application to mid-ocean ridge basalt petrogenesis. *Journal of Geophysical Research* **102**, 853-874.

Macris C. A. and Manning C. E. (2006, December). The solubility of diopside in H_2O-NaCl fluids at 800 C and 10 kbar. In *AGU Fall Meeting Abstracts* (Vol. 1, p. 1091).

Newton R. C. and Manning C. E. (2006) Solubilities of corundum, wollastonite and quartz in H_2O–NaCl solutions at 800° C and 10kbar: Interaction of simple minerals with brines at high pressure and temperature. *Geochimica et Cosmochimica Acta* **70**, 5571-5582.

Pauling L. (1929) The principles determining the structure of complex ionic crystals.

Journal of the American Chemical Society **51**, 1010-1026.

Pauling, L. (1960) The Nature of the Chemical Bond. Cornell University Press.

Poitrasson F., Halliday A. N., Lee D. C., Levasseur S., and Teutsch N. (2004) Significance of iron isotope mineral fractionation in pallasites and iron meteorites for the core-mantle differentiation of terrestrial planets. *Earth and Planetary Science Letters* **223**, 253-266.

Polyakov V. B. (1997) Equilibrium fractionation of the iron isotopes: Estimation from Mossbauer spectroscopy data. *Geochimica et Cosmochimica Acta* **61**, 4213-4217.

Polyakov V. B. and Mineev S. D. (2000) The use of Mössbauer spectroscopy in stable isotope geochemistry. *Geochimica et Cosmochimica Acta* **64**, 849-865.

Polyakov V. B., Clayton R. N., Horita J., and Mineev S. D. (2007) Equilibrium iron isotope fractionation factors of minerals: reevaluation from the data of nuclear inelastic resonant X-ray scattering and Mössbauer spectroscopy. *Geochimica et Cosmochimica Acta* **71**, 3833-3846.

Schauble E. A. (2004) Applying stable isotope fractionation theory to new systems. *Reviews in Mineralogy and Geochemistry* **55**, 65-111.

Schoenberg R. and von Blanckenburg F. (2006) Modes of planetary-scale Fe isotope fractionation. *Earth and Planetary Science Letters* **252**, 342-359.

Takahashi E. and Kushiro I. (1983) Melting of a dry peridotite at high pressures and basalt magma genesis. *American Mineralogist* **68**, 859-879.

Urey H.C. (1947) The thermodynamic properties of isotopic substances. *Journal of the Chemical Society,* 562-581.

Walter M. J. and Presnall D. C. (1994) Melting behavior of simplified lherzolite in the system CaO-MgO-Al_2O_3-SiO_2-Na_2O from 7 to 35 kbar. *Journal of Petrology* **35**, 329-359.

Weyer S., Anbar A. D., Brey G. P., Munker C., Mezger K., and Woodland A. B. (2005) Iron isotopic fractionation during planetary differentiation. *Earth and Planetary Science Letters* **240**, 251-264.

Weyer S. and Ionov D. A. (2007) Partial melting and melt percolation in the mantle: the message from Fe isotopics. *Earth and Planetary Science Letters* **259**, 119-133.

Weyer S. and Schwieters J. B. (2003) High precision Fe isotope measurements with high mass resolution MC-ICPMS. *International Journal of Mass Spectrometry* **226**, 355-368.

Williams H. M., McCammon C. A., Peslier A. H., Halliday A. N., Teutsch N., Levasseur S., and Burg J.-P. (2004) Iron isotope fractionation and the oxygen fugacity of the mantle. *Science* **304**, 1656-1659.

Williams H. M., Pelsier A. H., McCammon C., Halliday A. N., Levasseur S., Teutsch N., and Burg J.–P. (2005) Systematic iron isotope variations in mantle rocks and minerals: The effects of partial melting and oxygen fugacity. *Earth and Planetary Science Letters* **235**, 435-452.

Williams H. M., Nielsen S. G., Renac C., Griffin W. L., O'Reilly S. Y., McCammon C. A., Pearson N., Viljoen F., Alt J. C., and Halliday A. N. (2009) Fractionation of oxygen and iron isotopes by partial melting processes: Implications for the interpretation of stable isotope signatures in mafic rocks. *Earth and Planetary Science Letters* **283**, 155-166.

Woodland A. B., Kornprobst J., and Tabit A. (2006) Ferric iron in orogenic lherzolite massifs and controls of oxygen fugacity in the upper mantle. *Lithos* **89**, 222-241.

Wykes J. L., Newton R. C., and Manning C. E. (2011, December) Forsterite solubility in NaCl-H2O fluids at upper mantle PT conditions. In *AGU Fall Meeting Abstracts*

(Vol. 1, p. 0059).

Young E. D., Galy A., Nagahara H. (2002) Kinetic and equilibrium mass-dependent isotope fractionation laws in nature and their geochemical and cosmochemical significance. *Geochimica et Cosmochimica Acta* **66**, 1095-1104.

Young E. D., Tonui E., Manning C. E., Schauble E., and Macris C. A. (2009) Spinel–olivine magnesium isotope thermometry in the mantle and implications for the Mg isotopic composition of Earth. *Earth and Planetary Science Letters* **288**, 524-533.

Zhao X., Zhang H., Zhu X., Tang S., and Tang Y. (2010) Iron isotope variations in spinel peridotite xenoliths from North China Craton: implications for mantle metasomatism. *Contributions to Mineralogy and Petrology* **160**, 1-14.

Zhao X., Zhang H., Zhu X., Tang S., and Yan B. (2012) Iron isotope evidence for multistage melt-peridotite interactions in the lithospheric mantle of eastern China. *Chemical Geology* **292-293**, 127-139.

Zhu X. K., Guo Y., Williams R. J. P., O'Nions R. K., Matthews A., Belshaw N. S., Canters G. W., de Waal E. C., Weser U., Burgess B. K., and Salvato B. (2002) Mass fractionation processes of transition metal isotopics. *Earth and Planetary Science Letters* **200**, 47-62.

CHAPTER THREE

Experimental determination of equilibrium magnesium isotope fractionation between spinel, forsterite, and magnesite from 600°C to 800°C

Abstract

Magnesium isotopes are potentially powerful tools for high-temperature geochemistry if relevant fractionation factors are known. However, experimental data for Mg isotope fractionation are lacking at high temperatures. I performed piston-cylinder experiments at 600, 700, and 800 °C at 1 GPa to establish the equilibrium magnesium isotope partitioning between forsterite (Mg_2SiO_4) and magnesite ($MgCO_3$) and between spinel ($MgAl_2O_4$) and magnesite, making use of the well-established advantages of using carbonates as an isotope exchange medium (e.g. Clayton et al., 1989). In these experiments I implemented the three-isotope method with forsterite and magnesite, and with spinel and magnesite, at three different temperatures in high-pressure piston cylinder apparatus for varying lengths of time. The present study extends the applicability of the three-isotope method at high temperatures to experiments involving simple isotope exchange rather than exchange by heterogeneous reaction (e.g., Shahar et al., 2008). I used magnesite as the exchange medium (and exchange partner) to overcome the sluggish diffusion-limited exchange between spinel and forsterite alone. The carbonate medium evidently facilitates chemical and isotopic exchange by promoting annealing and re-crystallization of minerals during the experiment. Results are as follows: $\Delta^{26}Mg_{Fo\text{-}Mgs}$ = 0.036 ± 0.043‰ at 800 °C, 0.107 ± 0.095‰ at 700 °C, and 0.438 ± 0.098‰ at 600 °C; and $\Delta^{26}Mg_{Sp\text{-}Mgs}$ = 0.896 ± 0.285‰ at 800 °C, 1.098 ± 0.273‰ at 700 °C, and 1.727 ± 0.376‰ at 600 °C.

From these experimentally determined equilibrium fractionation values, I derive the temperature-dependent equilibrium fractionation between spinel and forsterite by difference, yielding $\Delta^{26}Mg_{Sp\text{-}Fo}$ values of 0.860 ± 0.288‰ at 800 °C, 0.992 ± 0.289‰ at 700 °C, and 1.289 ± 0.388‰ at 600 °C. These results agree remarkably well with first- principles estimates of equilibrium magnesium isotope fractionation between spinel and forsterite at high temperatures (Schauble, 2011). These findings are also consistent with spinel-forsterite fractionation measured in mantle xenoliths after correction for temperature (Young et al., 2009). The data allow the calculation of an experimentally determined equation for the temperature dependence of $^{26}Mg/^{24}Mg$ fractionation between spinel and olivine: $\Delta^{26}Mg_{Spl\text{-}Fo} = 0.96\ (\pm 0.21) \times 10^6/T^2$. This result is the first rigorous high-T experimental calibration of Mg isotope fractionation of mantle minerals, and is generally consistent with expectations based on crystal chemical environment of Mg in these phases.

3.1 Introduction

The use of non-traditional stable isotope partitioning between minerals is rapidly growing as a tool in geochemistry because investigators now have the capability to analyze the ratios of isotopes of heavier elements with great precision. In the past, studies of stable isotope fractionation were limited to light elements such as carbon, hydrogen, oxygen, and nitrogen. The advent of multiple-collector inductively-coupled plasma-source mass spectrometry (MC-ICPMS) now allows geochemists to measure the high-temperature partitioning of isotopes of some of the heavier rock-forming elements including iron, silicon, magnesium, calcium, and nickel. Recent studies have used this tool to measure very small, but distinct, fractionations of iron and magnesium isotopes between minerals in mantle xenoliths (e.g., Williams et al., 2009; Young et

al., 2009; Huang et al., 2011). Comparisons of published inter-mineral isotope fractionation data with quantitative predictions, sometimes lead to confirmation of the theory behind such predictions and the rigor of the measurements, but other times result in ambiguity regarding both. For this reason it is essential to compare measurements of stable isotope fractionation in natural samples and theoretical predictions with experimental evidence wherever possible. Experimental studies have recently been completed for iron, silicon, and nickel isotope fractionation between minerals at high temperatures (e.g., Shahar et al., 2008; Shahar et al., 2011; Lazar et al., 2012). This study provides the first experimental data for magnesium isotope fractionation between minerals at high *T*-*P* conditions.

There is currently a lack of data concerning Mg isotope fractionation at high temperatures, which leaves the geochemist without a potentially powerful tracer. For example, the mineral olivine is potentially a reliable monitor of parent-body Mg isotope ratios (e.g., Norman et al., 2006), but only if the equilibrium inter-mineral fractionation between olivine and co-existing minerals at high temperatures is understood (except in cases where olivine completely dominates the Mg budget and the host rock is not a partial fractionate). While recent contributions have expanded the limited data for Mg fractionation in mantle minerals (e.g., Wiechert and Halliday, 2007; Handler et al., 2009; Young et al., 2009; Yang et al., 2009; Chakrabati and Jacobsen, 2010; Liu et al., 2011; Huang et al., 2011), they have also served to highlight disagreements among individual data sets as well as disagreements between those data sets and theoretical studies. Comparisons of theoretical predictions of inter-mineral Mg isotope fractionations by Schauble (2011) with spinel-olivine fractionation measurements from mantle xenolith samples in the current data set yield mixed results. Data from Young et al. (2009) agree (within error) with predictions for spinel-forsterite Mg fractionation both qualitatively (on the

basis of Mg coordination environments) and quantitatively. Data from Liu et al. (2011) are systematically lower than theoretical predictions by several tenths of per mil. This ambiguity highlights the need for experimental calibrations of inter-mineral Mg isotope fractionation, especially between spinel and olivine.

It is also important to understand the isotope fractionation between Mg bearing carbonates such as magnesite ($MgCO_3$) and other phases. Magnesian carbonate may be a major CO_2 reservoir in the upper mantle (e.g., Katsura and Ito, 1990). Several studies have investigated Mg isotope fractionations associated with carbonate precipitation and dissolution in aqueous solutions at low temperatures (e.g., Galy et al., 2002; Wombacher et al., 2006). However, it is not clear whether the experiments in these studies represent equilibrium or kinetic fractionations. Young and Galy (2004) showed that kinetic isotope effects likely contribute to the low $^{26}Mg/^{24}Mg$ seen in some carbonate precipitates in nature.

The kinetic versus equilibrium isotopic fractionation in carbonates is a vital issue for the geochemist to understand, and has been the topic of several recent experimental studies. For example, experiments by Mavromatis et al. (2009) demonstrate that Mg isotope fractionation between magnesite and fluid at low temperatures depends on precipitation rates and the concentration of aqueous organic ligands. They conclude that these factors may be responsible in part for the degree of Mg isotopic fractionation observed in nature. Pearce et al. (2012) found that Mg isotope exchange between magnesite and fluid displays both kinetic and equilibrium behaviors, but concluded that the kinetic signal would be eradicated by equilibrium fractionation in most natural samples. Both of these studies were based on experiments at low temperatures and involved fractionations between magnesite and liquid associated with precipitation and/or dissolution. New experiments are needed to determine the equilibrium fractionation of

magnesium isotopes between carbonates and other minerals at high temperatures where kinetic limitations are more easily circumvented; high-temperature experiments offer a means to separate the potentially confusing kinetic isotope signals from those representing equilibrium among co-existing minerals in nature.

In this study I use the three-isotope exchange method (Matsuhisa et al., 1978) to determine experimentally the equilibrium magnesium isotope fractionation factors between forsterite (Fo) and magnesite (Mgs), and between spinel (Spl) and magnesite as a function of temperature. Making use of the well-established advantages of using carbonate as an exchange medium and exchange partner (e.g. Clayton et al., 1989; Chako et al. 1996), I successfully achieved significant exchange of Mg isotopes between the two mineral pairs, Spl-Mgs and Fo-Mgs, at a range of temperatures. These experiments resulted in the direct determination of equilibrium Mg isotope fractionation between spinel and magnesite, and between forsterite and magnesite, which, when combined, allows for the indirect determination of the equilibrium fractionation between spinel and forsterite.

3.2 Methods

3.2.1 The three-isotope method combined with the use of carbonate as an exchange medium

The three-isotope method is a technique used by experimentalists to determine the equilibrium fractionation factor of stable isotopes between phases containing the isotope(s) of interest. The technique was first used by Matsuhisa et al. (1978) to obtain equilibrium fractionation factors for oxygen isotopes between quartz and water. Shahar et al. (2008) first applied the method to obtain the iron isotope fractionation between two solid phases, magnetite and fayalite. Subsequent studies have employed the technique to determine high temperature

equilibrium fractionation factors for other important non-traditional isotopes, Si and Ni, between two solid phases (e.g., Shahar et al., 2009, 2011; Lazar et al., 2012). Here we present a brief review of the method and describe how it was employed in the current study by utilizing carbonate as an exchange medium.

A schematic representation of the three-isotope method is shown in Figure 3.1. A three-isotope plot consists of two axes defined by two isotope ratios with the same denominator. The present study relies on changes in $^{25}Mg/^{24}Mg$ and $^{26}Mg/^{24}Mg$ isotope ratios relative to a standard reported in per mil (‰) in three-isotope space. The per mil deviations are expressed in conventional delta notation:

$$\delta^{i}\mathrm{Mg} = 10^{3}\left(\frac{\left({}^{i}\mathrm{Mg}/{}^{24}\mathrm{Mg}\right)_{\mathrm{Sample}}}{\left({}^{i}\mathrm{Mg}/{}^{24}\mathrm{Mg}\right)_{\mathrm{Standard}}} - 1\right) \quad (1)$$

where $i = 25$ or 26.

The goal of the three-isotope method is to derive the equilibrium isotope exchange from two isotopically distinct starting phases at temperatures and pressures of interest. One of the starting phases should be "normal", in that it has a natural isotope value and plots on the terrestrial fractionation line (TFL). The other starting phase must be "spiked" with a known amount of the isotope that exists in the denominator of both axes (in this case ^{24}Mg), thereby displacing it from the TFL in three-isotope space. A series of experiments is done involving mixtures (of known compositions) of the two starting materials at the same high *T-P* conditions, but for varying lengths of time. During the experiments, the isotopes should exchange between phases, resulting in two straight lines defined by the isotopic compositions of the two starting phases, and the subsequent isotopic compositions of each phase from the isothermal time-series. These two lines represent the phases driving their compositions toward equilibrium on a secondary fractionation line (SFL), which is defined by the bulk composition (starting mixtures

of experiments) of the system. The most powerful part of the three-isotope method is that the two phases do not have to actually reach equilibrium during the experiments to be successful. The method allows the experimentalist to use isothermal time-series to extrapolate towards the SFL, which allows for the determination of the equilibrium fractionation between the two phases. The difference between these extrapolated intersections is the equilibrium inter-mineral fractionation value at a given temperature, e.g., for the present study:

$$\Delta^{26}\mathrm{Mg}_{\mathrm{Spl\text{-}Mgs}} = \delta^{26}\mathrm{Mg}_{\mathrm{Spl}} - \delta^{26}\mathrm{Mg}_{\mathrm{Mgs}} \quad (2)$$

where $\delta^{26}\mathrm{Mg}_{\mathrm{Spl}}$ is equal to the value of the open circle in Figure 3.1 and $\delta^{26}\mathrm{Mg}_{\mathrm{Mgs}}$ is equal to the value of the open triangle.

The extrapolated time series of $\delta^{26}\mathrm{Mg}_{\mathrm{Spl}}$ and $\delta^{26}\mathrm{Mg}_{\mathrm{Mgs}}$ data (Figure 1, t_0–t_2) are fit linearly using the new "York" weighted regression algorithm (Mahon, 1996). Following Shahar et al. (2008), the uncertainties in the slopes and intercepts of the regression analyses are used to calculate 2σ error envelopes. Errors and their propagations are discussed in §3.2.5. The slope of the TFL and SFL, γ, is taken to be 0.521 based on the expression for equilibrium mass fractionation,

$$\gamma = \frac{\left(\frac{1}{m_{24}} - \frac{1}{m_{25}}\right)}{\left(\frac{1}{m_{24}} - \frac{1}{m_{26}}\right)} \quad (3)$$

where m_i is the precise mass of each isotope i. The York regression technique is also used to compute linear fits and error envelopes for the temperature versus fractionation data (§3.2.5).

There are two requirements for successfully determining equilibrium fractionation factors with the three-isotope method: (1) varying degrees of isotope exchange must be achieved between phases of interest during the experiments, and (2) all phases containing the isotopes of interest must be completely separated after the experiments for analysis. In past studies

involving mineral-mineral exchange, the first requirement was met by utilizing heterogeneous reactions to promote isotope exchange. For example, Shahar et al. (2009) forced iron isotope exchange between fayalite and magnetite as a function of temperature in the assemblage magnetite+quartz+fayalite comprising the "QFM" oxygen fugacity buffer. Lazar et al. (2012) also used heterogeneous reaction to promote Ni isotope exchange between Ni-metal and Ni-talc by converting spiked NiO to Ni-talc at high *T-P*, leading to a final assemblage of metal+talc+quartz+H_2O. For the present study, no such reactions were stable that would result in spinel and forsterite as the only Mg-bearing phases. I solved this problem by utilizing magnesite as both an exchange medium for Mg isotopes, and exchange partner with both spinel and forsterite.

The second requirement for successful application of the three-isotope method (complete separation of run products containing the specified isotope(s)), is an equally important part of the experiment. Contamination of either phase with the other would result in spurious data and would compromise the rigor of any fractionation factor derived using such analyses. Both Shahar et al. (2008) and Lazar et al. (2012) were able to separate their run products with a strong magnet because one of the phases of interest in their final assemblages was magnetic, and other was not. None of the phases of interest in this study are magnetic. Again, the use of carbonate as exchange medium and partner, supplies a solution to this challenge. Taking advantage of the high solubility of magnesite in warm HCl, we preferentially dissolved the magnesite after each experiment, allowing for complete separation of phases for analyses. The specifics of my experimental methods are discussed in the following sections.

3.2.2 Piston-cylinder experiments

Starting materials were finely ground powders of synthetic, high-purity forsterite, spinel, and anhydrous magnesite. Forsterite and spinel were both synthesized in the lab by combining stoichiometric amounts of ultrapure powders of MgO + SiO_2 and MgO + Al_2O_3 (Alfa Aesar), respectively. The MgO component of both mixtures was spiked with excess ^{24}Mg by mixing the ultrapure MgO (Alpha Aesar) with high-purity α-^{24}MgO (Oak Ridge National Laboratory Batch 217101, ^{24}Mg 99.92%, ^{25}Mg 0.05%, ^{26}Mg 0.03%) in a ~ 99:1 ratio, ground twice under acetone in a mortar and pestle for ~30 min.

To synthesize forsterite, the stoichiometric mixture of SiO_2 powder + spiked MgO powder was homogenized by grinding in a mortar and pestle, then devolatilized in a platinum crucible at 800°C approximately 120 minutes, cooled, and finely ground again in an agate mortar and pestle. The material was then pelletized and sintered in an upright furnace at 1400°C for 72 hours, resulting in > 99% pure forsterite as determined by X-ray diffraction. For spinel synthesis, the stoichiometric Al_2O_3 + spiked MgO was homogenized and devolatilized the same as for forsterite, but then the powdered oxide mix was synthesized hydrothermally in a piston-cylinder apparatus. Anhydrous synthetic magnesite was purchased from Sargent-Welch. Magnesium isotope compositions of starting materials are given in Table 1.

For each experiment two separate capsules were made: one containing forsterite + magnesite, and one containing spinel + magnesite (both with approximately 1:1 molar Mg proportions). To make the capsules, starting assemblages were loaded into segments of Au tubing of 3.5 mm outer-diameter and 0.18 wall thickness. Au was used because of its low permeability to H_2 at experimental conditions (Eugster and Wones, 1962), which prevented the reduction of carbon in magnesite. After loading, the tubes were welded shut with a carbon electrode, and the sealed capsules were loaded side by side into a 1-inch diameter piston-cylinder

assembly with NaCl pressure medium and graphite heater sleeve. A thin piece of Au was placed on top of the capsules to prevent puncture by the thermocouple. Temperature was monitored with $Pt/Pt_{90}Rh_{10}$ thermocouples in contact with the capsules, with no correction for the effect of pressure on emf (Ulmer, 1971). The accuracy of the reported temperature is estimated to be ±3 °C. All experiments were brought to a pressure of 7 kbar and then heated to the desired run temperature at a rate of ~20 °C per minute. As the assembly heated, thermal expansion of the assembly brought the pressure to 10 kbar. Pressure was monitored with a Heise Bourdon-tube pressure gauge and maintained to within 200 bar gauge pressure. Experiments were performed at 600 °C - 800 °C for 15 to 240 min. Experiments were quenched by cutting power to the apparatus, which resulted in cooling of the experiment to <50 °C in <1 min (Manning and Boettcher, 1994). Following each run, the capsules were retrieved, cleaned, and weighed. They were then opened with a clean razor blade and run products were carefully removed and placed in glass containers.

3.2.3 Sample separation and purification

Measurement of inter-mineral isotope fractionation of Mg requires complete separation of the magnesium-bearing phases prior to mass spectrometric analysis. The starting assemblages of the Spl-Mgs and Fo-Mgs experimental charges were loaded into the Au capsules as loose microscopic powders. The post-run products were re-crystallized to various extents, but were still too small and intermingled to be quantitatively separated by hand. Complete separation of run products was achieved by developing a procedure for the preferential dissolution of magnesite.

Run products were transferred into Savillex vials and 1 mL of warm (150 °C) 1 N HCl was added. The vials were sonicated for ~5 min, then centrifuged for ~2 min to separate the remaining solids from the liquid which now contains dissolved magnesite. The supernatant fluid was then carefully poured into a new Savillex vial through filter paper (to exclude any crystals that might be poured off accidentally). This procedure was repeated 3 times with warm HCl, then twice more with room temperature Millipore H_2O. The supernatant fluid portion from this procedure, which now contains only dissolved magnesite from the run, is dried at 120 °C, redissolved in aqua regia, dried again, then picked up in 2% HNO_3 for mass spectrometry. The leftover solids in the vial, which were >99% Fo or Spl, were also dried at 120 °C.

To test the integrity of this procedure, mixtures of isotopically spiked Spl + terrestrial Mgs and spiked Fo + terrestrial Mgs (compositions of starting assemblages) were used. Both mixtures underwent the preferential dissolution procedure as described above, their respective separates were then dissolved, and in the case of Spl, put through Mg purification columns (as described below). Each separate was then analyzed by MC-ICPMS and found to be identical (within error of analysis) to measured values of original starting materials that did not undergo the preferential dissolution procedure, thus proving the successful separation of phases. Based on the precision of the isotope ratio analysis, the maximum intermingling of Mg from this procedure is ~5%.

Fo and Spl crystals from all experiments were dissolved in sealed Teflon vessels jacketed in steel acid digestion bombs (Parr Instrument Co.) in a 1:1 mixture of omnigrade HF and HNO_3 at temperatures of 230 °C for 72 hours. Dissolved samples were transferred to Savillex vials and evaporated to dryness at 120 °C. Dried samples were redissolved in aqua regia at 120 °C for 24 hours followed by evaporation to dryness. Forsterite samples were then dissolved again in 2%

HNO_3 for mass spectrometry. Spinel samples were redissolved in 1 N HNO_3 in preparation for ion exchange column chemistry.

Magnesium from spinel was purified by ion exchange chromatography in HEPA filtered laminar flow boxes within a class 100 clean laboratory using a one-column procedure modified from Young et al. (2009). We used PFA micro-columns measuring 120 mm × 4 mm with 70 ml reservoirs. These columns contain 1.5 ml (wet) of Bio-Rad™ AG 50W-X12 resin in 200 to 400 mesh hydrogen form. The 2.1 meq capacity of the resin translates to a column capacity of 36 mg Mg^{2+}. Columns were washed initially with 0.5N HF followed by a rinse with ~18 $M\Omega cm^2/cm$ water, cleaning with 6N HCl, and further rinsing. Resins were conditioned with 1N HNO_3. A typical load on the column consists of between ~50 μg of Mg in 300μl of 1N HNO_3. This column is used to separate Mg from Al by eluting Mg with 70 ml of 1N HNO_3. Recovered magnesium is again evaporated to dryness, then redissolved in 2% HNO_3 for mass spectrometry.

The most reliable indicator of complete recovery of Mg in the presence of matrix elements on the columns was the absence of measurable shifts in $^{25}Mg/^{24}Mg$ and $^{26}Mg/^{24}Mg$ following Mg recovery. These "zero enrichments" were checked for in-house reference Mg upon each load of resin. Blanks of Mg were below detection. Forsterite and magnesite samples did not go through this column chemistry procedure because the dissolution procedure alone served to purify Mg.

3.2.4 Mass spectrometry

All Mg isotope ratio measurements were made using a Thermo-Finnigan Neptune MC-ICPMS. The instrument has a fixed array of 9 Faraday collectors each with amplifier resistors of $10^{11}\Omega$. Sample purity was checked by monitoring $^{27}Al+$, $^{44}Ca+$, $^{56}Fe+$, $^{52}Cr+$, $^{55}Mn+$ and $^{56}Fe+$.

In all cases the abundances of these potential impurities were <1at.% of the analyte Mg concentration. Such low impurity/Mg ratios are well below thresholds for discernible matrix effects on Mg isotope ratio measurements as determined by tests using various mixtures of these elements. Samples and standard were analyzed as ~2 ppm Mg in 2% HNO_3 aspirated through a Cetac Aridus I® desolvating nebulizer (samples were run in dry plasma) with addition of N_2. Potential mass interferences from C_2^+ and CN^+ (below detection) were resolved from $^{24}Mg^+$ and $^{26}Mg^+$, respectively, by operating at a high mass resolving power of >10,000 (m/Δm as measured on the off-axis major beam peak shape). Samples were analyzed 8 to 13 times with each analysis consisting of 20 cycles of ~4 second integrations. Corrections for instrumental mass bias were obtained by sample-standard bracketing with peak height matching between sample and standard to better than 5%. Uncertainties for each datum are reported as 2 standard errors (2se), representing the uncertainty in the mean from the mass spectrometry blocks of 20 cycles.

In this study it is the relative differences in Mg isotope ratios that are of interest. Therefore, all values for Mg isotope ratios presented in this study were obtained by using Spex CertiPrep™ Mg concentration standard solutions for our internal standard. All data are presented in the conventional delta notation (Eq. 1). Over the course of these experiments, we ran out of our initial standard solution (Mg Spex 3), and were forced to switch to a new bottle (Mg Spex 4). Therefore one should not make direct comparisons of the $\delta^{25}Mg$ and $\delta^{26}Mg$ values from the 700 °C experiments with those of the 600 °C and 800 °C experiments. This does not affect the final determination of equilibrium fractionation because it is the relative differences between delta values in an experimental series, not the absolute measured values, that matter when determining fractionation between phases at a given temperature. We did not convert our internal standard values to the DSM3 scale because this incurs an additional systematic error that

could degrade the quality of the derived fractionation factors. Conversions from Spex 3 and Spex 4 to DSM3 scale can be made using the following values: $\delta^{25}Mg^{Spex3/DSM3}$ = -1.0533 ± 0.0077, $\delta^{26}Mg^{Spex3/DSM3}$ = -2.0605 ± 0.0068, $\delta^{25}Mg^{Spex4/DSM3}$ = -1.7992 ± 0.0053, $\delta^{26}Mg^{Spex4/DSM3}$ = -3.4874 ± 0.0045. Conversion between Spex 3 and Spex 4 scales is achieved by using $\delta^{25}Mg^{Spex3/Spex4}$ = 0.7299 ± 0.0085 and $\delta^{26}Mg^{Spex3/DSM3}$ = 1.4461 ± 0.0063.

3.2.5 Analytical errors and their propagation

Uncertainties in $\Delta^{26}Mg_{Fo\text{-}Mgs}$ and $\Delta^{26}Mg_{Spl\text{-}Mgs}$ reported in this study are derived from isotope ratio measurements of forsterite and magnesite, and spinel and magnesite, respectively, from a series of experiments. The method of propagating the uncertainties in individual analyses to the final equilibrium value is the same as that used by Shahar et al. (2008) for iron isotopes, and is described below for our magnesium isotope experiments.

The uncertainty in each isotope ratio measurement is the standard error of 8-13 MC-ICPMS analyses of the same sample solution. These analyses represent mineral separates from each experiment run at specific temperatures and times. Analyses of a given mineral representing an isothermal time series are regressed using the "new" York regression (Mahon, 1996), resulting in a best fit line and associated uncertainties in slope and intercept for each mineral from the experimental time series. The equilibrium $\Delta^{26}Mg_{Fo\text{-}Mgs}$ and $\Delta^{26}Mg_{Spl\text{-}Mgs}$ for that temperature are obtained from the difference in the intersection of the forsterite (or spinel) and magnesite regression lines with the secondary fractionation line in three-isotope space using the relation

$$\delta^{26}\mathrm{Mg}_{\mathrm{Eq},\,i} = \frac{-b_1 + b_2}{m_1 - \gamma} \qquad (4)$$

where $\delta^{26}Mg_{Eq,i}$ is the projected $\delta^{26}Mg$ value for mineral i at equilibrium, m_1 is the slope of the regressed data points for mineral i, γ is the slope of the secondary fractionation line, b_1 is the intercept of the best-fit line through the regressed data points, and b_2 is the intercept of the secondary fractionation line.

Uncertainties in the derived $\Delta^{26}Mg_{Fo\text{-}Mgs}$ and $\Delta^{26}Mg_{Spl\text{-}Mgs}$ values are obtained from the intersections of the 2σ error envelopes for the forsterite (or spinel) and magnesite best-fit lines with the secondary fractionation line. The $\delta^{26}Mg$ values for the intersection of the SFL and the error envelope for each best-fit line are calculated as in Shahar et al. (2008). Standard errors for the equilibrium $\delta^{26}Mg$ values obtained for forsterite, spinel, and magnesite are then propagated through to the final $\Delta^{26}Mg_{Fo\text{-}Mgs}$ and $\Delta^{26}Mg_{Spl\text{-}Mgs}$ by taking the square root of the sum of squares of the uncertainties for each extrapolated equilibrium $\delta^{26}Mg$ value.

The $\Delta^{26}Mg_{Spl\text{-}Fo}$ values at each temperature were calculated from the difference between $\Delta^{26}Mg_{Spl\text{-}Mgs}$ and $\Delta^{26}Mg_{Fo\text{-}Mgs}$ determined by experiments. The uncertainty associated with $\Delta^{26}Mg_{Spl\text{-}Fo}$ is therefore also calculated by summing the uncertainties in quadrature. Finally the values of $\Delta^{26}Mg_{\text{mineral a-mineral b}}$ at each temperature were regressed by forcing the intercept through the origin using the new York regression (Mahon, 1996) in order to obtain final equations for the temperature dependence of $\Delta^{26}Mg_{Fo\text{-}Mgs}$, $\Delta^{26}Mg_{Spl\text{-}Mgs}$, and $\Delta^{26}Mg_{Spl\text{-}Fo}$ with associated uncertainty.

3.3 Results

Starting compositions of the spinel, forsterite, and magnesite for each temperature are given in Table 3.1. Results of the Spl-Mgs and Fo-Mgs experiments at 600 °C, 700 °C and 800 °C at 10 kbar are given in Table 3.2.

3.3.1 Textural evidence of exchange mechanism

Before considering the results of the three-isotope experiments, it is instructive to examine possible mechanisms of exchange responsible for the isotopic evolution observed in the experiments. Figure 3.2 is a series of scanning electron microscope (SEM) backscattered electron images of the forsterite starting material and forsterite-magnesite run products. The synthetic forsterite starting material (before powdering) consists of subhedral crystals ranging in size from sub-micron to ~50 μm grains (Figure 3.2a). Run products from an 800 °C Fo-Mgs run are shown in Figure 3.2b. After the magnesite has been removed from the run products by preferential dissolution, as shown in Figure 3.2c, clear evidence of reaction between forsterite and magnesite at high *P-T* is revealed in the form of new crystal faces on forsterite grains. Based on these textural observations and the anhydrous nature of the present experiments, we suggest that the mechanism of chemical and isotopic change may be due to annealing and recrystallization at high temperature and pressure (e.g. Griggs et al., 1960; Chiba et al. 1989; Clayton et al., 1989). Similar evidence for grain growth was observed in Spl-Mgs experiments, suggesting a similar exchange mechanism.

3.3.2 Forsterite-magnesite experiments

Mg isotope exchange experiments involving forsterite and magnesite were performed at 10 kbar and 800 °C (Figure 3.3a, b) for 15, 30, 60, and 120 min, 700 °C (Figure 3.3c, d) for 15, 30, and 60 min, and at 600 °C (Figure 3.3e, f) for 60, 120, and 240 min. None of these experiments attained isotopic equilibrium, as indicated by the fact that none of the experimental run products have compositions on the secondary fractionation lines. The equilibrium Mg isotope ratios of forsterite and magnesite were therefore obtained by extrapolation to the

respective SFLs. The validity of linear extrapolation to the SFL has been investigated and verified by Lazar et al. (2012). Extrapolation of the regressed data to the SFLs at each temperature yielded $\Delta^{26}Mg_{Fo\text{-}Mgs}$ values of 0.036 ± 0.043‰ at 800 °C, 0.107 ± 0.095‰ at 700 °C, and 0.438 ± 0.098‰ at 600 °C.

3.3.3 Spinel-magnesite experiments

Experiments between spinel and magnesite were performed (in tandem with the Fo-Mgs experiments) at 10 kbar and 800 °C (Figure 3.4a, b) for 15, 30, 60, and 120 min, 700 °C (Figure 3.4c, d) for 15, 30, and 60 min, and at 600 °C (Figure 3.4e, f) for 60, 120, and 240 min. As with the Fo-Mgs experiments, none of these experiments attained isotopic equilibrium. Therefore the equilibrium Mg isotope ratios of spinel and magnesite at each temperature were obtained by linear extrapolation to the respective SFLs. Extrapolation of the regressed data to the SFLs at each temperature yielded $\Delta^{26}Mg_{Sp\text{-}Mgs}$ values of 0.896 ± 0.285‰ at 800 °C, 1.098 ± 0.273‰ at 700 °C, and 1.727 ± 0.376‰ at 600 °C.

3.3.4 Spinel-forsterite fractionation by difference

From the experimentally determined equilibrium fractionation values for forsterite-magnesite and spinel-magnesite, we determine equilibrium fractionation between spinel and forsterite by difference, yielding $\Delta^{26}Mg_{Sp\text{-}Fo}$ values of 0.860 ± 0.288‰ at 800 °C, 0.992 ± 0.289‰ at 700 °C, and 1.289 ± 0.388‰ at 600 °C.

3.3.5 Temperature dependence of equilibrium Mg isotope exchange

The experimentally determined Fo-Mgs and Spl-Mgs fractionations are plotted as a function of temperature in Figure 3.5a, b, along with theoretical lines for forsterite and spinel equilibrium fractionation with magnesite from Schauble (2011). Regressing these data by forcing the best-fit lines through the origin (Mahon, 1996), leads to equations for the temperature dependence of the Fo-Mgs and Spl-Mgs fractionation factors:

$$\Delta^{26}\mathrm{Mg}_{\text{Fo-Mgs}} = 0.06\ (\pm 0.04) \times 10^6/T^2 \quad (3)$$

$$\Delta^{26}\mathrm{Mg}_{\text{Spl-Mgs}} = 1.04\ (\pm 0.20) \times 10^6/T^2 \quad (4)$$

with 2se uncertainty.

Using the differences between the experimentally determined forsterite-magnesite and spinel-magnesite fractionation at each temperature, I obtain an equation for the temperature dependence of the spinel-forsterite fractionation factor:

$$\Delta^{26}\mathrm{Mg}_{\text{Spl-Fo}} = 0.96\ (\pm 0.21) \times 10^6/T^2 \quad (5)$$

Figure 3.5c shows spinel-forsterite equilibrium fractionation as a function of temperature plotted together with a predicted fractionation based on *ab initio* density functional perturbation theory calculations from Schauble (2011).

3.4 Discussion

3.4.1 Comparison to theoretical predictions

Recent theoretical studies have predicted the magnitude and direction of magnesium isotope fractionation between various phases and molecules at a range of temperatures and pressures (Black et al., 2007; Schauble, 2011; Rustad et al., 2010). Of these, only Schauble (2011) reported theoretical calculations of equilibrium magnesium isotope fractionations between Mg-bearing oxides, silicates, and carbonates. We therefore compare our experimentally

determined equilibrium fractionation factors (expressed as $\Delta^{26}Mg_{Fo\text{-}Mgs}$, $\Delta^{26}Mg_{Sp\text{-}Mgs}$, and $\Delta^{26}Mg_{Sp\text{-}Fo}$) with those predicted by Schauble (2011) in Figures 3.5a-c.

Mass-dependent equilibrium stable isotope fractionation is driven by changes in vibrational energies in crystals due to isotopic substitution (e.g. Urey, 1947; Bigeleisen and Mayer, 1947). Schauble (2011) used density functional perturbation theory (DFPT) to calculate vibrational frequencies in magnesium-bearing crystals, allowing for the calculation of associated mass-dependent shifts in frequencies. The calculations by Schauble (2011) suggest that inter-mineral Mg isotope fractionations should be large at a range of temperatures: several per mil at room temperature to several tenths of per mil at igneous and metamorphic temperatures. This work predicts that spinel will have higher $^{26}Mg/^{24}Mg$ than coexisting silicate phases (e.g. $\Delta^{26}Mg_{Sp\text{-}Fo} = 0.59$ at 1000 °C), while carbonates will have low $^{26}Mg/^{24}Mg$ with respect to spinel and silicates, the affinity for the heavy isotopes correlating inversely with coordination number.

The experimentally determined temperature-dependent fractionation factors are compared with theoretical predictions from Schauble (2011) in Figure 3.5a-c. In the case of both forsterite-magnesite (Figure 3.5a) and spinel-magnesite (Figure 3.5b), our experimentally determined Δ vs. $1/T^2$ lines have shallower slopes than the theoretically predicted lines. Also, in both instances, the 600 °C datum lies directly on the theoretical line, while the data for 700 and 800 °C lie below. The observed discrepancies could be due to experimental and/or analytical error in one or more sets of experiments involving magnesite in this study, although we have no reason to believe that the 600 °C data are any more accurate than the higher temperature data. In fact, in both sets of 600 °C experiments, the run products were the less equilibrated than in the respective 700 and 800 °C series, requiring greater extrapolation to equilibrium values, and therefore higher degrees of uncertainty.

The spinel-forsterite fractionation factor determined by this study agrees surprisingly well with theoretical predictions. Figure 3.5c shows the experimentally derived spinel-forsterite equilibrium fractionation as a function of temperature compared with the theoretically predicted fractionation from Schauble (2011). The experimentally and theoretically-predicted lines are indistinguishable at higher temperatures at the scale shown. Because the spinel-forsterite fractionation factor was determined by the difference between the spinel-magnesite and forsterite-magnesite fractionations at each temperature, discrepancies between my carbonate-mineral fractionations and those predicted by theory discussed above cancel in the final $\Delta^{26}\mathrm{Mg}_{\mathrm{Sp\text{-}Fo}}$ values.

3.4.2 Spinel-olivine Mg isotope geothermometry

Magnesium stable isotope geochemistry is a rapidly growing field with applications to many important planet-forming processes. Several recent publications investigating inter-mineral Mg isotope fractionation have reported small but resolvable Mg isotope fractionation (up to ~0.4‰) between coexisting pyroxene and olivine in mantle rocks (e.g. Weichert and Halliday, 2007; Handler et al., 2009; Yang et al., 2009; Young et al., 2009; Liu et al., 2011). Only two studies to date include measurements of Mg isotope fractionation between coexisting spinel and olivine, those of Young et al. (2009) and Liu et al. (2011). Both studies found that in all cases in mantle xenoliths, spinel is higher in $^{26}\mathrm{Mg}/^{24}\mathrm{Mg}$ than coexisting olivine. Although the studies agree as to the direction of fractionation ($\Delta^{26}\mathrm{Mg}_{\mathrm{Sp\text{-}Fo}} > 0$), they report small but resolvable differences in magnitudes. These small differences are important to understand if one wishes to use Mg isotopes as a geothermometer or a tracer of mantle processes.

The clearest picture of the meaning of observed fractionation will come from comparing measurements of natural samples with theoretical predictions and experimental evidence. Figure 3.6 shows spinel-olivine Mg isotope fractionation data from Young et al. (2009) and Liu et al. (2011), along with theoretically (Schauble, 2011) and experimentally (this study) determined fractionation lines. Spinel-olivine data from Liu et al. (2011) fall below the theoretically-predicted and experimentally-determined Al-spinel-forsterite fractionation lines, while data from Young et al. (2009) agree, within error, with both. Liu et al. (2011) argue that the reason for the discrepancy between their data and expected values is the complicating effects of chemical substitutions in spinels and the effects that these substitutions have on fractionation. Theory supports this observation.

Schauble (2011) posited that Mg isotope partitioning in normal spinel structures ($A^{2+}B_2^{3+}O_4^{2-}$) depends strongly on the composition of the octahedral (i.e., B^{3+}) ion. Evidence for this assertion is provided by the widely different predictions for pure spinel-forsterite, magnesiochromite-forsterite, and magnesioferrite-forsterite Mg isotope fractionation factors calculated by Schauble (2011) (shaded lines in Figure 3.6). Although this phenomenon is not fully understood, it appears that high $^{26}Mg/^{24}Mg$ is associated with low octahedral-cation atomic number (i.e., Al vs. Cr or Fe^{3+}). Therefore, natural spinels with varying amounts of Al, Cr, and Fe^{3+} in the octahedral position will likely have $\Delta^{26}Mg_{Sp\text{-}Fo}$ values intermediate to those predicted for pure spinel-forsterite, magnesiochromite-forsterite, and magnesioferrite-forsterite.

There is strong agreement between equilibrium $\Delta^{26}Mg_{Sp\text{-}Fo}$ values from the present work, which uses end-member synthetic $MgAl_2O_4$ spinel and forsterite, and those predicted by Schauble (2011) for pure spinel and forsterite, thus supporting the use of Mg isotopes as a valid geothermometer. However, since natural samples are rarely end-member compositions, caution

should be exercised when extracting temperatures based on Mg isotope ratios alone. In the study by Young et al. (2009), the ^{VI}Cr and $^{VI}Fe^{3+}$ contents of the spinels suggest that the measured spinel-forsterite fractionations are high compared with theory if the fractionation factors scale linearly with substitutions for ^{VI}Al. If so, the correspondence between temperatures obtained from the Mg isotope fractionation and that from spinel ordering would be fortuitous. Until more experiments are performed with different spinel compositions, the experimental evidence provided here should be combined with the theoretical predictions of Mg isotope partitioning as a function of chemical composition (Schauble, 2011) to evaluate the coexisting spinel-olivine inter-mineral fractionation in natural samples.

3.4.3 Magnesite in the mantle

Subducted oceanic crust contains significant amounts of carbonate (Alt and Teagle, 1999), which are not quantitatively removed by devolatilization reactions (Yaxley and Green, 1994; Molina and Poli, 2000; Kerrick and Connolly, 2001). Experimental studies have shown that magnesite is a major stable carbonate at mantle conditions (e.g. Biellman et al., 1993). It therefore has the ability to store carbon in the Earth's upper and lower mantle and is potentially a carrier of carbon in subducting plates (Kushiro et al., 1975; Brey et al., 1983; Katsura et al., l99l; Biellmann et al., 1993; Redfern et al., 1993; Gillet, 1993). While carbon isotopes are useful for identifying recycled organic carbonate, they are not very sensitive to inorganic carbonate due to the smaller fractionations involved (Yang et al., 2012). Therefore, magnesium isotopes are potentially powerful tracers of interactions between mantle rocks and recycled carbonate. The experimentally determined Mg-isotope fractionation between magnesite and spinel and magnesite and forsterite from the present study provide guidelines for the interpreting the $\delta^{26}Mg$

signals of high-*T* magnesite coexisting with silicates and oxides.

Magnesite also occurs as an alteration product in Mg-rich igneous and metamorphic rocks. It has been observed in kimberlites, eclogites, and mantle peridotites (e.g., McGetchin and Besancon, 1973; Lappin and Smith, 1978; Yang et al., 1993; Zhang and Liou, 1994). Yang et al. (1993) reported magnesite-bearing garnet peridotite consisting of garnet + forsterite + enstatite + diopside + magnesite. They found magnesite occurring as an interstitial grain among olivine crystals and in equilibrium with olivine. This is the perfect example of the type of natural sample for application of my experimental data. Unfortunately, there are no existing Mg isotope data for coexisting magnesite-forsterite or magnesite-spinel to compare with the findings of the present study. In the future, however, my experimental $\Delta^{26}Mg_{Fo\text{-}Mgs}$ and $\Delta^{26}Mg_{Sp\text{-}Mgs}$ values can be used to understand geochemical processes affecting igneous and metamorphic rocks such as those described above.

3.5 Conclusions

This study makes use of the three-isotope exchange method to experimentally determine the equilibrium magnesium isotope fractionation factors between forsterite and magnesite, and between spinel and magnesite, as a function of temperature. By using carbonate as both exchange medium and exchange partner, I successfully achieved significant exchange of Mg isotopes between the two mineral pairs, Spl-Mgs and Fo-Mgs, at 600, 700, and 800 °C. These experiments resulted in the direct determination of equilibrium Mg isotope fractionation between Spl and Mgs, and between Fo and Mgs, which, when combined, allows for the indirect determination of the equilibrium fractionation between Spl and Fo. Comparisons of experimental results reported here with theoretical predictions reveals close agreement for

spinel-olivine fractionation, but some discrepancies for forsterite-magnesite and spinel magnesite fractionation. In both cases the experimentally determined values ($\Delta^{26}Mg_{Fo\text{-}Mgs}$ and $\Delta^{26}Mg_{Sp\text{-}Mgs}$) are lower than those predicted by theoretical calculations. Results of experiments may place constraints on Mg isotopic variations observed in natural systems where spinel and olivine coexist, and where magnesite coexists with olivine and/or spinel.

Table 3.1
Mean relative isotopic compositions of experimental starting materials for each isothermal time series.

	Starting Mineral	δ^{25}Mg (‰)	2se	δ^{26}Mg (‰)	2se
800 °C	Forsterite	-12.744	0.008	-13.147	0.009
	Spinel	-12.842	0.013	-13.544	0.050
	Magnesite	1.792	0.012	3.404	0.011
700 °C	Forsterite	-10.844	0.010	-11.700	0.022
	Spinel	-13.419	0.042	-14.576	0.040
	Magnesite	1.0058	0.034	1.928	0.012
600 °C	Forsterite	-12.744	0.008	-13.147	0.009
	Spinel	-12.842	0.013	-13.544	0.050
	Magnesite	1.792	0.012	3.404	0.011

Table 3.2
Experimental Results

Temp (°C)	Run	Time (min)	Mineral	δ^{25}Mg (‰)	2se	δ^{26}Mg (‰)	2se
600	Sp516121	240	Spinel	-10.672	0.012	-10.898	0.016
600	Sp516122	60	Spinel	-11.282	0.006	-11.616	0.022
600	Sp516123	120	Spinel	-11.213	0.010	-11.517	0.020
600	Sp516121	240	Magnesite	0.446	0.014	1.809	0.022
600	Sp516122	60	Magnesite	1.015	0.010	2.455	0.018
600	Sp516123	120	Magnesite	1.199	0.012	2.653	0.010
600	Fo516121	240	Forsterite	-10.315	0.018	-10.352	0.010
600	Fo516122	60	Forsterite	-10.216	0.012	-10.192	0.016
600	Fo516123	120	Forsterite	-10.533	0.018	-10.594	0.018
600	Fo516121	240	Magnesite	-1.160	0.014	0.000	0.014
600	Fo516122	60	Magnesite	-1.333	0.010	-0.154	0.008
600	Fo516123	120	Magnesite	-1.531	0.014	-0.293	0.016
700	Sp713111	15	Spinel	-9.153	0.032	-9.641	0.024
700	Sp713112	30	Spinel	-10.011	0.074	-10.661	0.010
700	Sp713113	60	Spinel	-12.238	0.034	-13.214	0.026
700	Sp713111	15	Magnesite	-0.860	0.014	-0.310	0.010
700	Sp713112	30	Magnesite	0.067	0.026	0.742	0.026
700	Sp713113	60	Magnesite	0.247	0.030	0.963	0.022
700	Fo713111	15	Forsterite	-7.810	0.008	-8.072	0.022
700	Fo713112	30	Forsterite	-8.005	0.005	-8.371	0.008
700	Fo713113	60	Forsterite	-7.237	0.035	-7.441	0.018
700	Fo713111	15	Magnesite	-1.479	0.012	-0.889	0.014
700	Fo713112	30	Magnesite	-1.372	0.006	-0.750	0.009
700	Fo713113	60	Magnesite	-1.674	0.016	-1.110	0.018
800	Sp517122	120	Spinel	-10.577	0.030	-10.810	0.035
800	Sp518121	60	Spinel	-10.752	0.042	-11.060	0.096
800	Sp51122	30	Spinel	-10.190	0.042	-10.341	0.024
800	Sp1014111	15	Spinel	-11.208	0.006	-11.459	0.035
800	Sp1018111	30	Spinel	-11.067	0.010	-11.323	0.010
800	Sp1018112	60	Spinel	-10.845	0.004	-11.048	0.090
800	Sp517122	120	Magnesite	-0.097	0.026	1.309	0.050
800	Sp518121	60	Magnesite	-0.560	0.044	0.783	0.034
800	Sp51122	30	Magnesite	0.204	0.034	1.577	0.057
800	Sp1014111	15	Magnesite	0.562	0.010	1.981	0.022
800	Sp1018111	30	Magnesite	0.282	0.021	1.645	0.026
800	Sp1018112	60	Magnesite	0.206	0.020	1.565	0.016
800	Fo517122	120	Forsterite	-6.714	0.013	-6.284	0.016
800	Fo518121	60	Forsterite	-8.931	0.012	-8.825	0.020
800	Fo51122	30	Forsterite	-8.762	0.015	-8.634	0.042
800	Fo1014111	15	Forsterite	-7.767	0.013	-7.448	0.010
800	Fo1018111	30	Forsterite	-7.335	0.010	-6.974	0.010
800	Fo1018112	60	Forsterite	-8.502	0.006	-8.277	0.008

800	Fo517122	120	Magnesite	-3.034	0.010	-2.087	0.012
800	Fo518121	60	Magnesite	-2.113	0.013	-1.050	0.018
800	Fo51122	30	Magnesite	-2.031	0.012	-0.960	0.014
800	Fo1014111	15	Magnesite	-1.591	0.022	-0.429	0.055
800	Fo1018111	30	Magnesite	-2.178	0.016	-1.113	0.026
800	Fo1018112	60	Magnesite	-1.956	0.022	-0.881	0.037

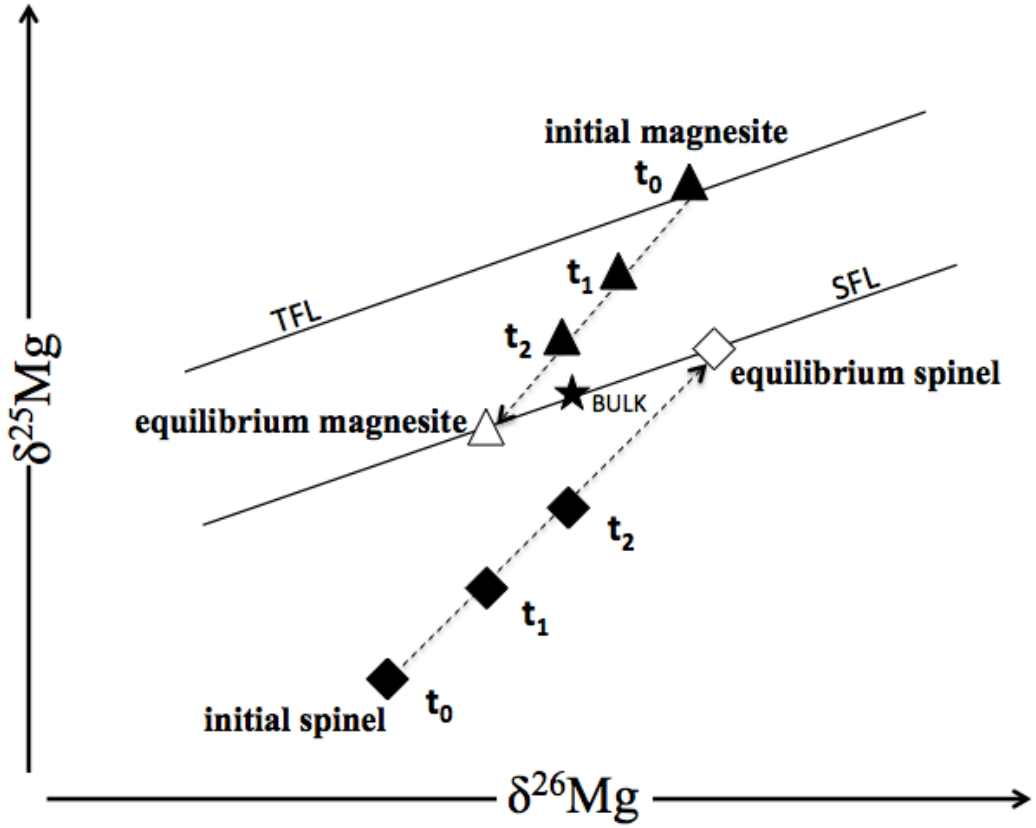

Figure 3.1 Schematic diagram of the three-isotope exchange method showing the terrestrial fractionation line (TFL) where all natural samples lie, the secondary fractionation line (SFL), which has the same slope as the TFL but is offset due to a ^{24}Mg spike affecting the bulk composition of the system. The intersections of the trend lines from the experiments with the SFL define equilibrium isotopic compositions. See text for further explanation.

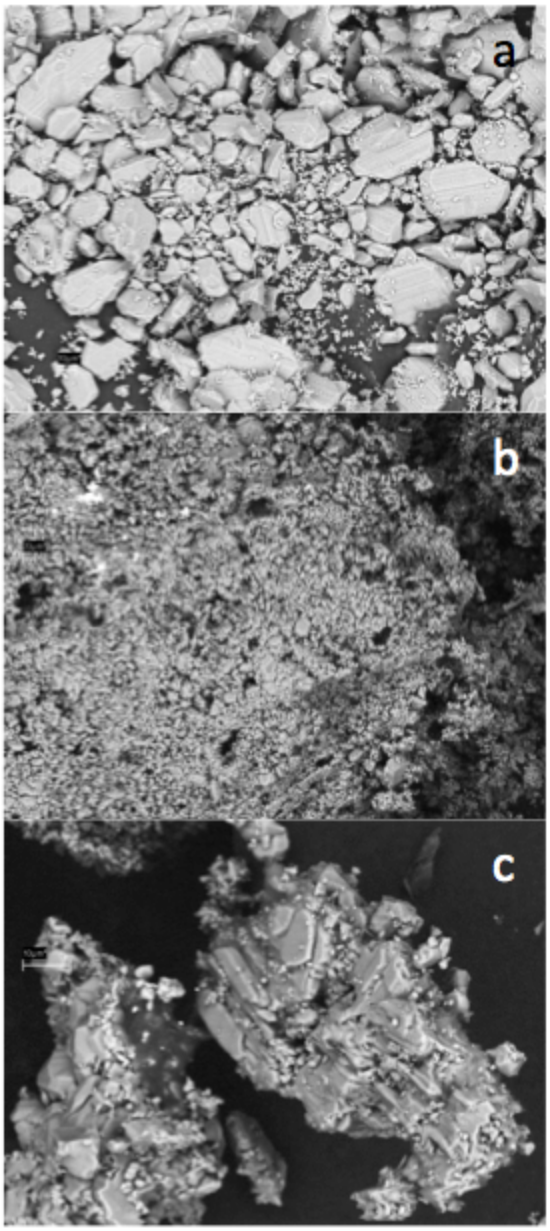

Figure 3.2 SEM photomicrographs of (a) forsterite starting material before grinding, (b) forsterite + magnesite after run, and (c) forsterite after preferential dissolution of magnesite after run. The textures in (c) show clear evidence of dissolution and recrystallization.

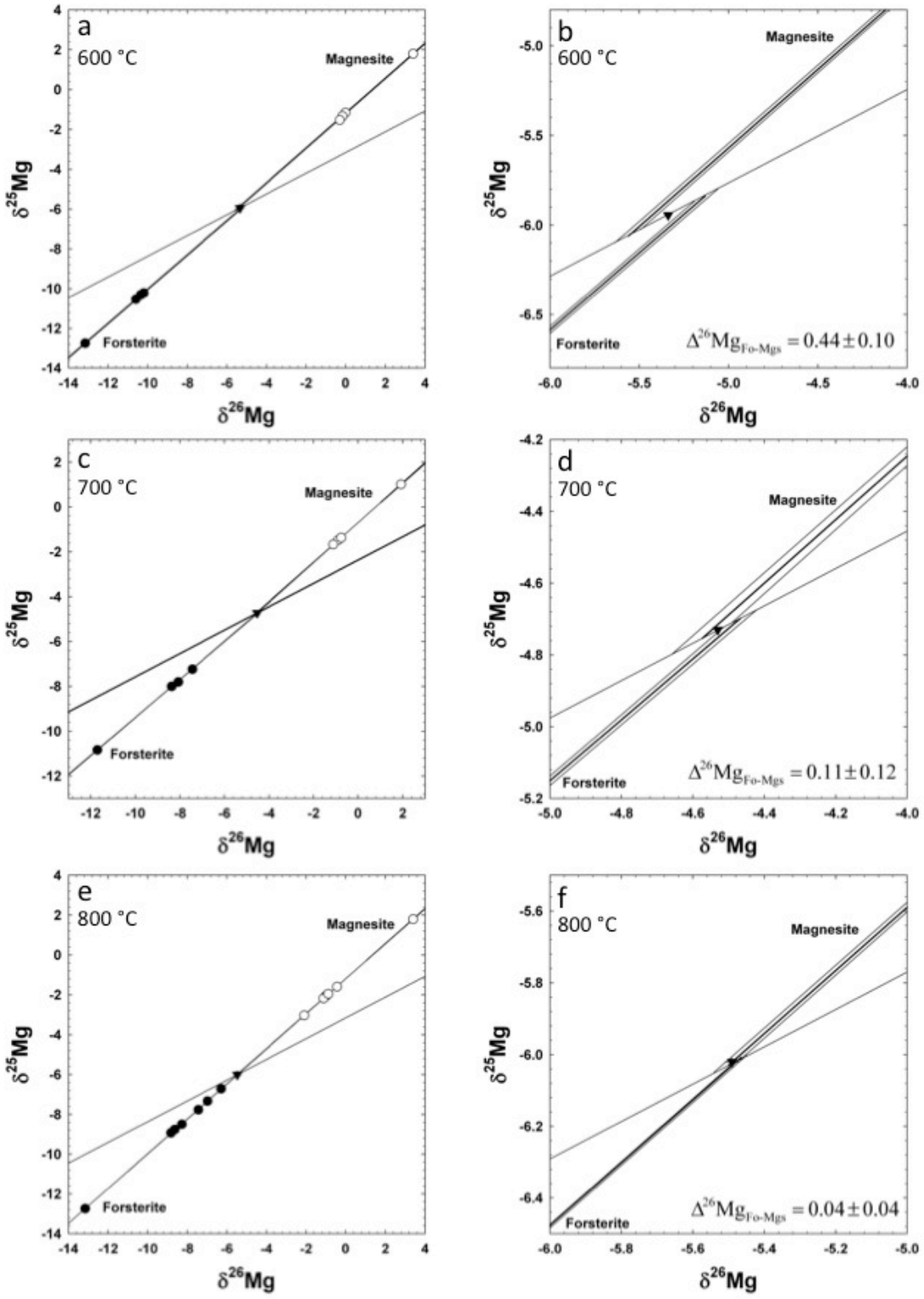

Figure 3.3 Experimental results for magnesite and forsterite at 600 °C (a, b), 700 °C (c, d), and 800 °C (e, f). Figures 3b, d, and f are close-ups of a, c, and e respectively. The open circles are magnesite, closed circles are forsterite, and upside down triangles are bulk compositions, which are measured directly for all cases except for Fo-Mgs 700 °C, where it was calculated from starting compositions. Error bars (2 se) are shown where they are larger than symbols. Heavy lines going through experimental data are best lines calculated using the new York regression (Mahon, 1996). Thinner lines on either side of best-fit lines are 2 se error envelopes.

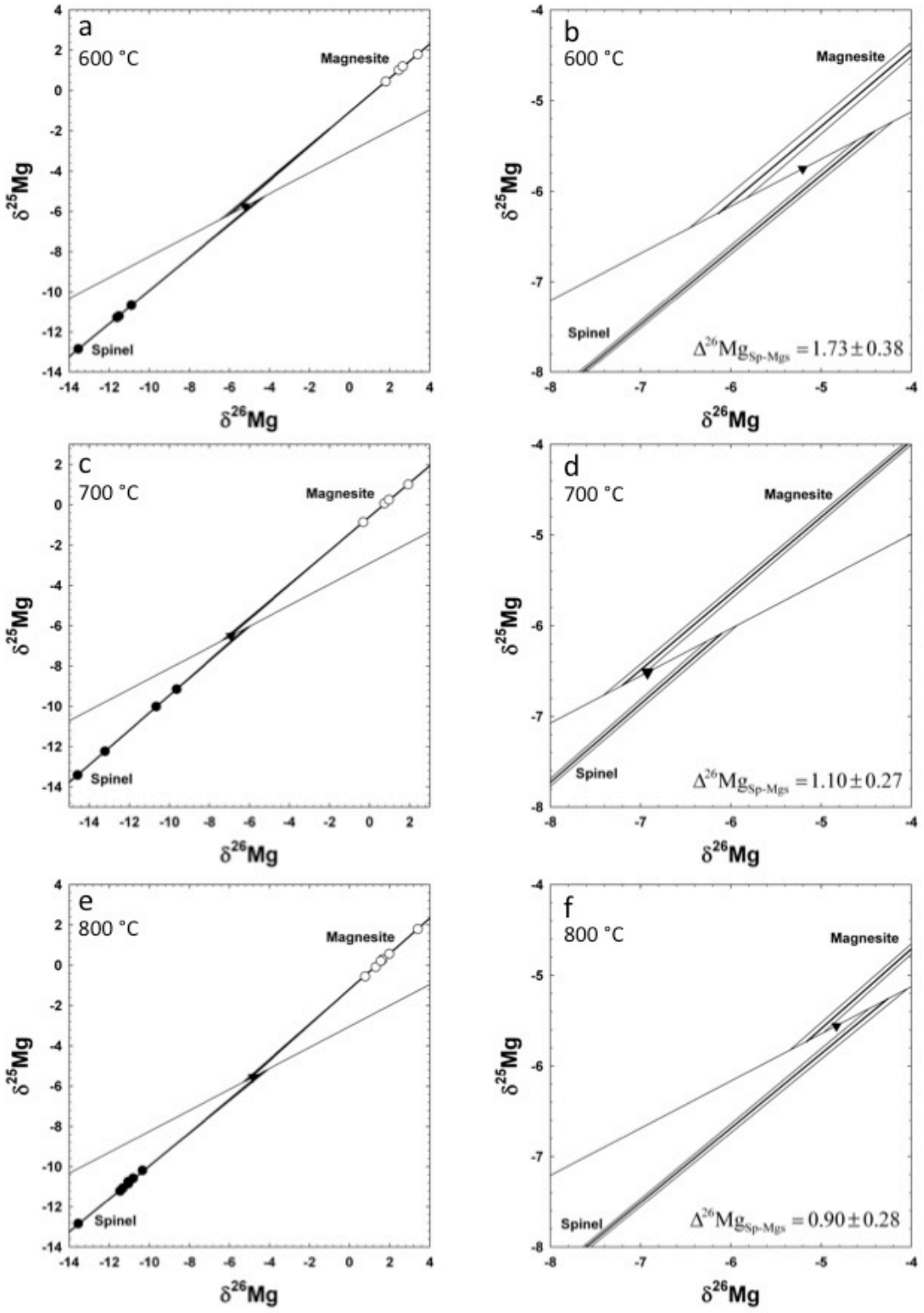

Figure 3.4 Experimental results for spinel and magnesite at 600 °C (a, b), 700 °C (c, d), and 800 °C (e, f). Figures 3b, d, and f are close-ups of a, c, and e respectively. The open circles are magnesite, closed circles are spinel, and upside down triangles are measured bulk compositions. Error bars (2 se) are shown where they are larger than symbols. Heavy lines going through experimental data are best lines calculated using the new York regression (Mahon, 1996). Thinner lines on either side of best-fit lines are 2 se error envelopes.

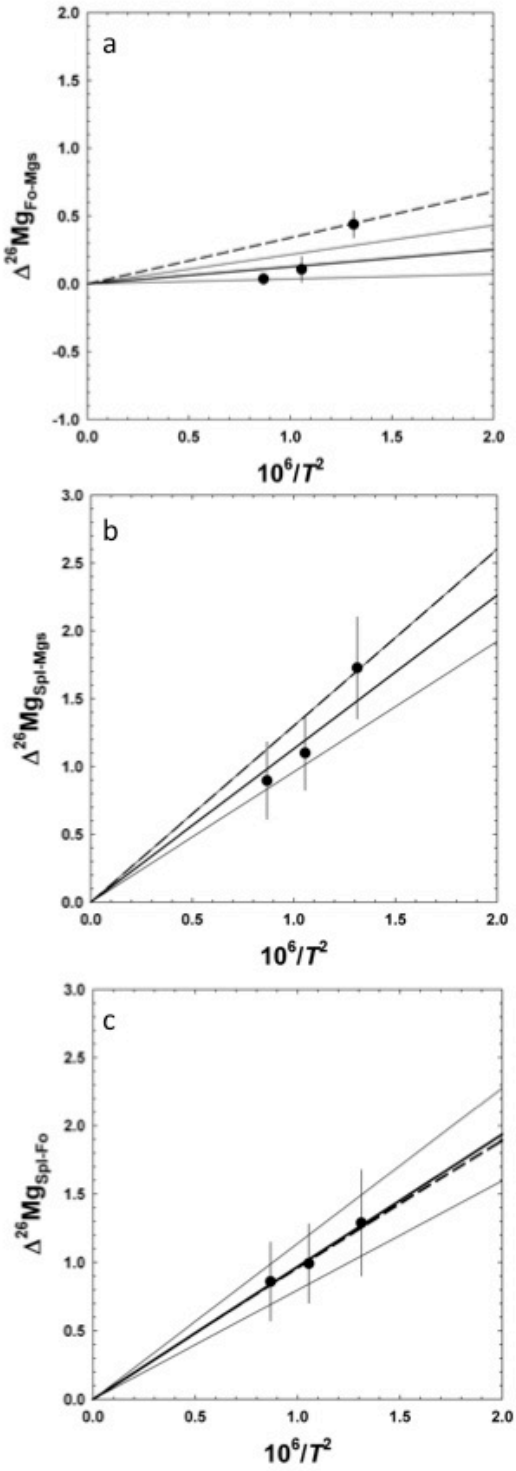

Figure 3.5 Experimental forsterite-magnesite (a), spinel-magnesite (b), and spinel-forsterite (c) Mg isotope fractionation data plotted as a function of temperature along with theoretical predictions (see text). Heavy lines are linear best-fits through the data (forced through the origin), thin lines are 2 se errors for the regressions , and dashed lines are theoretical predictions (Schauble, 2010). Error bars for the data are 2 se.

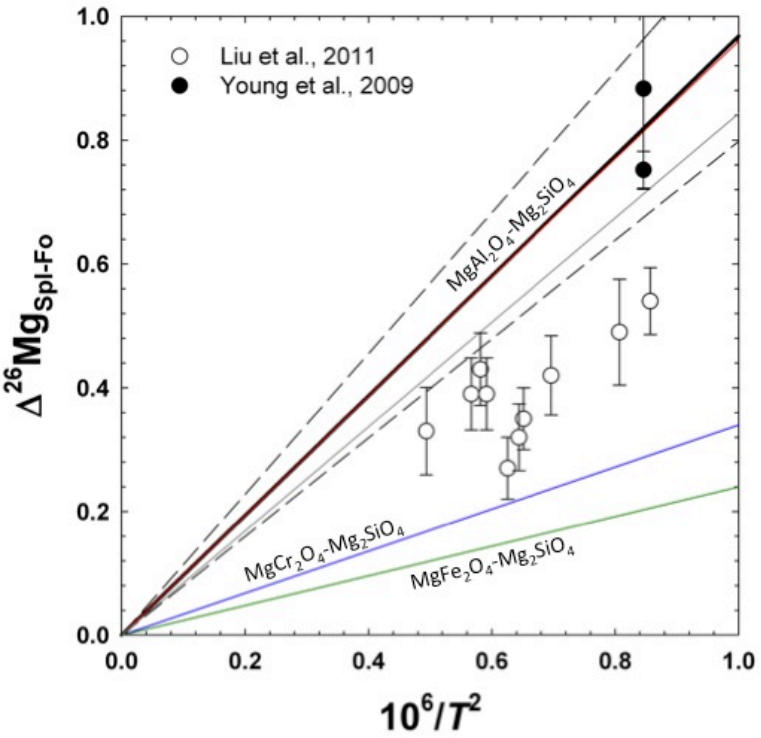

Figure 3.6 Comparison of measured Spl-Ol Mg isotope fractionation (Young et al., 2009; Liu et al. 2011) with experimentally and theoretically determined fractionation as a function of temperature. The heavy black line is the experimentally derived Spl-Fo fractionation. Dashed lines represent 2se errors on the experimental best-fit line. Colored lines are from theoretical calculations by Schauble (2010) for spinel-forsterite (red), magnesiochromite-forsterite (blue), and magnesioferrite-forsterite (green) fractionation. The grey line represents the fractionation line calculated by Liu et al. (2011) based on the Al:Cr:Fe^{3+} ratios of their spinels.

References

Alt J. C. and Teagle D. A. H. (1999) The uptake of carbon during alteration of oceanic crust. *Geochimica et Cosmochimica Acta* **63**, 1527-1535.

Biellmann C., Gillet P., Guyot F., Peyronneau J., and Reynard B. (1993) Experimental evidence for carbonate stability in the Earth's lower mantle. *Earth and Planetary Science Letters* **118**, 31–41.

Bigeleisen J. and Mayer M. G. (1947) Calculation of equilibrium constants for isotopic exchange reactions. *Journal of Chemical Physics* **15**, 261-267.

Black J. R., Yin Q.-Z., Rustad J. R. and Casey W. H. (2007) Magnesium isotopic equilibrium in chlorophylls. *Journal of the American Chemical Society* **129**, 8690-8691.

Brey G., Brice W. R., Ellis D. J., Green D. H., Harris K. L., and Ryabchikov I. D. (1983) Pyroxene-carbonate reactions in the upper mantle. *Earth and Planetary Science Letters* **62**, 63–74.

Chakrabati R. and Jacobsen S. B. (2010) The isotopic composition of magnesium in the inner solar system. *Earth and Planetary Science Letters* **293**, 349–358.

Clayton R. N., Goldsmith J. R., and Mayeda T. K. (1989) Oxygen isotope fractionation in quartz, albite, anorthite, and calcite. *Geochimica et Cosmochimica Acta* **53**, 725-733.

Eugster H. P. and Wones D. R. (1962) Stability relations of the ferruginous biotite, annite. *Journal of Petrology* **3**, 82-125.

Galy A., Bar-Matthews M., Halicz L., and O'Nions R. K. (2002) Mg isotopic composition of carbonate: insight from speleothem formation. *Earth and Planetary Science Letters* **201**, 105–115.

Gillet, P. (1993) Stability of magnesite (MgCO3) at mantle pressure and temperature conditions:

A Raman spectroscopic study. *American Mineralogist* **78**, 1328-1331.

Handler M. R., Baker J. A., Schiller M., Bennett V. C., and Yaxley G. M. (2009) Magnesium stable isotope composition of Earth's upper mantle. *Earth and Planetary Science Letters* **282**, 306-313.

Huang F., Zhang Z., Lundstrom C. C., and Zhi X. (2011) Iron and magnesium isotopic compositions of peridotite xenoliths from Eastern China. *Geochimica et Cosmochimica Acta* **75**, 3318-3334.

Katsura T. and Ito E. (1990) Melting and subsolidus phase relations in the $MgSiO_3$-$MgCO_3$ system at high pressures: implications to evolution of the Earth's atmosphere. *Earth and Planetary Science Letters* **99**, 110-117.

Katsura T., Tsuchida Y., Ito E., Yagi T., Utsumi W., and Akimoto S. I. (1991) Stability of Magnesite under the Lower Mantle Conditions. *Proceedings of the Japan Academy. Ser. B: Physical and Biological Sciences* **67**, 57-60.

Kerrick D. M. and Connolly J. A. D. (2001) Metamorphic devolatilization of subducted oceanic metabasalts: implications for seismicity, arc magmatism and volatile recycling. *Earth and Planetary Science Letters* **189**, 19-29.

Kushiro I. (1975) Carbonate-silicate reactions at high pressures and possible presence of dolomite

and magnesite in the upper mantle. *Earth and Planetary Science Letters* **28**, 116-120.

Lappin M. A. and Smith D. C. (1978) Mantle-equilibrated orthopyroxene eclogite pods from the basal gneisses in the Selje district, western Norway. *Journal of Petrology* **19**, 530-584.

Lazar C., Young E. D. and Manning C. E. (2012) Experimental determination of equilibrium nickel isotope fractionation between metal and silicate from 500° C to 950° C.

Geochimica et Cosmochimica Acta **86**, 276-295.

Liu S. A., Teng F. Z., Yang W. and Wu F. Y. (2011) High-temperature inter-mineral magnesium isotope fractionation in mantle xenoliths from the North China craton. *Earth and Planetary Science Letters* **308**, 131-140.

Mahon K. I. (1996) The New "York" regression: Application of an improved statistical method to geochemistry. *International Geology Review* **38**, 293-303.

Manning C. E. and Boettcher S. L. (1994) Rapid-quench hydrothermal experiments at mantle pressures and temperatures. *American Mineralogist* **79**, 1153-1158.

Matsuhisa Y., Goldsmith J. R., and Clayton R. N. (1978) Mechanisms of hydrothermal crystallization of quartz at 250 C and 15 kbar. *Geochimica et Cosmochimica Acta* **42**, 173-182.

Mavromatis V., Pearce C. R., Shirokova L. S., Bundeleva I. A., Pokrovsky O. S., Benezeth P., and Oelkers E. H. (2011) Magnesium isotope fractionation during hydrous magnesium carbonate precipitation with and without cyanobacteria. *Geochimica et Cosmochimica Acta* **76**, 161-174.

McGetchin T. R. and Besancon J. R. (1973) Carbonate inclusions in mantle-derived pyropes. *Earth and Planetary Science Letters* **18**, 408-410.

Molina J. F. and Poli S. (2000) Carbonate stability and fluid composition in subducted oceanic crust: an experimental study on H_2O–CO_2 bearing basalts. *Earth and Planetary Science Letters* **176**, 295-310.

Norman M. D., McCulloch M. T., O'Neill H. S. C., and Yaxley G. M. (2006) Magnesium isotopic analysis of olivine by laser-ablation multi-collector ICP-MS: composition dependent matrix effects and a comparison of the Earth and Moon. *Journal of Analytical*

Atomic Spectrometry **21**, 50-54.

Pearce C. R., Saldi G. D., Schott J., and Oelkers E. H. (2012) Isotopic fractionation during congruent dissolution, precipitation and at equilibrium: Evidence from Mg isotopes. *Geochimica et Cosmochimica Acta* **92**, 170-183.

Redfern S. A. T., Wood B. J., and Henderson C. M. B. (1993) Static compressibility of magnesite to 20 GPa: Implications for MgCO3 in the lower mantle. *Geophysical Research Letters* **20**, 2099-2102.

Rustad J. R., Casey W. H., Yin Q. Z., Bylaska E. J., Felmy A. R., Bogatko S. A., Jackson V. E., and Dixon D. A. (2010) Isotopic fractionation of Mg2+ (aq), Ca2+ (aq), and Fe2+ (aq) with carbonate minerals. *Geochimica et Cosmochimica Acta* **74**, 6301-6323.

Shahar A., Young E. D., and Manning C. E. (2008) Equilibrium high-temperature Fe isotope fractionation between fayalite and magnetite: an experimental calibration. *Earth and Planetary Science Letters* **268**, 330-338.

Shahar A., Hillgren V. J., Young E. D., Fei Y., Macris C., and Deng L. (2011) High-temperature Si isotope fractionation between iron metal and silicate. *Geochimica et Cosmochimica Acta* **75**, 7688–7697.

Schauble E. A. (2011). First-principles estimates of equilibrium magnesium isotope fractionation in silicate, oxide, carbonate and hexaaquamagnesium (2+) crystals. *Geochimica et Cosmochimica Acta* **75**, 844-869.

Ulmer G. C. (1971) *Research Techniques for High Pressure and High Temperature.* Springer-Verlag.

Urey H. C. (1947) The thermodynamic properties of isotopic substances. *Journal of the Chemical Society (Resumed)*, 562-581.

Wiechert U. and Halliday,A. N. (2007) Non-chondritic magnesium and the origins of the inner terrestrial planets. *Earth and Planetary Science Letters* **256**, 360-371.

Williams H. M., Nielsen S. G., Renac C., Griffin W. L., O'Reilly S. Y., McCammon C. A., Pearson N., Viljoen F., Alt J. C., and Halliday A. N. (2009) Fractionation of oxygen and iron isotopes by partial melting processes: Implications for the interpretation of stable isotope signatures in mafic rocks. *Earth and Planetary Science Letters* **283**, 156-166.

Wombacher F., Eisenhauer A., Böhm F., Gussone N., Kinkel H., Lezius J., Noe S., Regenberg M., and Rüggeberg A. (2006) Magnesium stable isotope compositions in biogenic $CaCO_3$. In *Geophysical Research Abstracts* **8**, 06353.

Yang J., Godard G., Kienast J. R., Lu Y., and Sun J. (1993) Ultrahigh-pressure (60 kbar) magnesite-bearing garnet peridotites from northeastern Jiangsu, China. *The Journal of Geology*, 541-554.

Yang W., Teng F. Z., and Zhang H. F. (2009) Chondritic magnesium isotopic composition of the terrestrial mantle: a case study of peridotite xenoliths from the North China craton. *Earth and Planetary Science Letters* **288**, 475-482.

Yang W., Teng F. Z., Zhang H. F., and Li S. G. (2012) Magnesium isotopic systematics of continental basalts from the North China craton: Implications for tracing subducted carbonate in the mantle. *Chemical Geology* **328**, 185-194.

Yaxley G. M. and Green D. H. (1994) Experimental demonstration of refractory carbonate-bearing eclogite and siliceous melt in the subduction regime. *Earth and Planetary Science Letters* **128**, 313-325.

Young E. D. and Galy A. (2004) The isotope geochemistry and cosmochemistry of magnesium. *Geochemistry of Non-Traditional Stable Isotopes*, vol. 55. MSA, pp. 197-230.

Young E. D., Tonui E., Manning C. E., Schauble E., and Macris C. A. (2009) Spinel–olivine magnesium isotope thermometry in the mantle and implications for the Mg isotopic composition of Earth. *Earth and Planetary Science Letters* **288**, 524-533.

Zhang R. Y., and Liou J. G. (1994) Coesite-bearing eclogite in Henan Province, central China: detailed petrography, glaucophane stability and PT-path. *European Journal of Mineralogy* **6**, 217-233.